

Abstract

Climate Change Effects on Precipitation Organization:
A Summertime Case Study in the Southeast United States

by Mark Nissenbaum

December, 2016

Director of Thesis: Dr. Rosana Nieto-Ferreira

DEPARTMENT OF GEOGRAPHY, PLANNING, AND ENVIRONMENT

The delivery of precipitation through large and small scale precipitation features plays a key role in the hydrological cycle. Therefore, it is important to understand how the organization of precipitation will change as the earth warms. The organization of precipitation can be characterized into either widespread, mesoscale precipitation features (MPF) or short-lived, isolated precipitation features (IPF). The Weather Research and Forecasting (WRF) model was used to simulate precipitation features at a 3 km resolution during the 17-22 June 2010 period in the Southeast US under present and future climate conditions. In this methodology, the model is first run in present climate mode and then rerun with an adjusted initial state that adds projected temperature anomalies for the 2090s based on Representative Concentration Pathways (RCPs) 4.5 and 8.5 from the Coupled Model Intercomparison Project Phase 5 (CMIP5) in the IPCC Fifth Assessment Report (AR5).

In the future climate simulations, small changes in precipitation occurred under RCP4.5 warming, but many significant changes were noted under RCP8.5 warming. Domain-averaged precipitation increased in the future climate simulations, with the largest changes over the ocean relative to the continent. In the future climates, IPF grew larger in length and eventually coalesced into MPF, reducing the total number of IPF and increasing the number of MPF. IPF and MPF also extended deeper into the troposphere and produced more precipitation overall.

Climate Change Effects on Precipitation Organization:
A Summertime Case Study in the Southeast United States

A Thesis

Presented To

The Faculty of the Department of Geography, Planning, and Environment
East Carolina University

In Partial Fulfillment

of the Requirements for the Degree

Geography M.S.

by

Mark Nissenbaum

December, 2016

©Copyright 2016
Mark Ryan Nissenbaum

CLIMATE CHANGE EFFECTS ON PRECIPITATION ORGANIZATION:
A SUMMERTIME CASE STUDY IN THE SOUTHEAST UNITED STATES

by

Mark Nissenbaum

APPROVED BY:

DIRECTOR OF THESIS: _____
Rosana Nieto-Ferreira, PhD

COMMITTEE MEMBER: _____
Thomas Rickenbach, PhD

COMMITTEE MEMBER: _____
Scott Curtis, PhD

COMMITTEE MEMBER: _____
Gary Lackmann, PhD (NCSU MEAS)

CHAIR OF THE DEPARTMENT OF GEOGRAPHY, PLANNING, AND ENVIRONMENT:

Burrell Montz, PhD

DEAN OF THE GRADUATE SCHOOL:

Paul J. Gemperline, PhD

ACKNOWLEDGEMENTS

I would like to thank my advisor, Dr. Rosana-Nieto Ferreira, for her guidance in the completion of this thesis. I would also like to thank my committee members Dr. Thomas Rickenbach, Dr. Scott Curtis, and Dr. Gary Lackmann for their feedback and support throughout this process. I would like to give special thanks to Dr. Thomas Rickenbach for his help with modifying portions of his feature identification algorithm for usage with WRF. I would also like to thank North Carolina State University professor, Dr. Gary Lackmann, for joining my committee and assisting me with my methodology.

I would like to thank the groups and organizations which made this thesis possible. The National Center for Atmospheric Research's (NCAR's) "WRF Help" assisted me with the installation of WRF on campus computers, and answered all of my WRF-related questions. I would also like to acknowledge NCAR's Yellowstone Supercomputer, which I used to run all of my WRF simulations. I would also like to thank the North Carolina Space Grant for a graduate research grant that funded my thesis in the summer of 2015. I would also like to acknowledge the National Science Foundation (Grant # AGS-1118141), which has supported this research from the beginning.

TABLE OF CONTENTS

LIST OF TABLES	vii
LIST OF FIGURES	viii
CHAPTER 1: INTRODUCTION	1
1.1 Purpose	1
1.2 Research Questions.....	2
CHAPTER 2: CURRENT STATE OF KNOWLEDGE	3
2.1 Precipitation Organization	3
2.2 Climate Change Projections	4
2.2.1 Temperature Projections.....	5
2.2.2 Precipitation Projections.....	6
2.3 Changes in SE US Precipitation	7
2.4 Downscaling Approaches	8
CHAPTER 3: RESEARCH METHODS	14
3.1 Case Study: 17-22 June 2010	14
3.2 WRF Model Setup	15
3.2.1 Study Domain	15
3.2.2 Data Sources	16
3.2.3 Parameterizations	16
3.2.4 WRF Output	17
3.3 Future Climate Simulations	17
3.4 Analysis	19
3.4.1 Synoptic-Scale Environment	20
3.4.2 Feature Identification Algorithm.....	21
CHAPTER 4: RESULTS	22
4.1 Synoptic-Scale Environment	23
4.1.1 850 and 250 mb Winds.....	24
4.1.2 Sea Level Pressure.....	26
4.1.3 CAPE and CIN	27
4.2 Total Accumulated Precipitation	31
4.2.1 Total Precipitation	31

4.2.2 IPF and MPF Precipitation	33
4.2.3 IPF/MPF Precipitation Fractions	42
4.2.4 Diurnal Cycle of Precipitation.....	43
4.3 Precipitation Features	51
4.3.1 Feature Numbers	51
4.3.2 Feature Lengths	52
4.3.3 Feature Echo Heights	56
4.3.4 Feature Total Precipitation	61
CHAPTER 5: DISCUSSION.....	67
5.1 Model Evaluation.....	67
5.1.1 Total Precipitation	67
5.1.2 Continental Precipitation	67
5.1.3 Ocean Buffer Precipitation	68
5.1.4 Gulf Stream Precipitation	68
5.1.5 Precipitation Features	71
5.1.6 IPF Precipitation	71
5.1.7 MPF Precipitation.....	72
5.1.8 CAPE and CIN	72
5.2 Future Climates.....	73
5.2.1 Total Precipitation	73
5.2.2 Continental Precipitation	73
5.2.3 Oceanic Precipitation.....	74
5.2.4 Precipitation Features	74
5.2.5 IPF Precipitation	75
5.2.6 MPF Precipitation.....	75
5.2.7 CAPE and CIN	76
CHAPTER 6: CONCLUSION	77
REFERENCES	79
APPENDIX: SURFACE AND UPPER AIR WEATHER MAPS	84

LIST OF TABLES

1. Comparison among the different RCPs	6
2. Major research papers that utilized the pseudo global warming method.....	10
3. WRF domain parameterizations	17
4. List of CMIP5 GCMs used in the creation of the MMM	19
5. IPF and MPF precipitation in NMQ and WRF-CC	32
6. IPF and MPF precipitation in WRF-CC, WRF-RCP4.5, and WRF-RCP8.5	33
7. Number of precipitation features in WRF-CC and NMQ.....	51
8. Number of precipitation features in WRF-CC, WRF-RCP4.5, and WRF-RCP8.5.....	52
9. Average CAPE and temperatures in the WRF simulations	76

LIST OF FIGURES

1. Radar data coverage across the US	3
2. WPS domain configuration.....	15
3. Future climate simulation process in WRF.....	18
4. Upper-level winds at 250 mb.....	22
5. Lower-level winds at 850 mb	23
6. Upper-level wind differences.....	24
7. Lower-level wind differences	25
8. Sea level pressure.....	26
9. Sea level pressure differences.....	27
10. Diurnal cycle of CAPE	29
11. Diurnal cycle of CIN.....	30
12. Offshore ocean buffer	31
13. Maps of precipitation in NMQ.....	35
14. Maps of precipitation in WRF-CC.....	36
15. Maps of precipitation in WRF-RCP4.5.	37
16. Maps of precipitation in WRF-RCP8.5.	38
17. Maps of precipitation differences between WRF-CC and NMQ.....	39
18. Maps of precipitation differences between WRF-RCP4.5 and WRF-CC	40
19. Maps of precipitation differences between WRF-RCP8.5 and WRF-CC	41
20. IPF and MPF precipitation fractions for NMQ and WRF-CC.....	42
21. IPF and MPF precipitation fractions for the future climate simulations	42
22. Diurnal cycle of precipitation in WRF and NMQ	44
23. Diurnal cycle of precipitation in the future climate simulations.....	45
24. Maps of diurnal precipitation in NMQ	47
25. Maps of diurnal precipitation in WRF-CC	48
26. Maps of diurnal precipitation in WRF-RCP4.5	49
27. Maps of diurnal precipitation in WRF-RCP8.5	50
28. IPF feature length histograms for WRF-CC and NMQ.....	53
29. MPF feature length histograms for WRF-CC and NMQ.....	54
30. IPF feature length histograms for the future climate simulations.....	55
31. MPF feature length histograms for the future climate simulations.....	56
32. IPF echo height histograms for WRF-CC and NMQ.....	58
33. MPF echo height histograms for WRF-CC and NMQ	59
34. IPF echo height histograms for the future climate simulations	60
35. MPF echo height histograms for the future climate simulations	61
36. IPF feature total precipitation histograms for WRF-CC and NMQ.....	63

37. MPF feature total precipitation histograms for WRF-CC and NMQ	64
38. IPF feature total precipitation histograms for the future climate simulations	65
39. MPF feature total precipitation histograms for the future climate simulations	66
40. Comparison of SSTs at the beginning and end of the simulation.....	69
41. Comparison of precipitation between NMQ, WRF-CC, and WRF-CC with SST update.....	70
42. SPC surface analysis plots for the 17-22 June 2010 period.....	84
43. SPC upper air plots for the 17-22 June 2010 period.....	87

CHAPTER 1: INTRODUCTION

While there is still great debate among politicians and the public at large, climate scientists almost universally agree that global warming is happening and that it is important to manage the future risks. As the climate warms and our polar ice caps melt, the amount of precipitation will also change. Any changes in precipitation will be reflected in the hydrological cycle and ultimately trickle down to water availability for human use. The focus of this research is to understand how precipitation organization, specifically within the Southeast (SE) United States (US), will change in a warmer world. To do this, case studies of past weather events were simulated using the Weather Research and Forecasting (WRF) model and then reran with modified initial conditions to represent temperature anomalies for the 2090s.

1.1 Purpose

This work focuses on understanding the effect of climate change on precipitation organization in the SE US. Precipitation is characterized in this thesis by the size of precipitating radar features into either isolated precipitation features (IPF) or mesoscale precipitation features (MPF). Since the size of precipitation features has a connection to the environmental factors that form and maintain precipitation, this study may offer guidance to improve the simulation of regional precipitation change in climate models. Any changes in the distributions and characteristics of IPF and MPF may potentially affect regional hydrology, which affects access to drinking water, hydroelectricity, dams, and agriculture. Therefore, this study of the effect of climate change on precipitation organization is of primary importance.

The effect of climate change on precipitation organization in the regional climate is still not well understood. Climate modeling usually involves the use of general circulation models (GCMs) that are too coarse in resolution to resolve small-scale features, such as squall lines and

sea breeze thunderstorms. GCMs must sacrifice spatial resolution in order to simulate the entire planet on decadal to centurial time scales. At convective-resolving resolutions, these GCMs would be too costly to operate, as it would greatly delay the eventual study of the models by research groups. Hence various dynamical and statistical methods for downscaling coarse resolution GCM data into finer resolutions for the study of regional climates have been developed. This study uses dynamical downscaling with WRF to explicitly simulate convection and to address the research questions listed below.

1.2 Research Questions

1. How well does WRF-simulated precipitation organization compare to the observations in the National Mosaic & Multi-Sensor QPE (NMQ) dataset?
2. Will the increase in temperature cause a shift in the distributions of precipitation organization? If so, will the shift be towards more IPF or more MPF?
3. How will the horizontal and vertical structure of precipitation organization change?
4. How will precipitation totals in general change?

CHAPTER 2: CURRENT STATE OF KNOWLEDGE

2.1 Precipitation Organization

Rickenbach et al. (2015) used a size-based classification scheme to study the seasonality of precipitation in the SE US using the National Mosaic & Multi-Sensor QPE dataset (NMQ, Zhang et al. 2011). The NMQ is a 1 km x 1 km x 5 min high resolution mosaic of Next Generation Doppler Radars (NEXRAD) for the contiguous US developed by the National Oceanic and Atmospheric Administration (NOAA) National Severe Storm Laboratory (NSSL). The extent of NEXRAD radar data coverage is shown in Figure 1. Rickenbach et al. (2015) classified precipitation features into either IPF or MPF based on maximum feature length. MPF are classified when maximum feature length exceeds 100 km, while all other smaller features are identified as IPF (Rickenbach et al. 2015).

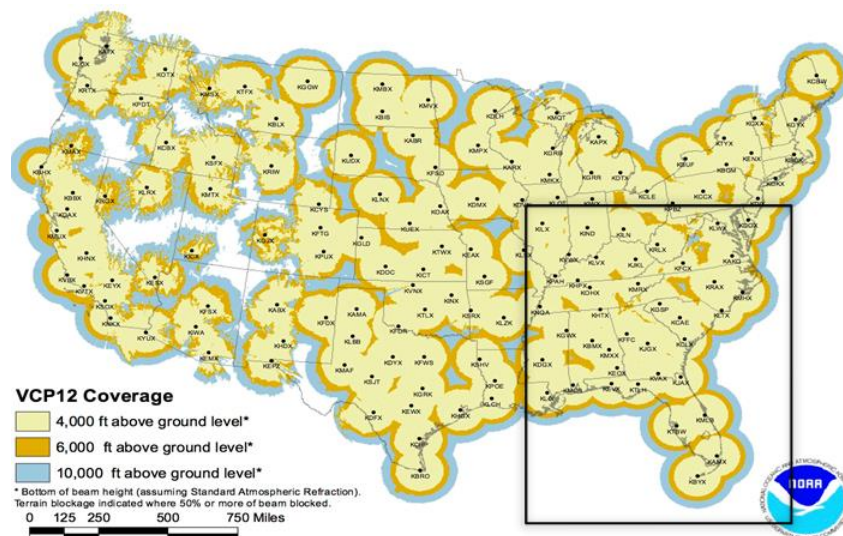


Figure 1 Radar data coverage across the US. Areas in light yellow have excellent coverage, while areas in orange and blue have difficulty seeing the lower-levels of the troposphere, which can make thunderstorms and rain appear weaker than they actually are. Areas in white contain no radar coverage at all. The SE US has been indicated in a black outline. Source: NOAA

The algorithm analyzes each 15 minute NEXRAD snapshots on a pixel-by-pixel basis. First, pixels are flagged as either rain or snow based on the “Q2” product of the NMQ dataset,

which contains water phase information (i.e., whether the pixel contained rain or snow). Precipitation features are defined as contiguous pixels with rainrates ≥ 0.5 mm/hr, which is the equivalent of ≥ 5 dBZ on radar reflectivity.

A four-year climatology of precipitation organization for the SE US is presented in Rickenbach et al. (2015). They find that IPF occur year-round in the SE US, but contribute a larger fraction of the total summertime precipitation, as most convection is driven by daytime heating and local forcing processes, such as the sea breeze, which produce smaller-scale precipitation features on average (Rickenbach et al. 2015). MPF are also present year-round, but contribute a larger fraction of seasonal precipitation during the winter and transitional months, in conjunction with the passage of midlatitude cyclones that more directly impact the SE US. According to Ferreira et al. (2013), up to 70% of wintertime precipitation in the SE US can be accounted for by midlatitude cyclones. Synoptic-scale forcing by midlatitude cyclones allow for MPF to develop and grow into squall lines, mesoscale convective systems (MCSs, as defined by Houze et al. 1990), or large regions of stratiform precipitation. Because Rickenbach et al. (2015) classifies NMQ precipitation based on maximum feature size alone, it is possible for regions of snow showers can be labeled as MPF or IPF. The precipitation organization classification algorithm described by Rickenbach et al. (2015) provides a useful strategy to objectively classify precipitation features.

2.2 Climate Change Projections

Today most climate scientists agree that the recent trends in warmer-than-average global temperatures have occurred as a result of anthropogenic processes from the burning of fossil fuels, which release large amounts of CO₂ into the atmosphere (Kharin et al. 2007; Stocker et al. 2013; Cubasch et al. 2001; and others). Global surface temperatures have warmed by over

0.85°C from 1880 to 2012, and may only become more extreme by the end of the 21st century (Stocker et al. 2013). The most recent late-century global temperature projections are provided in the Intergovernmental Panel on Climate Change (IPCC) Fifth Assessment Report (AR5), but the influence of these warmer temperatures on precipitation patterns remains an active area of interest.

2.2.1 Temperature Projections

The latest set of climate change temperature projections have been carried out in the Coupled Model Intercomparison Project Phase 5 (CMIP5), under the auspice of the IPCC AR5. The CMIP5 began in 2007 as a coordinated effort by the Working Group on Coupled Modelling (WGCM) of the World Climate Research Programme (WCRP) and culminated with the publication of the IPCC Fifth Assessment Report (AR5) in 2013 (Taylor et al. 2012). Advancements in technology and computer processing power have enabled the GCMs in the CMIP5 to operate at finer spatial resolutions and even simulate the full biogeochemical cycle for the study of carbon transfer (Taylor et al. 2012). With over 50 GCMs and more than 20 participating agencies from around the world, the CMIP5 represents an international effort for the study of climate change (Taylor et al. 2012). The entire volume of data produced by the CMIP5 spans over 3 petabytes, which is nearly 100 times the volume of data created by the GCMs in the AR4 (Taylor et al. 2012; Stouffer et al. 2011).

These new temperature projections are guided by a series of emission scenarios, namely the Representative Concentration Pathways (RCPs). These updated scenarios assume the same magnitudes of CO₂ emissions in the previous IPCC Fourth Assessment Report (AR4), but have been restructured to incorporate the latest projections in carbon reduction policy, population trends, aerosol emissions, and so forth, which play a key role in global average temperature

trends (Kirtman et al. 2013). The approximate radiative forcing level (in W m^{-2}) in the year 2100 is what gives the RCPs their distinct name (e.g., RCP2.6 and RCP8.5). RCP2.6 represents low-range warming by the end of the century, with aggressive mitigation strategies to reduce carbon emissions and lower global temperatures. RCP4.5 and RCP6.5 represent mid-range warming, with some policy to reduce carbon emissions. RCP8.5 represents high-range warming, with “business as usual” carbon emissions and few, if any, strategies to reduce emissions. A list of the different RCPs and their impact on global mean surface temperature is shown in Table 1.

Scenario	Radiative Forcing (W m^{-2})	CO ₂ by 2100 (ppm)	Global Mean Surface Temperature Change (°C)	
			2046-2065	2081-2100
RCP2.6	2.6	421	1.0	1.0
RCP4.5	4.5	538	1.4	1.8
RCP6.0	6.0	670	1.3	2.2
RCP8.5	8.5	936	2.0	3.7

Table 1 Comparison among the different RCPs and their effect on global mean surface air temperature during the period from 2046-2065 and 2081-2100 relative to the modern period of 1986-2005 (IPCC).

2.2.2 Precipitation Projections

Kharin et al. (2007) estimated that mean global precipitation could increase by 5.3% by the end of the century, with an even greater 6.8% increase over land surfaces. Many climatologists (e.g., Allen & Ingram 2002; Held & Soden 2006; Pall et al. 2007) have alleged that the future climate warming will take place under the same relative humidity values as the present climate. If this is the case, then precipitation can be expected to change by 6-7% per degree Celsius in accordance with the Clausius-Clapeyron relationship (Pall et al. 2007).

The Clausius-Clapeyron relationship is the basis behind the “rich get richer and poor get poorer” hypothesis regarding global projections in precipitation change. Under this hypothesis, the greatest increases in precipitation could be expected in existing wet regions, while dry

regions will only get dryer (Pall et al. 2007; Allen & Ingram 2002). Pall et al. (2007) has demonstrated that increased precipitation is likely over the already wet tropical oceans, while mid latitude regions governed by subtropical ridges will could see less precipitation, due to changes in rising and sinking air associated with the global atmospheric circulation. The effects of the Clausius-Clapeyron relationship will be felt more strongly in extreme precipitation events, which are capable of removing the entire column of water from the atmosphere (Pall et al. 2007; Allen & Ingram 2002).

2.3 Changes in SE US Precipitation

As previously discussed, the global nature of precipitation is expected to change in the future, with enhanced wet and dry regions around the tropical and subtropical belts of the world (Pall et al. 2007; Allen & Ingram 2002). The manifestation of these global changes into the regional climate, particularly the SE US, remains a deep subject of investigation among climatologists. This is partly due to the intricacies of precipitation in the SE US, which varies greatly on seasonal to interannual timescales; however, most precipitation variation during the summer season can be explained through the natural variability of the North Atlantic Subtropical High (NASH; Li et al. 2013; Li et al. 2011).

During the winter months, precipitation in the SE US is mostly delivered from the passage of midlatitude cyclones, which can impart thunderstorms, squall lines, stratiform rain, snow, and other forms of precipitation onto the landscape (Ferreira et al. 2013; Nieto Ferreira & Hall 2015). On the other hand, precipitation from midlatitude cyclones is minimized during the summer months, as the NASH plays a larger role in precipitation. Li et al. (2013) found that different positions of the NASH favor more precipitation in the SE US, while other positions favor less precipitation. A northwest position of the NASH is associated with reduced

precipitation across the SE US, while a southwest position favors more precipitation (Li et al. 2013; Li et al. 2011).

While there is no clear trend in SE US precipitation change in the recent decades, the nature of precipitation has become more variable, with larger amplitudes between wet and dry years (Li et al. 2013). In addition, Li et al. (2013) has observed a westward shift in the western end of the NASH, which favors even more variability between wet and dry years. In studies of the IPCC climate models, this western edge of the NASH has been shown to continue its westward jog into the future (Li et al. 2011; Wang et al. 2010), which will only increase summertime precipitation variability in the SE US.

2.4 Downscaling Approaches

While IPCC GCMs provide crucial information on precipitation changes at the global scale, they provide crude representations at the regional scale, which can make the study of regional climate change difficult. In order to overcome these barriers, downscaling techniques have been invented to resample coarse resolution GCM data into a finer resolution for the study of the regional and local climate. Downscaling is achieved either statistical or dynamical means (Ueyama 2012). The statistical approach can “correct” coarse resolution datasets by matching specific locations with actual climatological values (Gutmann et al. 2012; Ueyama 2012), while the dynamical downscaling simply runs the coarse resolution GCM data through high resolution NWP model, which reveals the finer details hidden in the original dataset.

In dynamical downscaling, the coarse resolution GCM provides the boundary conditions to the model (Castro 2005). This form of downscaling is the easiest to execute, but the major disadvantage is that it requires running the model for long periods of time in order to obtain any usable data, which is not feasible for high resolution NWP models at the regional level. An

updated approach, dubbed the pseudo global warming method (PGW), incorporates the coarse resolution GCM data *and* a subject or time period of interest into the NWP for the study of the regional climate. PGW is a modern version of the surrogate global warming approach (Frei et al. 1998; Schär et al. 1996), in which initial conditions in a NWP model are uniformly adjusted by constant temperature anomalies and the model is rerun to study the same conditions under a future (“pseudo”) climate. In PGW, the temperature adjustment to the NWP model is provided by the coarse resolution data in the GCM projections (Sato et al. 2007; Kimura & Kitoh 2007). This method frequently involves the modification of air temperature, but some studies have modified other variables as well, such as wind speed and SSTs (Table 2). Unlike the surrogate approach, PGW accounts for vertical and horizontal variations in temperature anomalies due to latitudinal and continental/oceanic effects. For instance, the largest surface temperature anomalies can be found near the poles versus the tropics, and surface temperatures are less variable over the oceans.

Yoshikane et al. (2012) and Kawase et al. (2008) have demonstrated that PGW exhibits fewer biases than other downscaling methods because the present climate weather conditions are retained in the future climate simulations, which allows for an “apples-to-apples” comparison between the present and future climate simulations. In PGW, natural variability from the underlying GCM is kept to a minimum, which eliminates uncertainty in the downscaled simulation (Kawase et al. 2008). However, PGW does tend to overestimate precipitation near the upstream side of model boundaries where information enters the domain, which is more of an issue in smaller domains (Yoshikane et al. 2012).

A comprehensive list of some of the most recent and well-known PGW studies is shown in Table 2. PGW studies have utilized a wide range of NWP models, with WRF becoming

increasingly popular (Table 2). Researchers have created PGW simulations spanning just a couple of days to over several years' duration with differing model physics and data sources, tailored to best represent their subject of interest (Table 2). Climate scientists have investigated a wide range of topics using PGW, such as the study of climate change on tropical cyclones (Kanada et al. 2013), rice production in Japan (Iizumi et al. 2007), and extreme precipitation events (Lackmann 2013). An assumption made by many researchers (Table 2), and supported by the discussion in the earlier sections (Allen & Ingram 2002; Held & Soden 2006; Pall et al. 2007), is to increase temperatures in PGW under constant relative humidity. This makes many of the future climate changes in precipitation a function of increased vapor pressure due to the Clausius-Clapeyron relationship. Lackmann (2013) noted the Clausius-Clapeyron response to precipitation with his focus on the Tennessee Valley (Pall et al. 2007), similar to the conclusions reached by Frei et al. (1998) and Schär et al. (1996) in their surrogate global warming studies of European precipitation. The Clausius-Clapeyron relationship provides a reasonable explanation for the increase in precipitation due to thermodynamic changes, but it does not explain any changes due to dynamics, which are more difficult to diagnose.

Reference	(1) Study Area (2) Interest	(1) Model (2) Resolution (3) Cumulus (4) Microphysics (5) Simulation length	Data Sources (1) Present climate (2) Future Differences (3) Adjusted Variables	Major Findings
Willison et al. (2015)	(1) North Atlantic (2) Sensitivity of storm track response to global warming under different resolutions	(1) WRF V3.4.1 (2) 20 and 120 km (3) Zhang-McFarlane (ZM) (4) WRF Single-Moment-6 (WSM6) (5) 4 months	(1) National Centers for Environmental Prediction (NCEP) final operational global analysis (FNL) (2) Multimodel mean of five CMIP5 models (3) air temperature and sea surface temperature (SST)	Variable response of extratropical storms to horizontal resolution under warmer climate

Table 2 Comparisons among some major research papers that utilized the pseudo global warming method. Basic model parameterizations are shown only for the domains of interest.

Reference	(1) Study Area (2) Interest	(1) Model (2) Resolution (3) Cumulus (4) Microphysics (5) Simulation length	Data Sources (1) Present climate (2) Future Differences (3) Adjusted Variables	Major Findings
Kanada et al. (2013)	(1) Japanese Islands (2) Intense tropical cyclones	(1) Nonhydrostatic model (2) 2 km (3) Explicit (4) Bulk-type (Murakami 1990) (5) 90-144 hours	(1) Meteorological Research Institute Atmospheric GCM, version 3.2 (MRI-AGCM3.2) (2) Multimodel mean of the CMIP3 GCMs for the A1B emission scenario (3) SST	Increase in pressure falls, radii of maximum hourly precipitation decrease
Lackmann (2013)	(1) Southeast US (2) Major precipitation event	(1) WRF V3.2.1 (2) 6 km (3) Explicit (4) WSM6 (5) 96 hours	(1) GFS 1° Final Analysis (2) Multimodel mean of five IPCC AR4 GCMs for the A1B emission scenario (3) air temperature, SST, soil temperature; constant relative humidities	Increase in overall precipitation; stronger updrafts; no change in the strength of the low-level jet
Mallard et al. (2013)	(1) Atlantic Ocean (2) Atlantic hurricanes	(1) WRF V3.0.1.1 (2) 6 km (3) Explicit (4) Morrison et al. (2009) two-moment and WSM6 (5) 30 days	(1) GFS 1° Final Analysis (2) 20-member ensemble of GCM simulations from the IPCC AR4 for the A1B emission scenario (3) air temperature and SST; constant relative humidities	Reduction in tropical storms, hurricanes, and major hurricanes
Adachi et al. (2012)	(1) Tokyo metropolitan area, Japan (2) urban heat islands	(1) Terrestrial Environment Research Centre – Regional Atmospheric Modeling System (TERC-RAMS) (2) 3 km (3) Arakawa-Schubert (4) Walko et al. (1995) (5) 37 days	(1) Japanese 25-Year Reanalysis Project (JRA-25) (2) JRA-25, five single GCMs, multimodel mean of five GCMs (3) air temperature and SST; constant relative humidities	Significant variations in temperature change among different GCM members; multimodel GCMs could be a better way of understanding changes
Yoshikane et al. (2012)	(1) East Asia (2) Verification of PGW method	(1) WRF (2) 20 km (3) Kain-Fritsch (4) WSM6 (5) 30 years	(1) Model for Interdisciplinary Research On Climate (MIROC3.2_MEDRES) (2) MIROC3.2_MEDRES for the A1B emission scenario (3) Not specified.	PGW climate statistically equivalent to the assumed true climate; precipitation increases near the upstream side of lateral boundaries

Table 2 continued.

Reference	(1) Study Area (2) Interest	(1) Model (2) Resolution (3) Cumulus (4) Microphysics (5) Simulation length	Data Sources (1) Present climate (2) Future Differences (3) Adjusted Variables	Major Findings
Hill & Lackmann (2011)	(1) western tropical Atlantic main development region (MDR) (2) tropical cyclone intensity and structure	(1) WRF V2.2 (2) 6 and 2 km (3) Explicit (4) WSM6 (5) 5-10 days	(1) National Centers for Environmental Prediction–National Center for Atmospheric Research (NCEP–NCAR) reanalysis (2) Multimodel mean from 13 different IPCC AR4 GCMs (3) air temperature, moisture, and SST	Increase in pressure falls; increase in precipitation
Tsunematsu et al. (2011)	(1) Asia (2) Dust emissions	(1) WRF/WRF-Chem V3.1 (2) 40 km (3) Kain-Fritsch (4) Lin (5) 72 hours	(1) National Centers for Environmental Prediction–FINaL (NCEP–FNL) (2) Model for Interdisciplinary Research On Climate (MIROC; V3.2-hires) (AR4 A1B scenario) (3) air temperature, geopotential heights, and u-v wind components; constant relative humidities	weakening of sea level pressure gradients; weakening of cold air surges; reduction in future Asian dust emission
Rasmussen et al. (2011)	(1) Colorado (2) snowfall	(1) WRF V3.0 (2) 2 km (3) Explicit (4) Thompson et al. (2008) (5) 6 months	(1) North American Regional Analysis (NARR) (2) Community Climate System Model (CCSM) for the A2 emission scenario (3) air, surface, and soil temperatures	Increase in precipitation; higher melting levels; small changes in vertical velocities
Hara et al. (2008)	(1) Japan (2) snowfall	(1) WRF V2.2 (2) 5 km (3) Not specified. (4) WSM6 (5) 41 days	(1) NCEP/NCAR reanalysis (2) MIROC3.2 for the A2 emission scenario (3) air temperature, u-v wind components, geopotential heights, and SSTs; constant relative humidities	reduction in snowfall

Table 2 continued.

Reference	(1) Study Area (2) Interest	(1) Model (2) Resolution (3) Cumulus (4) Microphysics (5) Simulation length	Data Sources (1) Present climate (2) Future Differences (3) Adjusted Variables	Major Findings
Fujihara et al. (2008)	(1) Seyhan River Basin, Turkey (2) hydrology and water resources	(1) TERC-RAMS (2) 8.3 km (3) Not specified. (4) Not specified. (5) Not specified.	(1) NCEP/NCAR reanalysis (2) MRI-CGCM2 and CCSR/NIES/FCGC-MIROC for the A2 emission scenario (3) air temperature, geopotential height, u-v wind component, specific humidity, and SSTs	Decrease in snowpack and runoff
Kawase et al. (2008)	(1) East Asia (2) Mei-yu rainband; reliability of PGW method on hindcast data for the 1960s	(1) WRF V2.2 (2) 40 km (3) Kain-Fritsch (4) WSM6 (5) 40 days	(1) 40 year ECMWF reanalysis (ERA-40) (2) ERA-40 (3) air temperature, geopotential height, u-v wind component, and SSTs; constant relative humidities	The PGW method reliably reproduced the hindcast 1960s climate
Iizumi et al. (2007)	(1) Japan (2) rice production	(1) TERC-RAMS (2) 30 km (3) Arakawa-Schubert (4) Walko et al. (1995) (5) 1 year	(1) NCEP/NCAR reanalysis (2) MRI-CGCM2 for the A2 emission scenario (3) air temperature, geopotential heights, u-v wind component, specific humidity, and SSTs	Larger increase in daily minimum temperature compared to maximum temperature; greater temperature change in cooler year; spatial increases/decreases in precipitation
Sato et al. (2007)	(1) Mongolia (2) Precipitation	(1) TERC-RAMS (2) 30 km (3) Arakawa-Schubert (4) Walko et al. (1995) (5) 36 days	(1) NCEP-NCAR reanalysis (2) MRI-CGCM2 for the A2 scenario (3) air temperature, geopotential heights, u-v wind component, specific humidity, and SSTs	Precipitation tended to decrease; reduction in middle to heavy rainfall events ($> 4 \text{ mm hr}^{-1}$); decrease in soil moisture

Table 2 continued.

CHAPTER 3: RESEARCH METHODS

This chapter begins with a discussion of the synoptic-scale conditions during 17-22 June 2010 period, which has been selected for the study of climate change on precipitation organization. Then, an overview of the WRF and PGW setup is provided. Finally, a summary of analysis techniques used to validate the model and understand the future climate changes using the Rickenbach et al. (2015) feature identification algorithm is presented.

3.1 Case Study: 17-22 June 2010

The 17-22 June 2010 period has been selected for this study because it is representative of ordinary summertime convection in the SE US with very little midlatitude cyclone influence. This convective period is driven primarily by thermodynamic instability from afternoon thunderstorms that develop at the time of maximum diurnal heating. As a result, many of the precipitation features that formed during this period are short lived and small in size, which is characteristic of IPF. However, some of these IPF coalesced into broader regions of precipitation, denoted by MPF, particularly near Florida and over the oceans.

During this period, the western ridge of the North Atlantic Subtropical High (NASH) strongly dominated the SE US, shielding the majority of the region from midlatitude cyclones. However, midlatitude cyclones were still frequent across the northern portion of the domain, where most precipitation was delivered by squall lines and MPF. In the Carolinas and Mid Atlantic, weak frontal systems were observed, which enhanced precipitation, and contributed to the development of MPF. Away from these frontal systems, precipitation was modulated by the diurnal cycle of heating and cooling. Near the Gulf and Atlantic coasts, sea breeze fronts produced precipitation, mostly in the form of IPF. Surface and upper air maps from the Storm Prediction Center (SPC) for this period are shown in Appendix I.

3.2 WRF Model Setup

3.2.1 Study Domain

WRF-ARW version 3.5.1, as described by Skamarock et al. (2008), was set up with a 27 km parent domain over North America and two smaller 9 and 3 km nested domains centered over the continental US and the SE US, respectively (Figure 2). The 27 km domain extends from the Hudson Bay in Canada southward into Central America, including portions of the Caribbean and Atlantic and Pacific Oceans. The 9 km domain is centered over the contiguous US, and the 3 km domain is centered over the SE US, extending from the Ohio Valley into Florida, including western Louisiana and portions of the Gulf of Mexico and Atlantic Ocean. The location of the 3 km domain corresponds to the study site used in Rickenbach et al. (2015) to analyze climatological patterns of precipitation in the SE US using the NMQ dataset. The SE US has excellent radar coverage with few radar beam obstructions. For this reason, the NMQ dataset is useful for evaluating the performance of WRF in reproducing observed patterns of precipitation.

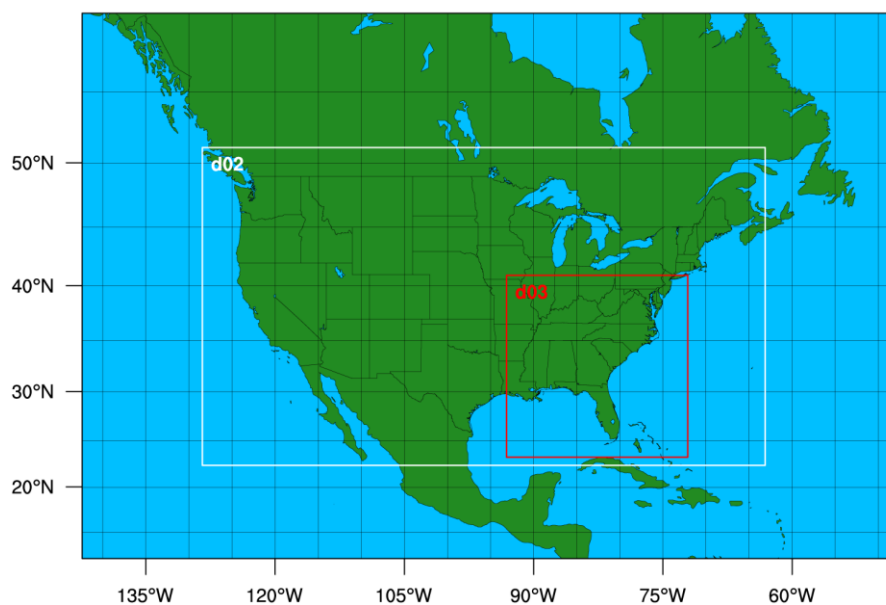


Figure 2 WPS domain configuration. The 27 km parent domain encompasses the full extent, the 9 km inner nest (d02) is boxed in white, and the 3 km innermost nest (d03) is boxed in red.

3.2.2 Data Sources

Initial conditions for WRF are provided by the Global Forecast System (GFS) Analysis dataset, a global 1° resolution dataset provided four times a day from March 2, 2004 to the latest full month (Anon n.d.). Sea surface temperature (SST) data is provided by the National Center for Environment Prediction's (NCEP) real-time, global sea surface temperature (RTG-SST) dataset. The RTG-SST is a global 0.5° resolution dataset of daily SSTs merged from ship, buoy, and satellite data from February 11, 2001 to present (Thiébaux et al. 2003). As SSTs do not change significantly throughout the duration of the simulation, WRF is run with static SSTs set at the initialization time.

3.2.3 Parameterizations

At horizontal resolutions less than 6 km, WRF is capable of explicitly resolving convective updrafts and downdrafts within thunderstorms, so cumulus parametrization is neglected for the 3 km domain. At this grid scale, WRF can resolve small-scale convective features associated with fronts, squall lines, mesoscale convective systems, and even sea breeze fronts. Due to their larger size, the 9 and 27 km domains use the Betts-Miller-Janjic (Janjić 1994) cumulus scheme. Boundary layer physics is provided by the Yonsei scheme (Hong et al. 2006). WRF has been configured with 50 vertical levels. The 3 and 9 km nested domains receive their boundary conditions from the parent domains using one-way nesting.

WRF model physics largely follow Lackmann (2013), which used an earlier version of WRF and had a similar area of interest. Surface physics are provided by the Noah land-surface model (Tewari et al. 2004), radiation physics from the Rapid Radiative Transfer Method for General Circulation Models (RRTMG, Iacono et al. 2008). The 9 and 27 km domains use the WRF Single Moment-3 (WSM3, Hong et al. 2004) microphysics, while WRF Single Moment-6

(WSM6, Hong & Lim 2006) is used in the 3 km domain. A complete list of physics options is shown in Table 3.

	Domain 1	Domain 2	Domain 3
Resolution	300 x 200	619 x 349	598 x 598
Grid spacing	27 km	9 km	3 km
Microphysics	WRF Single Moment 3	WRF Single Moment 3	WRF Single Moment 6
Cumulus	Betts-Miller-Janjic	Betts-Miller-Janjic	none (explicit)
Surface physics	Noah	Noah	Noah
LW/SW Radiation	RRTMG	RRTMG	RRTMG
Boundary layer	Yonsei	Yonsei	Yonsei

Table 3 WRF domain parameterizations.

3.2.4 WRF Output

WRF simulations are run for eight day periods, but results after the first 48 hours of the simulation are only included in the analysis. WRF output is created every 12 hours for the 27 and 9 km domains, and every 15 minutes for the 3 km domain. The temporal resolution of the 3 km domain matches the time interval at which the NMQ data was analyzed in Rickenbach et al. (2015), and allows the WRF output to be easily read into the Rickenbach et al. (2015) feature identification algorithm.

3.3 Future Climate Simulations

The future climate simulations were created using the same methodology employed by Lackmann (2013). The WRF Preprocessing System (WPS) combines atmospheric and SST data sources into an intermediate file known as *met_em*, which provides the model with initial and lateral boundary conditions. In this methodology, the future climate states are created by directly adding a multi-model mean (MMM) of temperature anomalies to the *met_em* files. The MMM anomalies consist of air and surface temperature anomalies for the 2090s averaged for five different CMIP5 GCMs from the IPCC AR5. In comparison, Lackmann (2013) used an average

of five different GCMs from the A2 emissions scenario in the IPCC AR4. A simplified rundown of this methodology is shown in Figure 3.

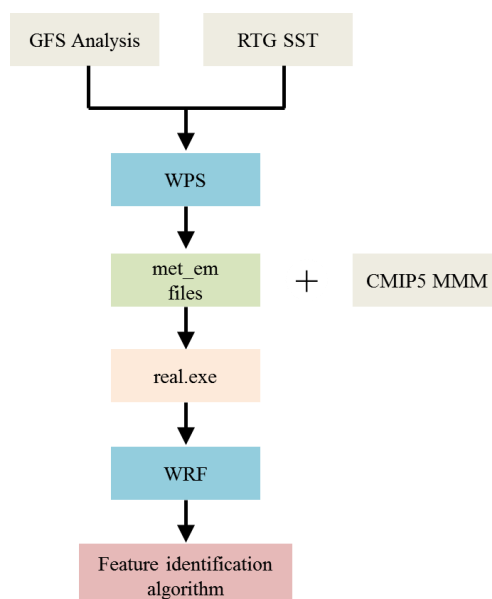


Figure 3 Simplified run-down of the creation of the future climate simulations from primary data sources and processes in WRF. *Real.exe* vertically and horizontally interpolates atmospheric data and hydrostatically balances the model, while the numerical integration occurs in WRF. The WRF output can be read directly into the Feature Identification Algorithm.

The CMIP5 GCM data was obtained from the Earth System Grid Federation (ESGF, Taylor et al. 2012) and the German Climate Computing Center (DKGZ), freely available online for registered users. Surface and air temperature data was obtained for the historical runs (spanning 1850 – 2005) and the RCP4.5 and RCP8.5 emission scenarios (spanning 2005 – 2100). Five CMIP5 GCMs were selected based on low error measures for 2 m, 850 mb, and 200 mb temperature in Flato et al. (2013). These include the Australian Community Climate and Earth-System Simulator (ACCESS), the Hadley Global Environment Model 2 and its Atmosphere and Earth System versions (HadGEM2-AO and HadGEM2-ES), Community Earth System Model – Biogeochemical Cycle (CESM1-BGC), and the Max Planck Institute Earth System Model running on Low Resolution (MPI-ESM-LR). These GCMs are believed to represent the best of

the CMIP5 and a range of different modeling institutions from around the world. A detailed list of these GCMs is shown in Table 4.

GCM	Ensemble	Institute	Country	Reference
ACCESS1-0	r1i1p1	CSIRO	Australia	Bi et al. (2013)
HadGEM2-AO	r1i1p1	NIMR-KMA	Korea	Martin et al. (2011)
HadGEM2-ES	r1i1p1	MOHC	England	Jones et al. (2011)
CESM1-BGC	r1i1p1	NSF-DOE-NCAR	USA	Hurrell et al. (2013)
MPI-ESM-LR	r1i1p1	MPI-M	Germany	Stevens et al. (2013)

Table 4 List of CMIP5 GCMs used in the creation of the MMM.

The MMM was created by subtracting the RCP4.5 and RCP8.5 monthly means for the 2090s from those in the historical run for the 1990s for each GCM and averaging them all together. This was completed for all three WRF domains for surface and air temperature. The modified *met_em* files were then read directly into WRF where the geopotential heights and moisture variables were recomputed. This methodology includes the assumption that relative humidity in the future warmer climate will remain unchanged from the present climate (Allen & Ingram 2002; Pall et al. 2007; Held & Soden 2006). For instance, if a location has a relative humidity of 75% at an air temperature of 20°C in the present climate, the dew point is recomputed to remain at 75% relative humidity at the future climate air temperature of 25°C.

3.4 Analysis

In order to verify the performance of the model and understand the changes in the future climate simulations, a number of different variables are analyzed. This analysis encompasses variables that define the synoptic-scale kinematic and thermodynamic environment, such as winds and sea level pressure. These variables can help explain the results from the Rickenbach et al. (2015) feature identification algorithm, which identifies IPF and MPF, and produces statistics on feature characteristics, such as feature length, height, and precipitation.

3.4.1 Synoptic-Scale Environment

The present and future climate simulations in WRF have been compared against the North American Regional Reanalysis (NARR, Mesinger et al. 2006), a 0.3° (32 km) high resolution reanalysis dataset available from 1979 to 2015, developed by the National Center for Environmental Prediction (NCEP). The NARR was created using NCEP's Eta model, and like most reanalysis datasets, the information in this dataset should be treated as a best estimate of the observed atmospheric conditions. This analysis examines the 850 and 250 mb winds and sea level pressures for the 9 km WRF domain, which covers the contiguous US. The 9 km domain provides a broader picture of the underlying synoptic weather pattern that is cropped out of the 3 km domain over the SE US. Average convective available potential energy (CAPE) and convective inhibition (CIN) were also examined in the 3 km domain. The WRF variables were calculated using NCL's built-in WRF functions.

CAPE and CIN are diagnostic variables that meteorologists often examine when the atmosphere is favorable for thunderstorms or severe weather. A plot of the atmospheric temperature and dew point profile on a Skew-T diagram can easily reveal regions of CAPE and CIN. CAPE can be understood as the amount of buoyant energy available to a parcel of air that no longer needs to be raised mechanically and can rise on its own. Typically, higher values of CAPE are associated with greater amounts of instability, and the higher potential for stronger and heavier rain-producing thunderstorms. CIN is the amount of energy that the parcel must overcome before it has access to CAPE. If CIN is too high, then it might suppress thunderstorm activity entirely, but if CIN is too low, thunderstorms can form more easily.

As Doswell & Schultz (2006) pointed out, CAPE is the superposition of moisture and conditional instability. As such, CAPE typically reaches its highest values during the late

afternoon and early evening when the maximum diurnal temperature is achieved, which is when conditional instability is at its highest. If the maximum temperature is higher in the future climate simulations, CAPE should be expected to increase as well. Therefore, CAPE and CIN can provide helpful insight into understanding the thermodynamic effect of the warmer temperatures on precipitation in the future climate simulations.

3.4.2 Feature Identification Algorithm

The feature identification algorithm computes IPF and MPF feature lengths, heights, and total feature precipitation from maps of instantaneous rainrates. These variables have already been computed for NMQ, as the identification algorithm was originally designed for this dataset. The identification algorithm was modified to ingest output from WRF. Rainrates in WRF were calculated by dividing instantaneous precipitation totals by the instantaneous model time step, which varies due to the use of the adaptive time step option in WRF. WRF echo heights were calculated by identifying the geopotential height that corresponded to the highest level with reflectivity greater than or equal to 18 dBZ, which corresponds roughly to drizzle-sized precipitation particles within a cloud, and is used by the Tropical Rainfall Measuring Mission (TRMM) satellite dataset for climate studies of echo top height (Rickenbach et al. 2015).

CHAPTER 4: RESULTS

SE US precipitation for the 17-22 June 2010 period was modeled in WRF under the present and future climates using PGW. Precipitation during this period was mostly in the form of afternoon thunderstorms, while areas in the northern portion of the domain were affected by transient frontal systems. This period is therefore characterized by summertime convection with little midlatitude influence. This period is also well-documented in the NMQ dataset, thereby providing a good metric for evaluating WRF's performance in producing precipitation.

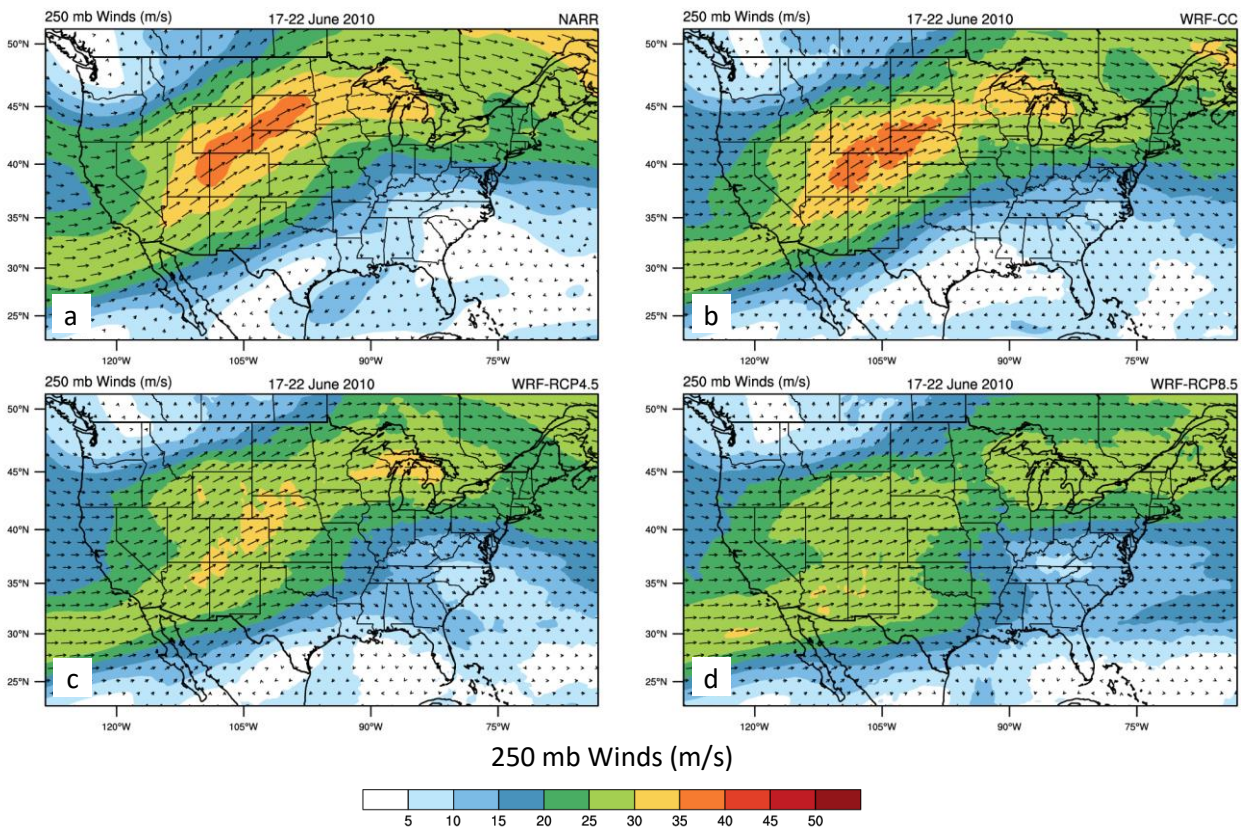


Figure 4 Upper-level winds (m/s) at 250 mb averaged 0 UTC 17 June to 0 UTC 23 June in (a) NARR, (b) WRF-CC, (c) WRF-RCP4.5, and (d) WRF-RCP8.5.

In the first step of this analysis, the results from the current climate WRF simulation (WRF-CC) are compared to the observations from NARR for synoptic-scale kinematic and thermodynamic variables and to the observed precipitation organization from NMQ (Rickenbach et al. 2015). The next step of this analysis is the comparison of WRF-CC to the future climate

WRF simulations under the RCP4.5 (WRF-RCP4.5) and RCP8.5 (WRF-RCP8.5) emission scenarios.

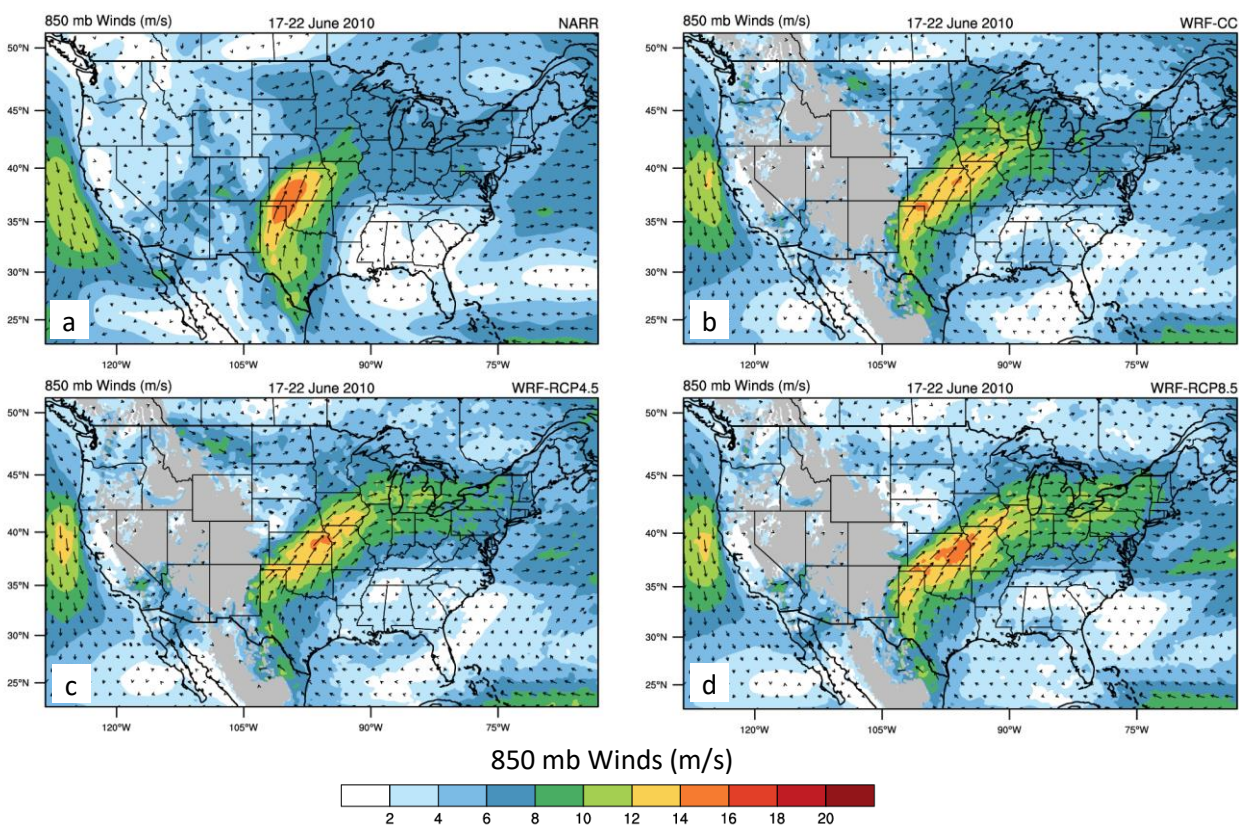


Figure 5 Same as Figure 4, but for lower-level winds (m/s) at 850 mb.

4.1 Synoptic-Scale Environment

The synoptic-scale weather conditions were assessed using the 9 km domain, which encompasses the contiguous US. Figures 4 and 5 show the upper and lower-level winds and SLP from NARR and WRF-CC, WRF-RCP4.5, and WRF-RCP8.5 averaged for the 17-22 June 2010 study period. Differences between NARR and WRF-CC as well as differences between WRF-CC and WRF-RCP4.5 and WRF-RCP8.5 are shown in Figures 6 and 7.

4.1.1 850 and 250 mb Winds

Model Evaluation. At 250 mb, the southern tip of a trough is located over Washington State with a southwesterly jet stream that stretches from Arizona to the Great Lakes. The magnitude and position of this upper-level jet stream in WRF-CC (Figure 4b) compared well to the observed jet in NARR (Figure 4a). However, WRF-CC did not resolve the 10-15 m/s upper-level southwesterly jet streak over the northern Gulf of Mexico (Figure 6a). In the low-levels, WRF-CC captured the correct placement of the Great Plains low-level jet (Figure 5b), but it was 3-5 m/s weaker in magnitude compared to NARR (Figure 5a). WRF-CC also produced a 4-6 m/s 850 mb southwesterly jet over the SE US (Figure 5b), which was not present in NARR (Figure 5a).

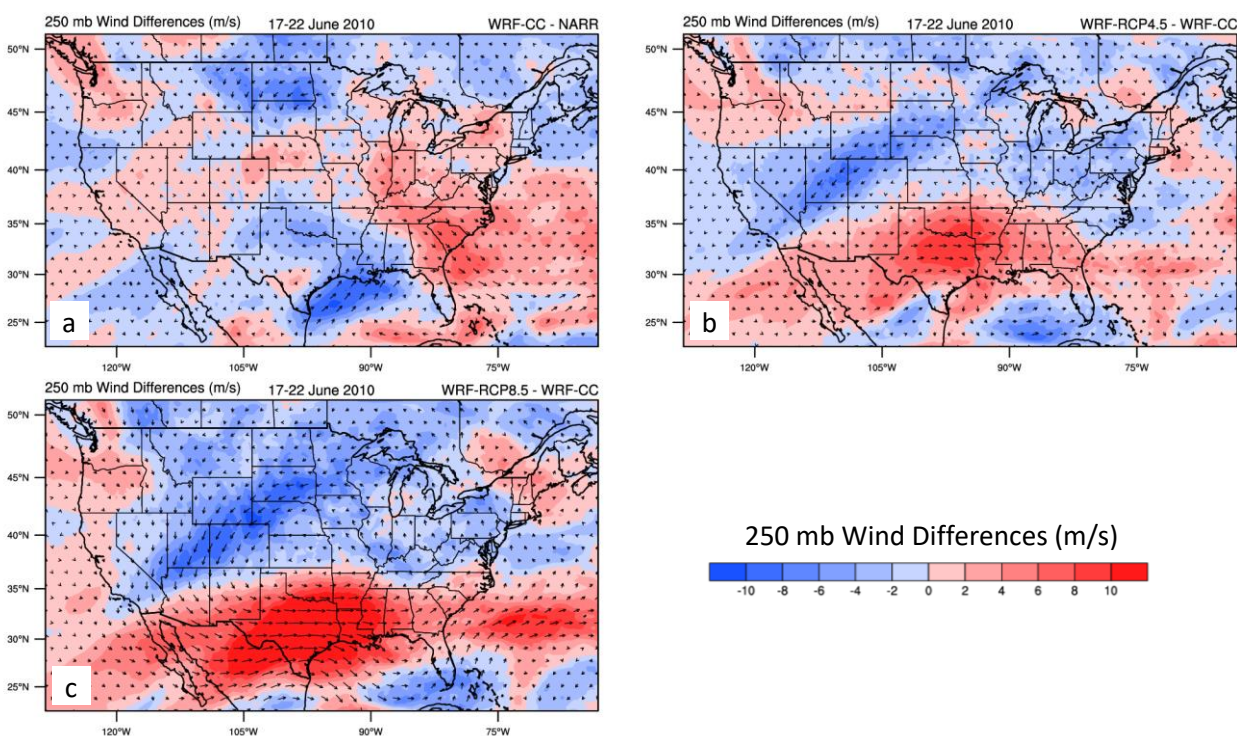


Figure 6 Upper-level wind differences (m/s) at 250 mb between (a) NARR and WRF-CC, (b) WRF-RCP4.5 and WRF-CC, and (c) WRF-RCP8.5 and WRF-CC.

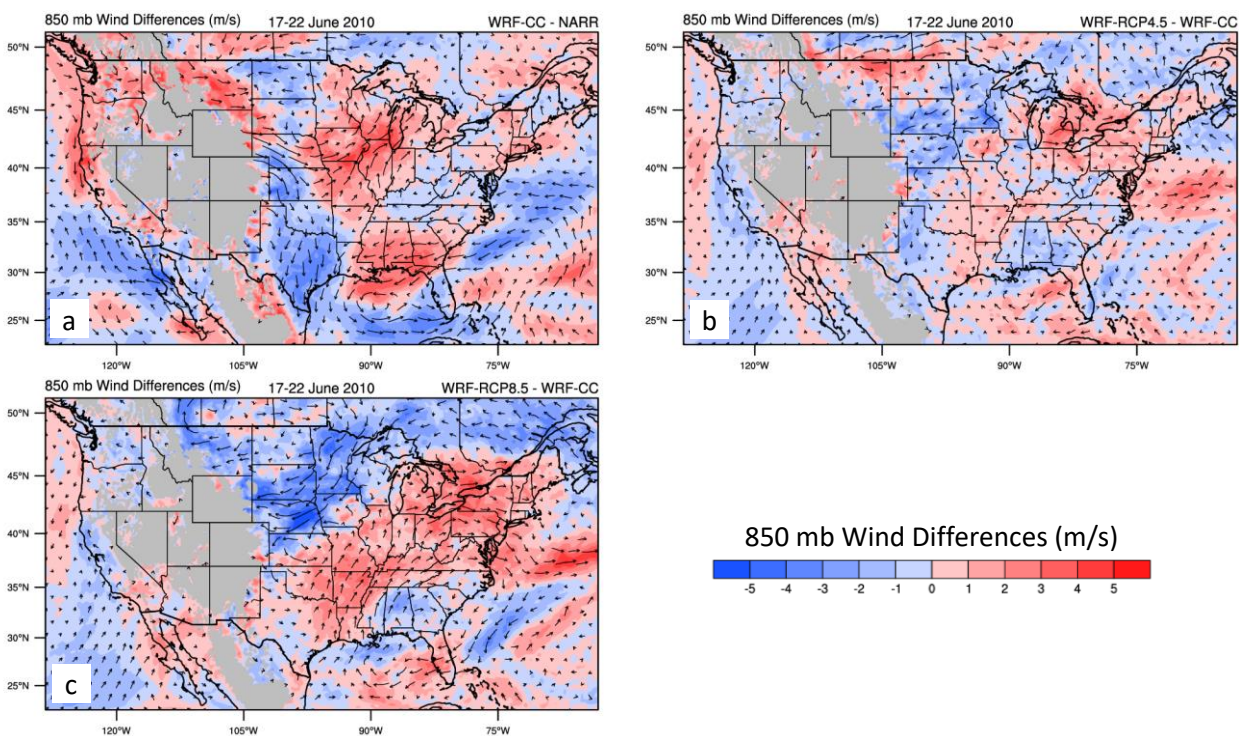


Figure 7 Same as Figure 6, but for lower-level winds (m/s) at 850 mb.

Future Climates. The 250 mb upper-level jet stream over the central US became progressively weaker in WRF-RCP4.5 (Figure 4c) and WRF-RCP8.5 (Figure 4d). As the 250 mb upper-level jet stream weakened in magnitude, it broadened and extended further south in WRF-RCP4.5 (Figure 6b) and WRF-RCP8.5 (Figure 6c). This broadening is consistent with southern shift in the upper-level jet stream already observed in recent years (Wang et al. 2010). The upper-level jet stream weakened by 6-8 and 8-10 m/s, respectively in WRF-RCP4.5 (Figure 6b) and WRF-RCP8.5 (Figure 6c). On the other hand, the 850 mb lower-level jet strengthened over Oklahoma in WRF-RCP4.5 (Figure 5b) and WRF-RCP8.5 (Figure 5c). The lower-level jet strengthened by 1-2 and 3-4 m/s, respectively, in WRF-RCP4.5 (Figure 7b) and WRF-RCP8.5 (Figure 7c) compared to WRF-CC. Interestingly, this made the 850 mb lower-level wind flow more similar to NARR (Figure 5a) than WRF-CC.

4.1.2 Sea Level Pressure

Model Evaluation. During the study period, a low-level trough extended southward along the Great Plains from the Dakotas to New Mexico, while the western ridge of the North Atlantic Subtropical High (NASH) dominated the eastern US. Over the continental US and eastward of the Rockies, sea level pressures in WRF-CC (Figure 8b) were generally lower than in NARR (Figure 8a). In particular, the western ridge of the North Atlantic Subtropical High (NASH) was weaker in WRF compared to NARR as seen by the wide region of negative SLP differences in excess of 2 mb over Gulf of Mexico and parts of Florida and the Bahamas (Figure 9a). The weaker NASH in WRF-CC may have contributed to the weaker WRF-CC Great Plains low-level jet discussed earlier.

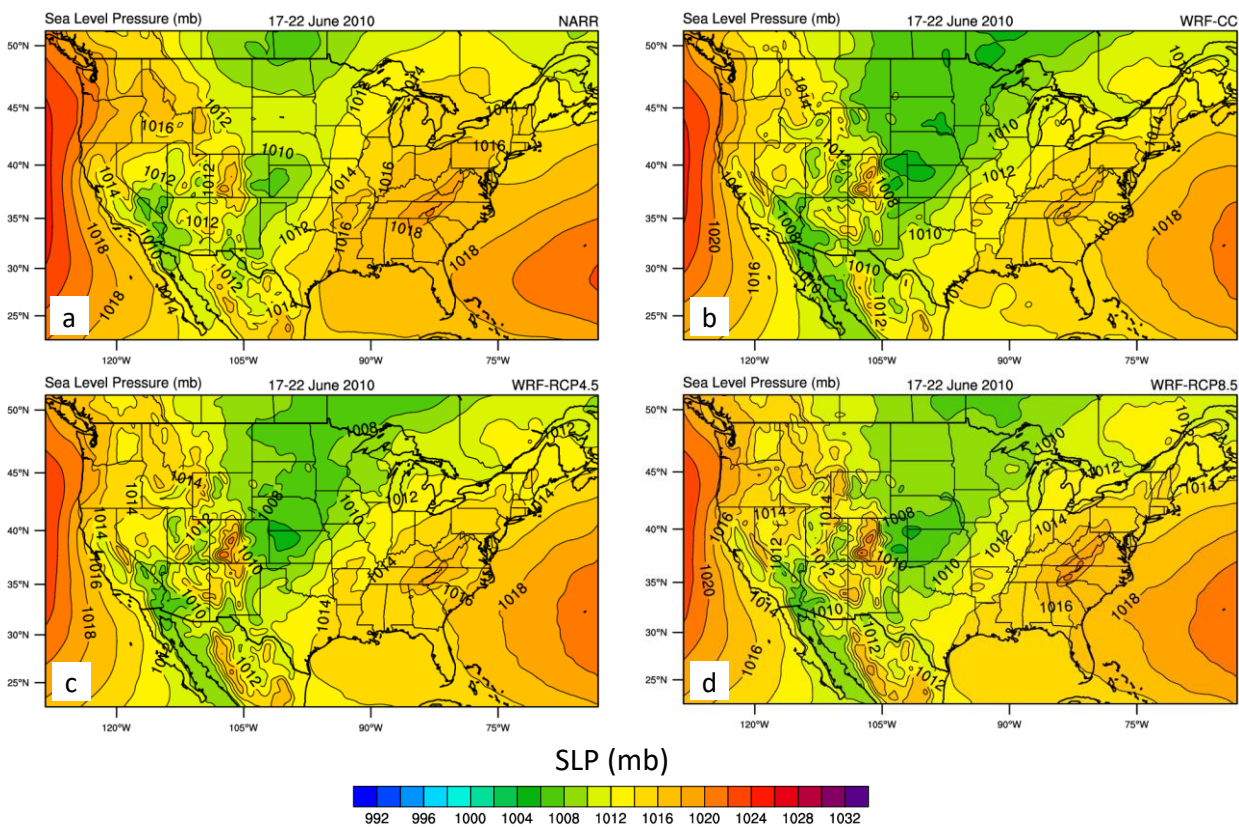


Figure 8 Sea level pressure (mb) averaged over 0 UTC 17 June to 0 UTC 23 June in (a) NARR, (b) WRF-CC, (c) WRF-RCP4.5, and (d) WRF-RCP8.5.

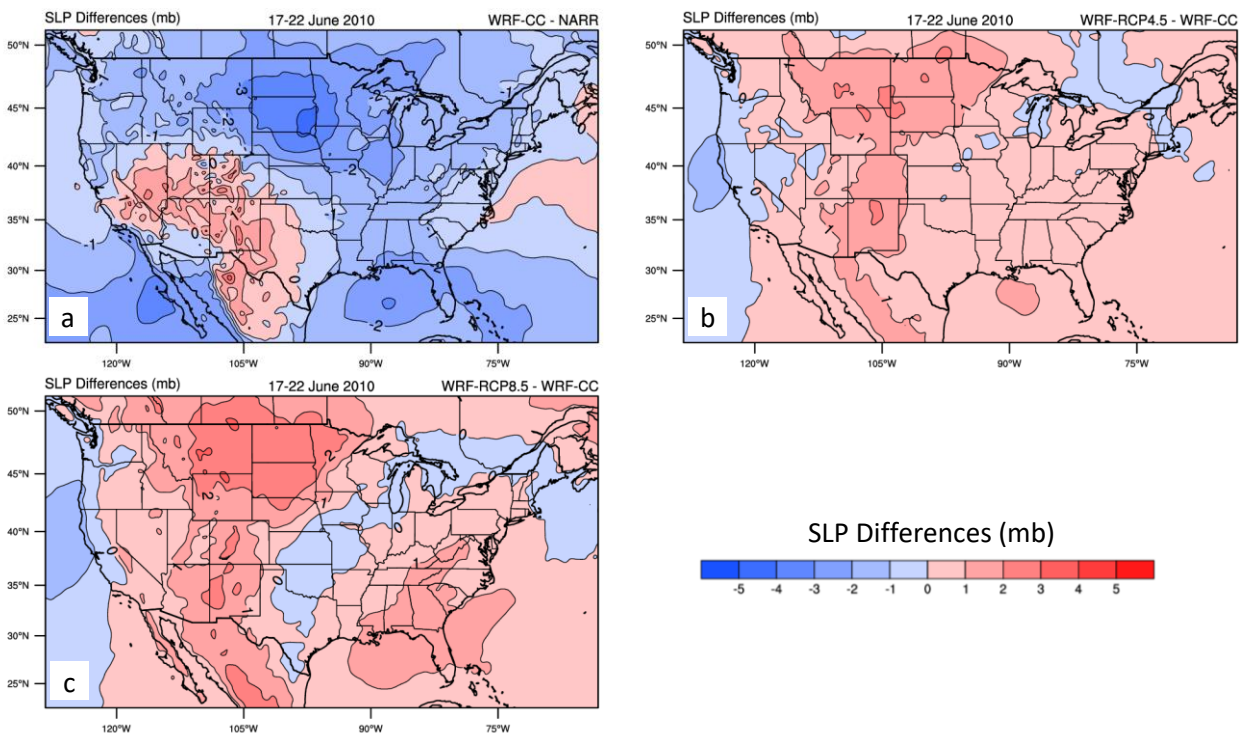


Figure 9 Same as Figure 6, but for sea level pressure differences (mb).

Future Climates. Sea level pressure increased slightly over the eastern US in WRF-RCP4.5 (Figure 9b) and in WRF-RCP8.5 (Figure 9c). In WRF-RCP8.5, sea level pressures east of the Rockies increased further, with the largest increases in excess of 2 mb seen over the northern plains (Figure 9c). Interestingly, sea level pressures actually decreased slightly over the central US., near the location of the enhanced 850 mb lower-level jet discussed earlier (Figure 7c). The western ridge of the NASH strengthened in WRF-RCP8.5, with an expansive region of positive anomalies in excess of 1 mb over a large portion of the SE US (Figure 9c). The stronger NASH may have contributed to the strengthened Great Plains low-level jet in WRF-RCP8.5.

4.1.3 CAPE and CIN

Model Evaluation. The diurnal cycle of CAPE over land in NARR had a 9 UTC minimum of about 1000 J/kg followed by a 0 UTC peak of 2300 J/kg (Figure 10b). Although WRF-CC simulated this pattern of the diurnal cycle, it had lower values of CAPE than NARR by as much

as 600 J/kg in the afternoon (Figure 10b). Over the ocean, CAPE in NARR was very large (2400-2600 J/kg) and its diurnal cycle had a maximum at 0 UTC and a minimum at 9 UTC, similar to the land (Figure 10b). However, the WRF-CC diurnal cycle of CAPE over the ocean had a maximum at 6 UTC and a minimum at 18 UTC, which is out-of-phase with the observed diurnal cycle (Figure 10b). CAPE values over the ocean differed by as much as 400-600 J/kg throughout the day (Figure 10b). Again, CAPE values in WRF-RCP4.5 were more similar to NARR than in WRF-CC (Figure 10).

CIN in WRF-CC compared well to NARR, with only slight differences on the order of 5-8 J/kg at 6 UTC and 18 UTC (Figure 11a). CIN values over the land compared well between the two datasets, but WRF-CC produced roughly 5 J/kg less CIN over the ocean than in NARR regardless of the hour (Figure 11b).

Future Climates. As the climate warms, CAPE increases. CAPE in WRF-RCP4.5 and WRF-RCP8.5 was greater than WRF-CC by roughly 300 and 700 J/kg, respectively (Figure 10a). Over land, increases in CAPE were larger, on the order of 400 and 900 J/kg, respectively, in the WRF-RCP4.5 and WRF-RCP8.5 simulations (Figure 10b). Over the ocean, CAPE increased by 400 and 800 J/kg, respectively, in WRF-RCP4.5 and WRF-RCP8.5 (Figure 10b). The diurnal minimum and maximum of CAPE over the land and ocean in the future climate simulations occurred at the same hours as in WRF-CC.

CIN in WRF-RCP4.5 and WRF-RCP8.5 increased by roughly 8 and 12 J/kg, respectively (Figure 11a). The largest increases in CIN were seen over the land, where increases by as much as 10 J/kg were seen in WRF-RCP4.5 and WRF-RCP8.5 (Figure 11b). Smaller increases by 5 J/kg were seen over the ocean in the future climate simulations (Figure 11b). CIN in WRF-

RCP8.5 was more similar to NARR than in WRF-CC. The diurnal maximum and minimum of CIN in the future climate simulations once again occurred at the same hours as WRF-CC.

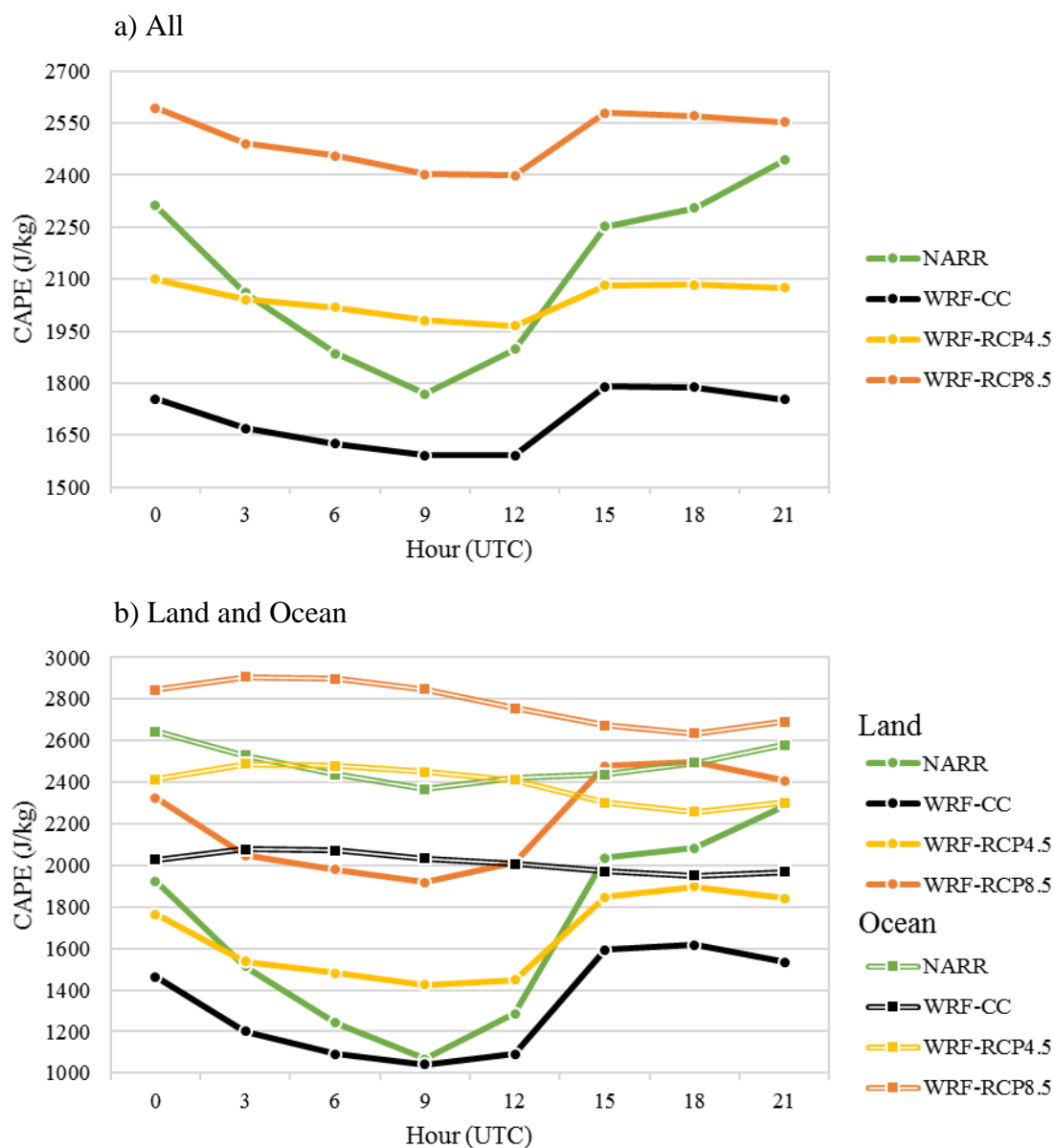


Figure 10 Three-hourly Convective Available Potential Energy (CAPE, J/kg) averaged over the 3 km domain from 0:00 UTC 17 June to 0:00 UTC 23 June 2010 in the NARR reanalysis dataset and the WRF-CC, WRF-RCP4.5, and WRF-RCP8.5 simulations for (a) the entire domain and (b) the land (solid line) and ocean (hollow line).

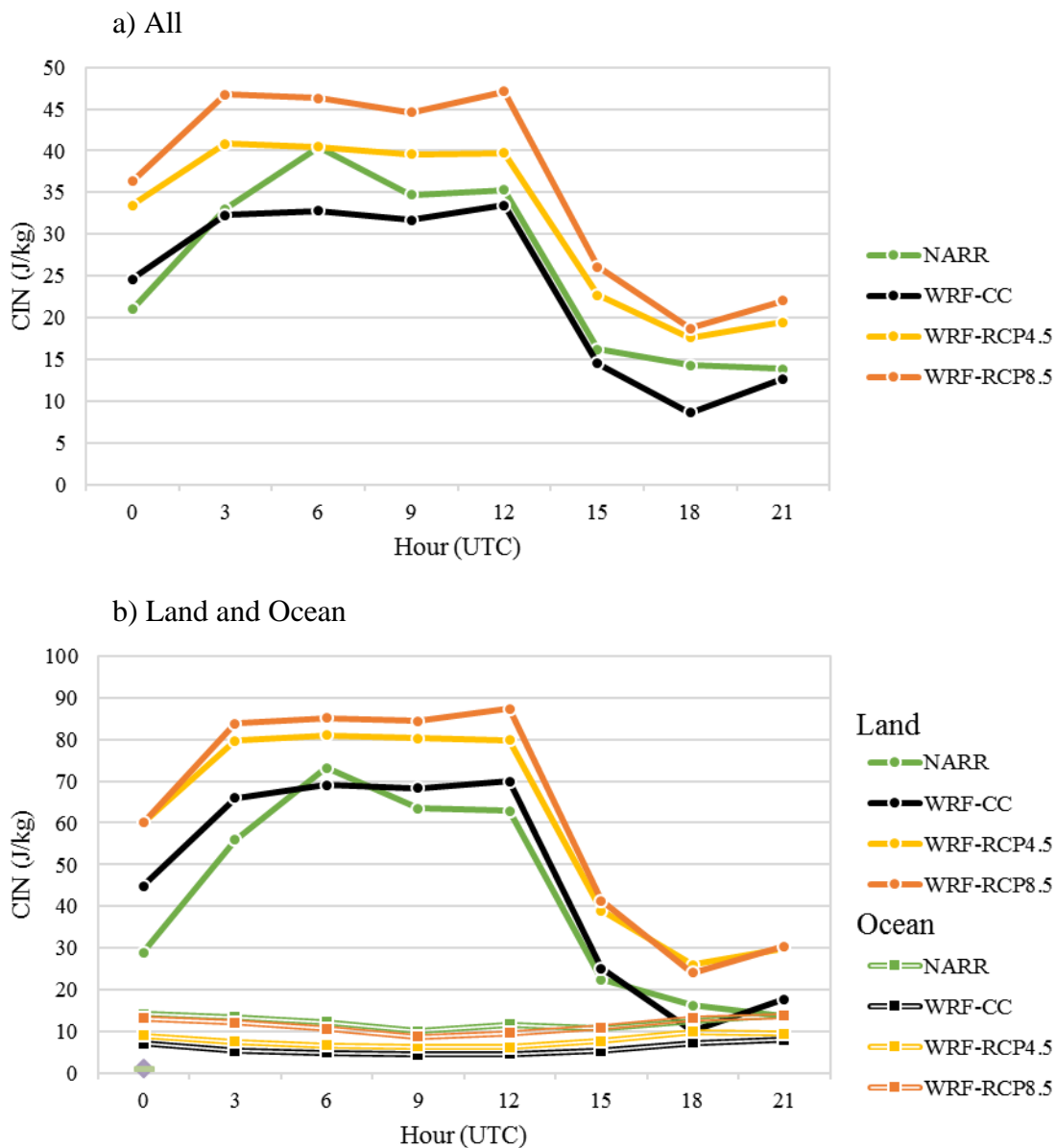


Figure 11 Same as Figure 10, but for Convective Inhibition (CIN, J/kg).

4.2 Total Accumulated Precipitation

Total precipitation within the 3 km WRF domain was evaluated and compared to the observations in the NMQ dataset. Both WRF and NMQ precipitation data were analyzed using the Rickenbach et al. (2015) feature identification algorithm where precipitation features were partitioned into either IPF or MPF on the basis of their maximum feature length. IPF and MPF total precipitation was further partitioned according to their location over the land or ocean. Since the NEXRAD data only extends to about 250 km offshore, the oceanic domains of WRF and NMQ were very different. To account for this, an approximately 250 km offshore ocean buffer was applied to the WRF precipitation results (Figure 12). The future climate simulation comparisons, however, were performed without the masked region.

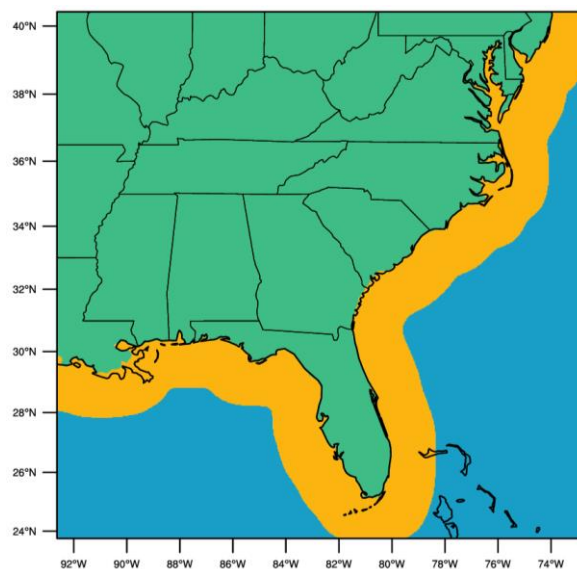


Figure 12 The 250 km offshore ocean buffer (yellow) used to compare oceanic precipitation in WRF that is common to NMQ.

4.2.1 Total Precipitation

Model Evaluation. Total accumulated precipitation in NMQ (Figure 13a) and in WRF-CC (Figure 14a) compared well, with similar precipitation magnitudes. Total average accumulated precipitation for all precipitation features combined were similar for WRF-CC and NMQ (Table

5), although WRF-CC tended to produce higher precipitation amounts (by 6.8 mm) than NMQ over land but lower precipitation amounts than NMQ over the ocean (by 3.71 mm, Table 5).

Dataset	Totals			Land			Ocean Buffer		
	All	IPF	MPF	All	IPF	MPF	All	IPF	MPF
NMQ	24.13	12.55	11.58	22.62	10.59	12.02	25.64	14.50	11.14
WRF-CC	25.67	19.82	5.85	29.42	19.97	9.45	21.93	19.68	2.25

Table 5 Area average total accumulated IPF and MPF precipitation (mm) measured over 0:00 UTC 17 June to 0:00 UTC 23 June 2010 in NMQ and WRF-CC across the land plus ocean buffer, land, and ocean buffer. Bolded values represent differences significant to the 95% level.

WRF-CC produced less precipitation across northern Florida, southern Alabama, and coastal Georgia, South Carolina, and North Carolina, where the sea breeze had been the main driver of precipitation during this period (Figure 17a). WRF-CC also produced less precipitation over Indiana and Illinois, but more precipitation across Ohio, West Virginia, and areas eastward (Figure 17a), where transient frontal systems entered the area of interest. WRF-CC did not reproduce the large precipitation maximum in the Gulf Stream off the SE US coast pictured in Figure 17a. WRF-CC did, however, reproduce the observed precipitation minimum offshore from Florida, Georgia, and South Carolina (Figure 17a).

Future Climates. In comparison with WRF-CC, the average total accumulated precipitation across the entire domain in WRF-RCP4.5 and WRF-RCP8.5 increased by 1.68 and 12.08 mm, respectively (Table 6). In WRF-RCP8.5, precipitation across the entire domain was 38.79 mm, 12.08 mm higher than in WRF-CC with significant precipitation increases over both the land and ocean (Table 6). Overall, the largest precipitation increases in WRF-RCP8.5 occurred over the ocean (Table 6).

Dataset	Totals			Land			Ocean		
	All	IPF	MPF	All	IPF	MPF	All	IPF	MPF
WRF-CC	26.71	20.82	5.89	29.42	19.97	9.45	24.00	21.68	2.32
WRF-RCP4.5	28.39	23.13	5.26	26.27	18.08	8.19	30.51	28.18	2.33
WRF-RCP8.5	38.79	29.05	9.74	37.55	24.18	13.38	40.03	33.93	6.10

Table 6 Area average total accumulated IPF and MPF precipitation (mm) measured over 0:00 UTC 17 June to 0:00 UTC 23 June 2010 in WRF-CC, WRF-RCP4.5, and WRF-RCP8.5 across the land plus ocean, land, and ocean. Bolded values indicate future climates differences that are significant to the 95% level compared to the current climate.

Total accumulated precipitation in WRF-RCP4.5 and WRF-RCP8.5 is shown in Figures 15 and 16. In WRF-RCP4.5, precipitation decreased over the Midwest and Ohio valley, but increased across portions of the Carolinas, the Gulf of Mexico, and the Gulf Stream. Interestingly, WRF-RCP4.5 resolved the Gulf Stream precipitation that was present in NMQ (Figure 13a) and not in WRF-CC (Figure 14a). The Gulf Stream precipitation disappeared again in WRF-RCP8.5 (Figure 16a). It is odd that although WRF-RCP4.5 produced more IPF precipitation over the Gulf Stream compared to WRF-CC as expected, WRF-RCP8.5 produced very little IPF over the Gulf Stream, even less than WRF-CC. This is a very unexpected aspect of WRF-RCP8.5 that is interesting and requires further study. In WRF-RCP8.5, precipitation decreased over Kentucky, but increased over the northwestern portion of the domain, where transient frontal systems entered the region (Figure 19a). Precipitation over the Gulf of Mexico and off the coast of Florida increased further from WRF-RCP4.5 (Figure 19a).

4.2.2 IPF and MPF Precipitation

Model Evaluation. While the average total accumulated precipitation in WRF-CC is very similar to the observations (Table 5), the model produced an unrealistically large amount of precipitation from IPF (57% more than NMQ), with much less precipitation from MPF (49% less than NMQ). This bias towards IPF precipitation was present in both the land and ocean buffer (Table 5). IPF

precipitation in NMQ (Figure 13b) and WRF-CC (Figure 14b) had similar horizontal distributions with high values over the ocean and inland near the coast (Figure 17). Although MPF precipitation was weaker in the model than in the observations, the spatial distribution was similar. There is a maximum of MPF precipitation over Florida and the Gulf of Mexico. The precipitation maximum associated with midlatitude forcing over the northern part of the domain is displaced eastward of its location in the observations, which might indicate that the frontal systems were located farther east in WRF-CC. The observed MPF precipitation maximum over the Gulf Stream is not present in WRF-CC.

Future Climates. In WRF-RCP4.5, statistically significant increases in total IPF precipitation occurred over the ocean amounting to 6.5 mm (Table 6). No significant changes in MPF precipitation occurred in WRF-RCP4.5. Significant precipitation increases occurred in WRF-RCP8.5, with total overall increases in IPF and MPF precipitation by 8.23 and 3.85 mm, respectively (Table 6). Again, total IPF precipitation increased much more over the ocean (by 12.25 mm) than over land (by 4.21 mm) in WRF-RCP8.5, with significant increases in IPF and MPF precipitation over both the land and ocean (Table 6).

IPF precipitation in WRF-RCP4.5 increased over the Gulf of Mexico, coastal North and South Carolina, and over the Gulf Stream (Figure 18b). In WRF-RCP8.5, IPF precipitation further increased over the Gulf of Mexico and off the coast of Florida, but changed very little over the Gulf Stream (Figure 19b). In WRF-RCP4.5, MPF precipitation increased across the Midwest, South Carolina, the Gulf of Mexico, and over Florida (Figure 18c). Further increases in MPF precipitation occurred in WRF-RCP8.5 (Figure 19c).

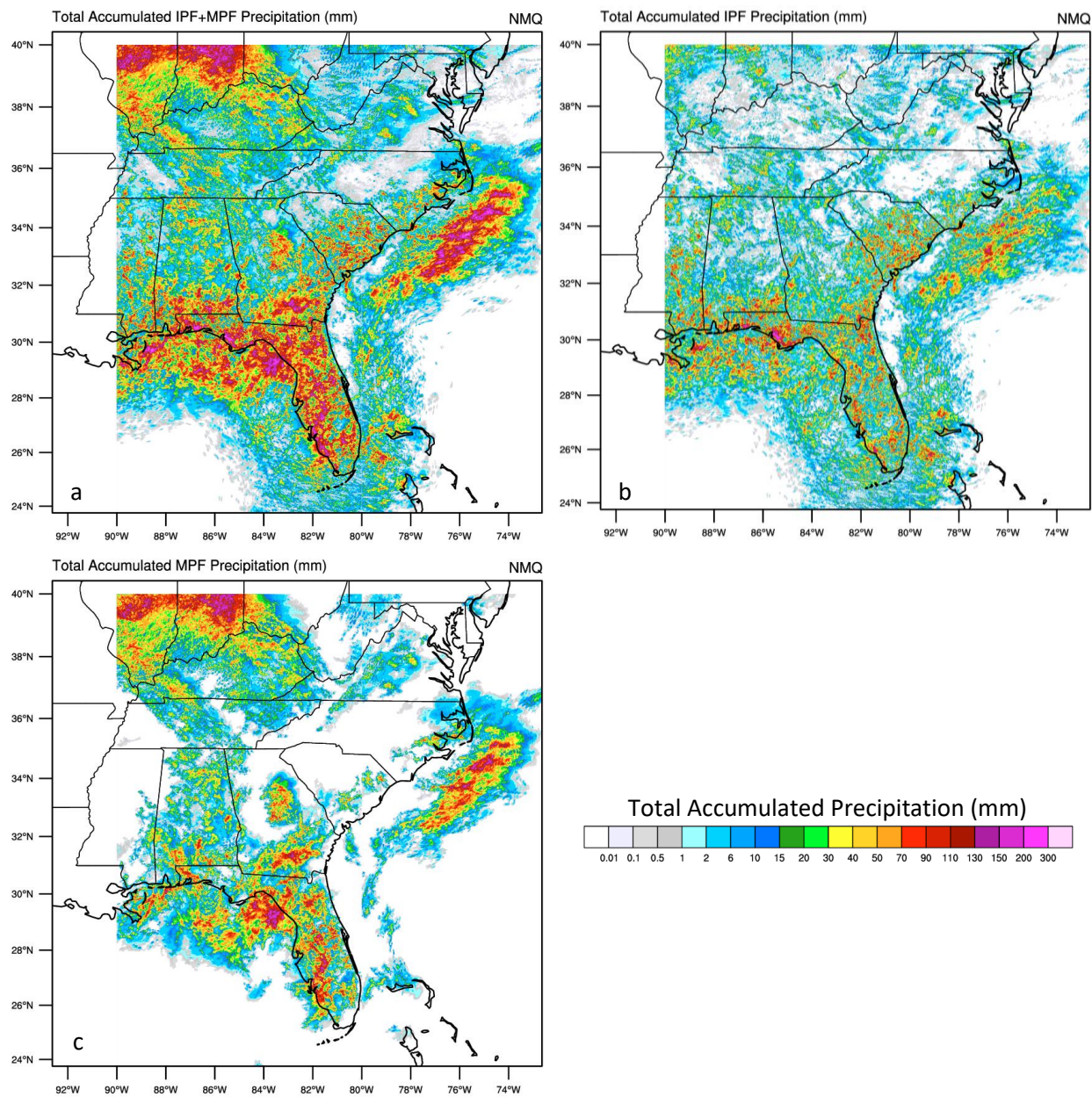


Figure 13 Observed values of total accumulated precipitation (mm) measured over 0:00 UTC 17 June to 0:00 UTC 23 June 2010 in the NMQ dataset for (a) combined IPF and MPF precipitation, (b) IPF precipitation, and (c) MPF precipitation.

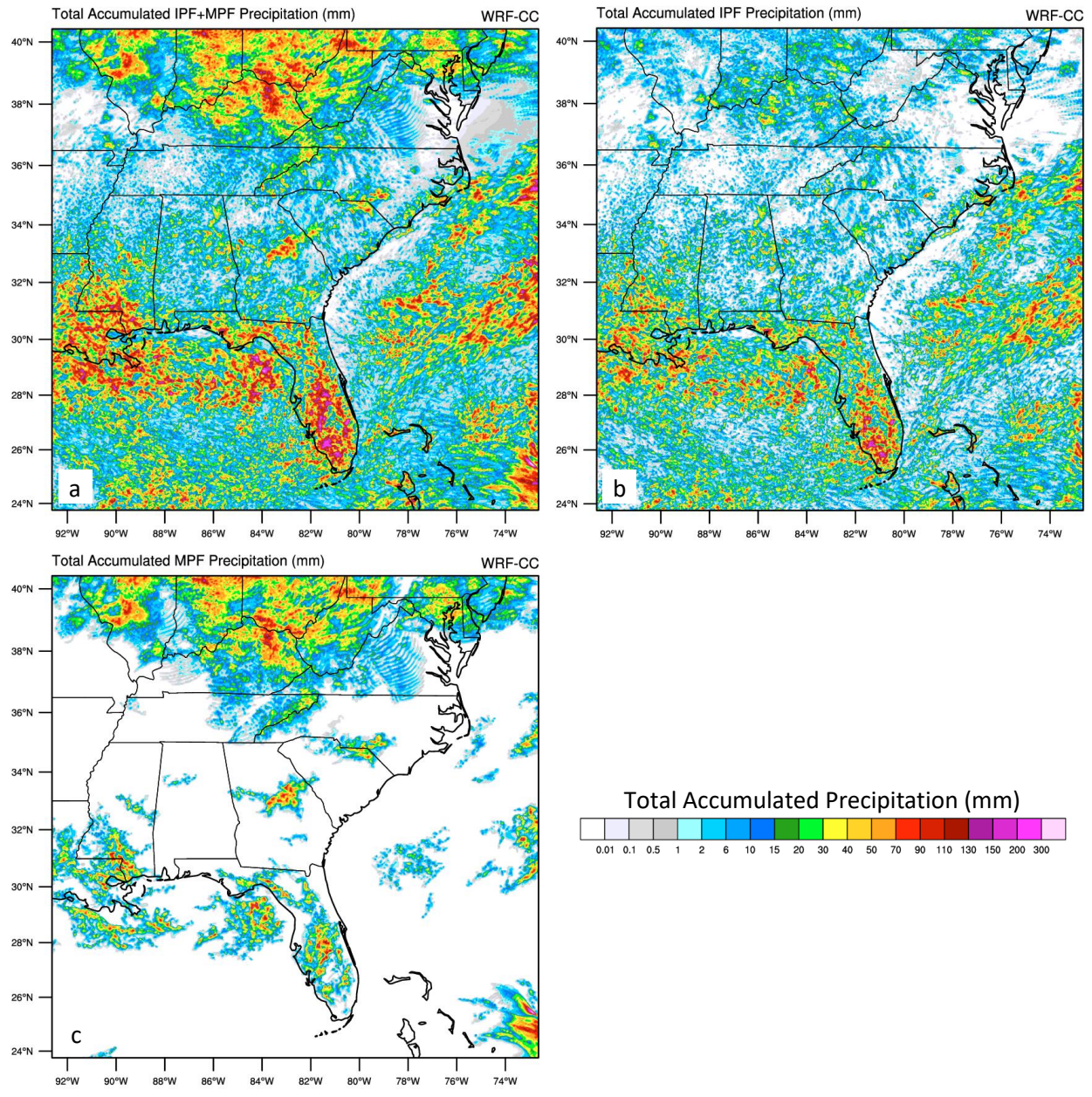


Figure 14 Same as Figure 13, but for WRF-CC.

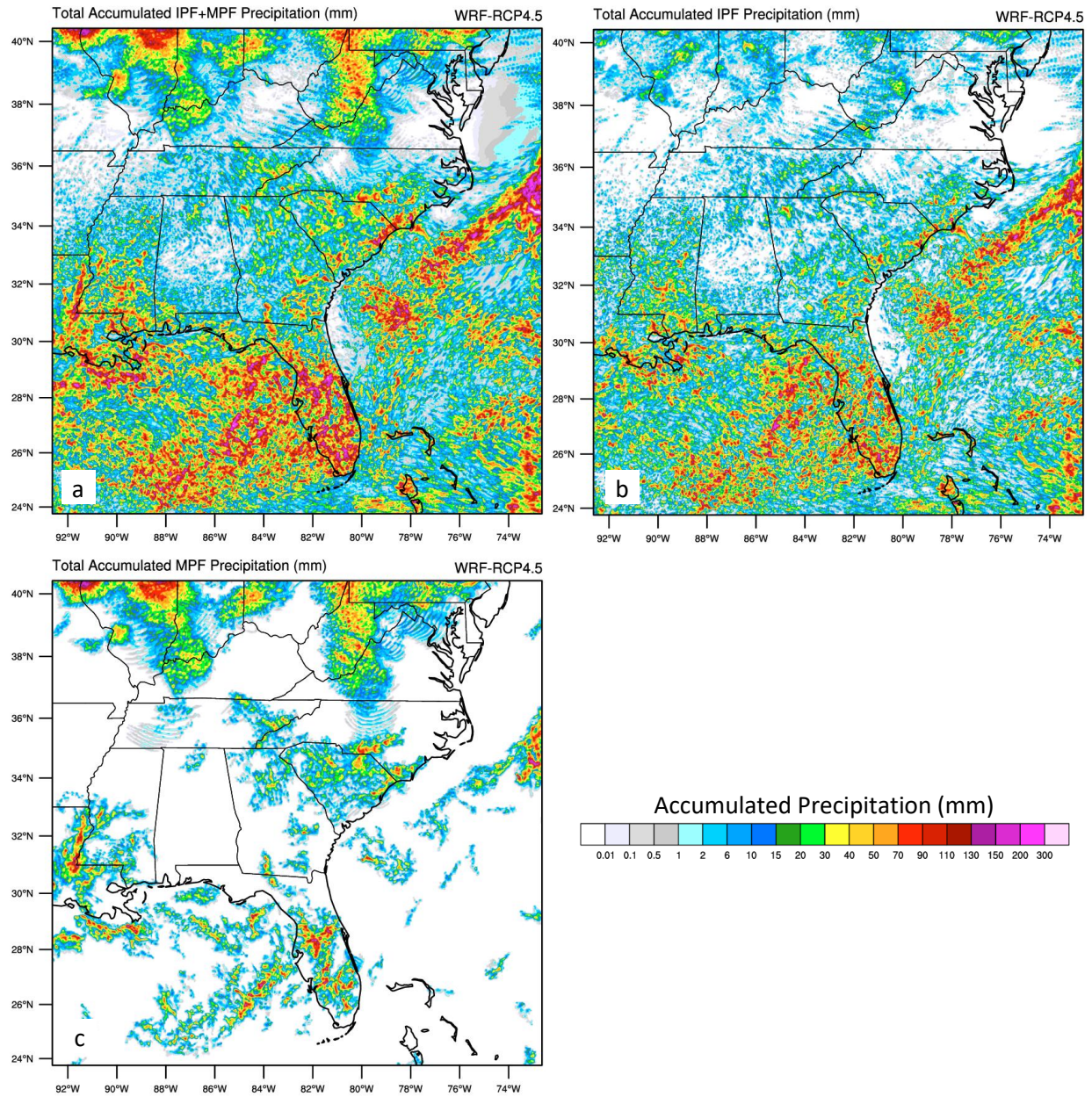


Figure 15 Same as Figure 13, but for WRF-RCP4.5.

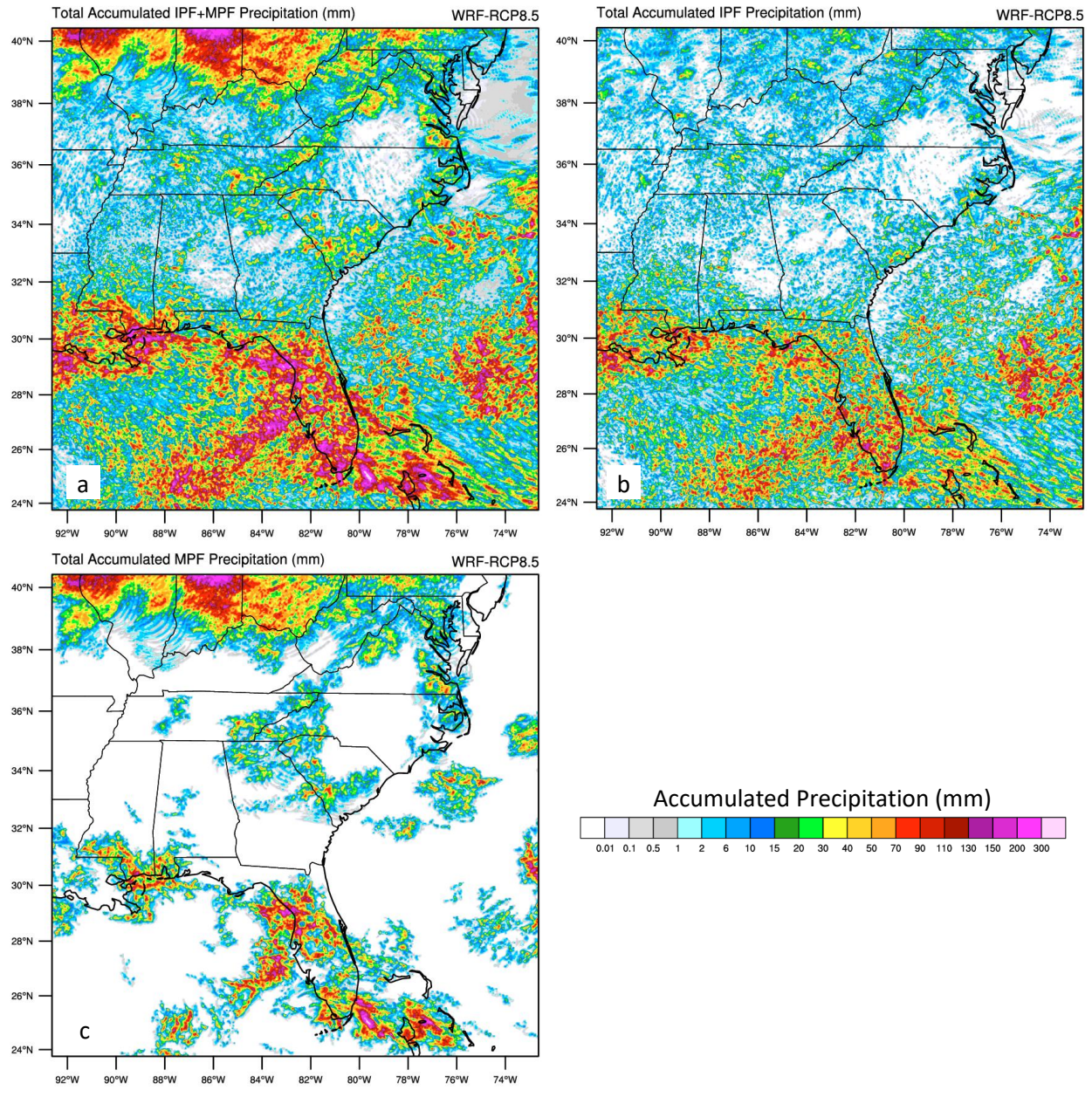


Figure 16 Same as Figure 13, but for WRF-RCP8.5.

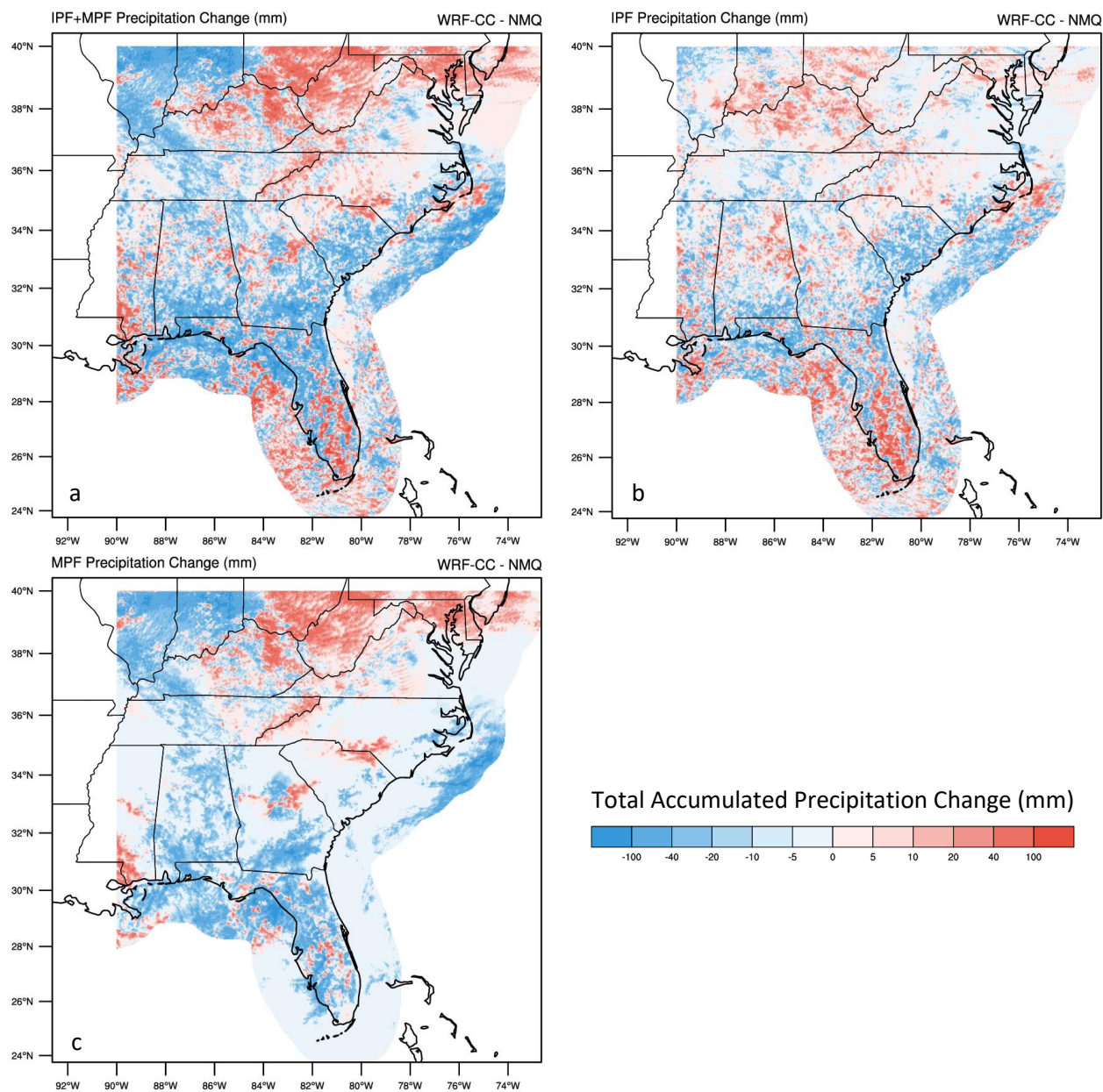


Figure 17 Differences in total accumulated precipitation (mm) between WRF-CC and NMQ for (a) combined IPF and MPF precipitation, (b) IPF precipitation, and (c) MPF precipitation.

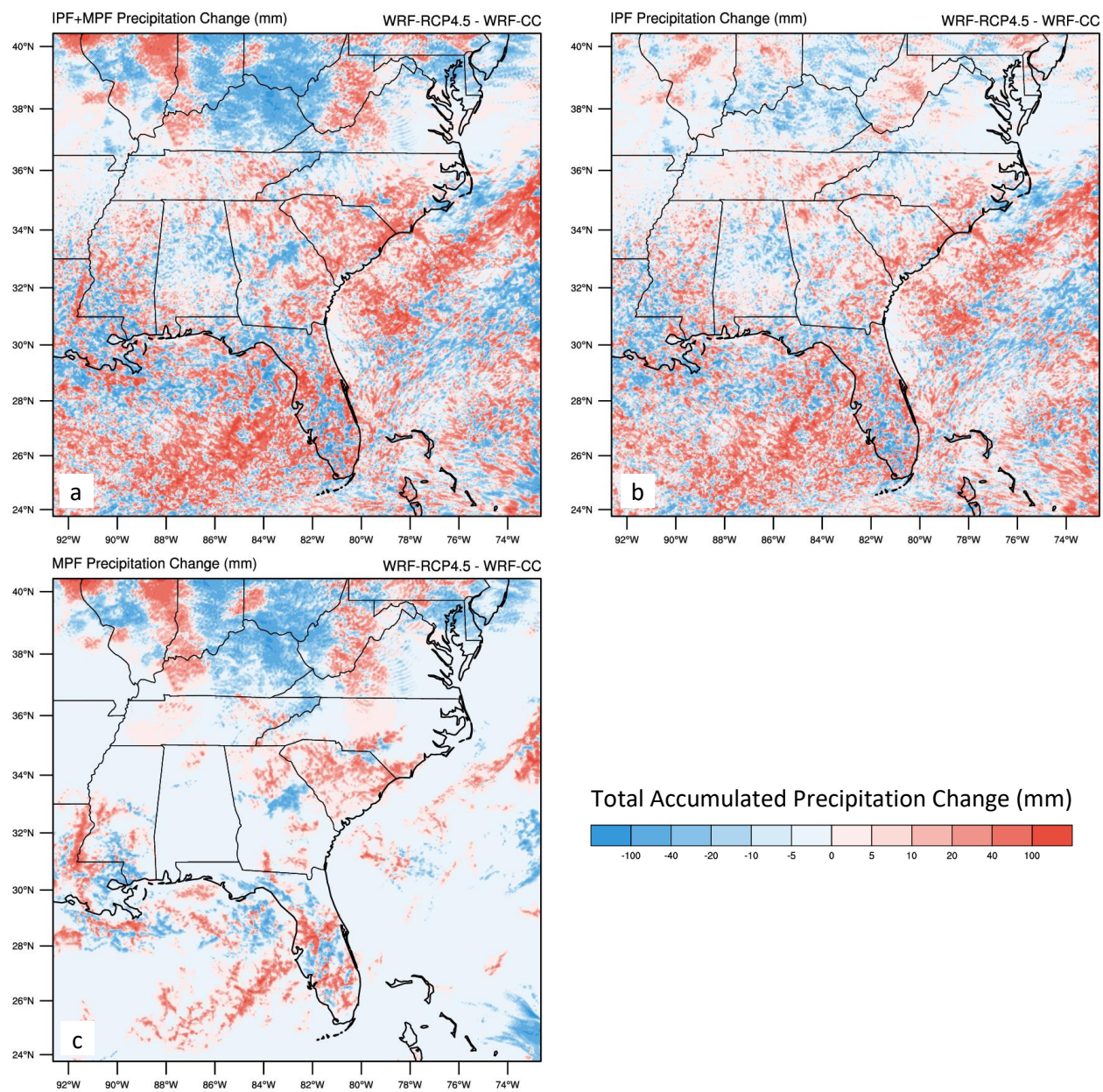


Figure 18 Same as Figure 17, but for WRF-RCP4.5 and WRF-CC.

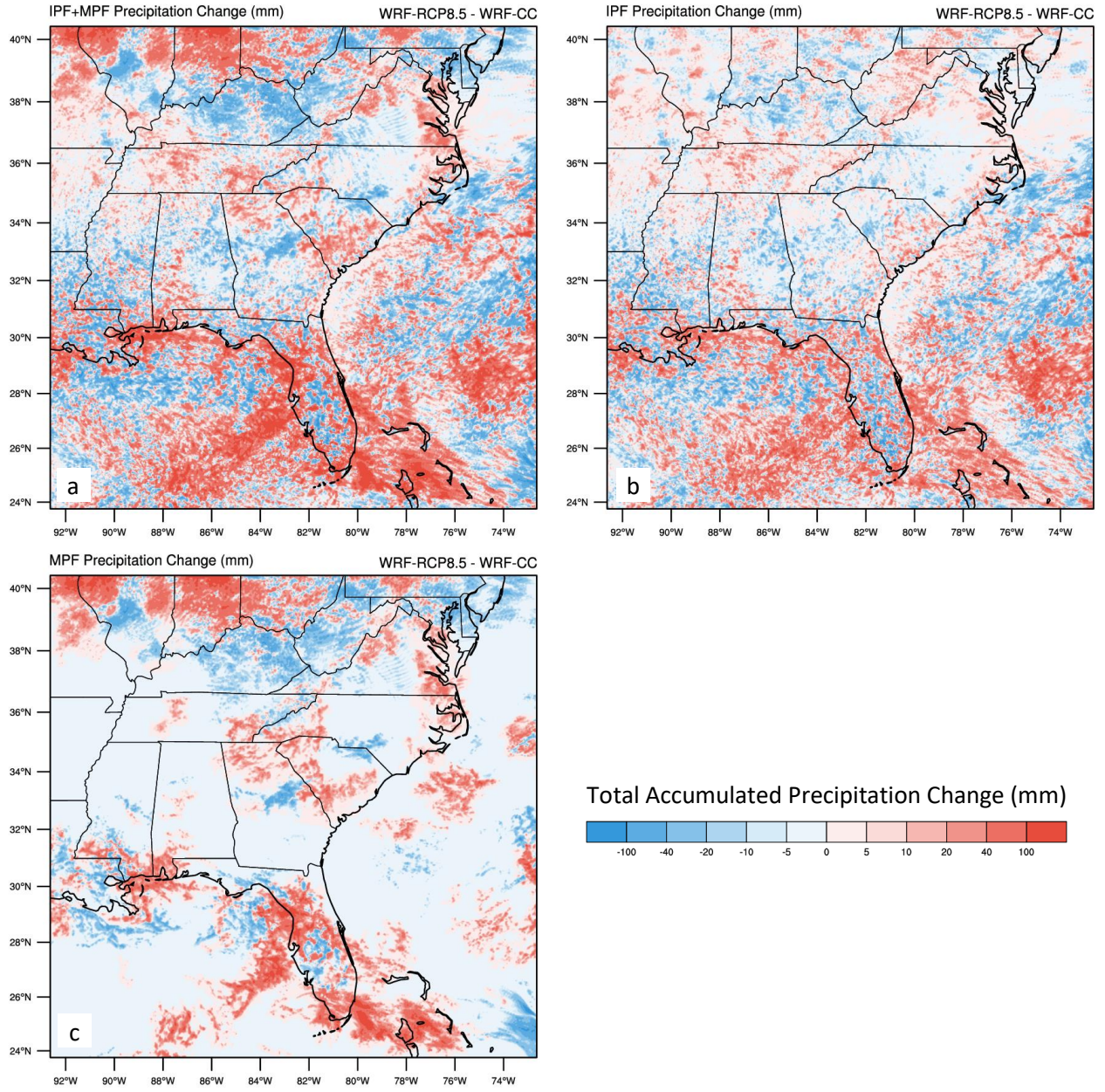


Figure 19 Same as Figure 17, but for WRF-RCP8.5 and WRF-CC.

4.2.3 IPF/MPF Precipitation Fractions

Model Evaluation. In NMQ, IPF and MPF contributed a similar fraction of total precipitation (Figure 20). Over land, MPF contributed more to the total observed precipitation than IPF, while the opposite is true for the ocean buffer (Figure 20). However, WRF-CC was strongly biased toward IPF with much larger fractions of total precipitation contributed by IPF over both the land and ocean buffer (Figure 20).

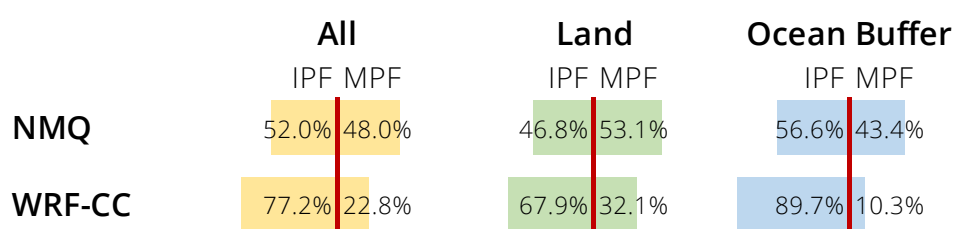


Figure 20 Fractions of total precipitation produced by IPF and MPF over the entire domain, the land, and the ocean buffer for NMQ and WRF-CC, measured over 0:00 UTC 17 June to 0:00 UTC 23 June 2010.

Future Climates. In WRF-RCP4.5, the fraction of total precipitation produced by IPF increased by 3.6%, with the largest increase over the ocean (Figure 21). In WRF-RCP8.5, the IPF precipitation fraction decreased by 3.0%, favoring the development of heavier rain-producing MPF (Figure 21). In WRF-RCP8.5, the MPF precipitation fraction increased everywhere, including a 5.5% increase over the ocean (Figure 21).

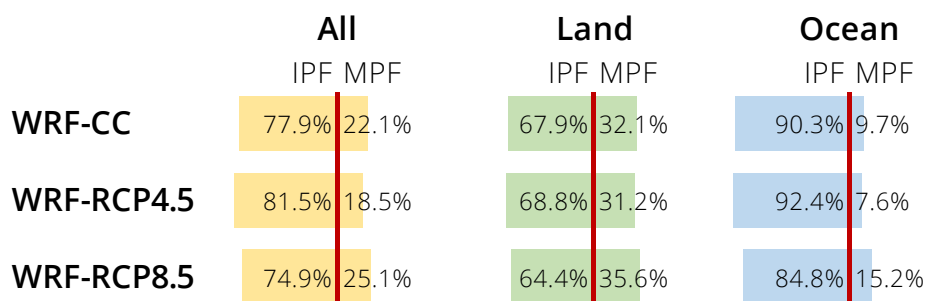


Figure 21 Same as Figure 20, but for WRF-CC and the future climate simulations.

4.2.4 Diurnal Cycle of Precipitation

Model Evaluation. Figure 22b shows a comparable diurnal cycle of precipitation over the land and ocean buffer in WRF-CC and NMQ. Like in the observations, the diurnal cycle of precipitation in WRF-CC displayed a maximum over the ocean at early morning and then a maximum over the land during the late evening hours. WRF-CC did not resolve the nighttime-early morning precipitation over the Gulf Stream (Figure 25). The diurnal cycle of oceanic precipitation in WRF-CC is produced mainly by IPF, whereas the diurnal cycle over land seems to be produced by a combination of IPF and MPF (Figure 22d,e).

Future Climates. In WRF-RCP8.5, total precipitation increased throughout all hours of the day, with the greatest increases between 7-18 UTC and 21-23 UTC (Figure 23a). The diurnal cycle of precipitation over land and ocean were enhanced in WRF-RCP8.5 with precipitation over the land increasing during the afternoon-to-early evening when precipitation over land is strongest and precipitation over the ocean increasing during the nighttime to early morning hours when rain is strongest over the ocean (Figure 23a). The diurnal cycle of precipitation is contributed to mainly by IPF precipitation. Figures 26 and 27 show diurnal precipitation maps of WRF-RCP4.5 and WRF-RCP8.5. WRF-RCP4.5 and WRF-RCP8.5 varied greatly from WRF-CC during the early morning over ocean (Figure 23d). This appears to be a thermodynamic response to the increase in CAPE over the land and ocean in the future climate simulations (Figure 10), combined with a large increase in CIN over land and slight increase over the ocean (Figure 11). This allows oceanic precipitation to grow more easily in the future climate simulations, contributing to higher numbers of IPF.

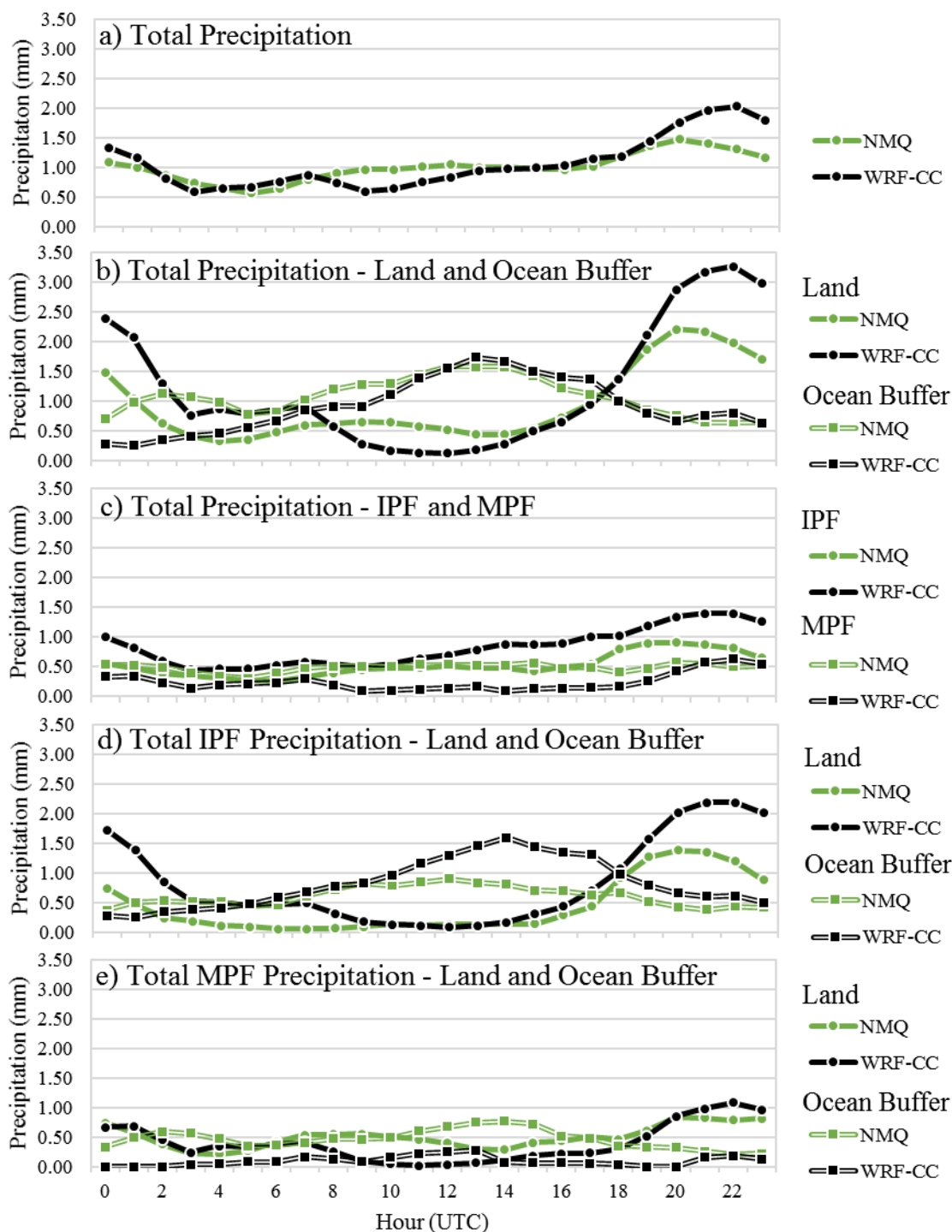


Figure 22 Average total hourly accumulated precipitation (mm) in WRF-CC and NMQ measured over 0:00 UTC 17 June to 0:00 UTC 23 June 2010 for (a) the entire region, (b) the individual land (solid) and ocean buffer (hollow), (c) the entire region divided into IPF (solid) and MPF (hollow) precipitation, (d) IPF precipitation over the land (solid) and ocean region (hollow), and (e) MPF precipitation over the land (solid) and ocean buffer (hollow).

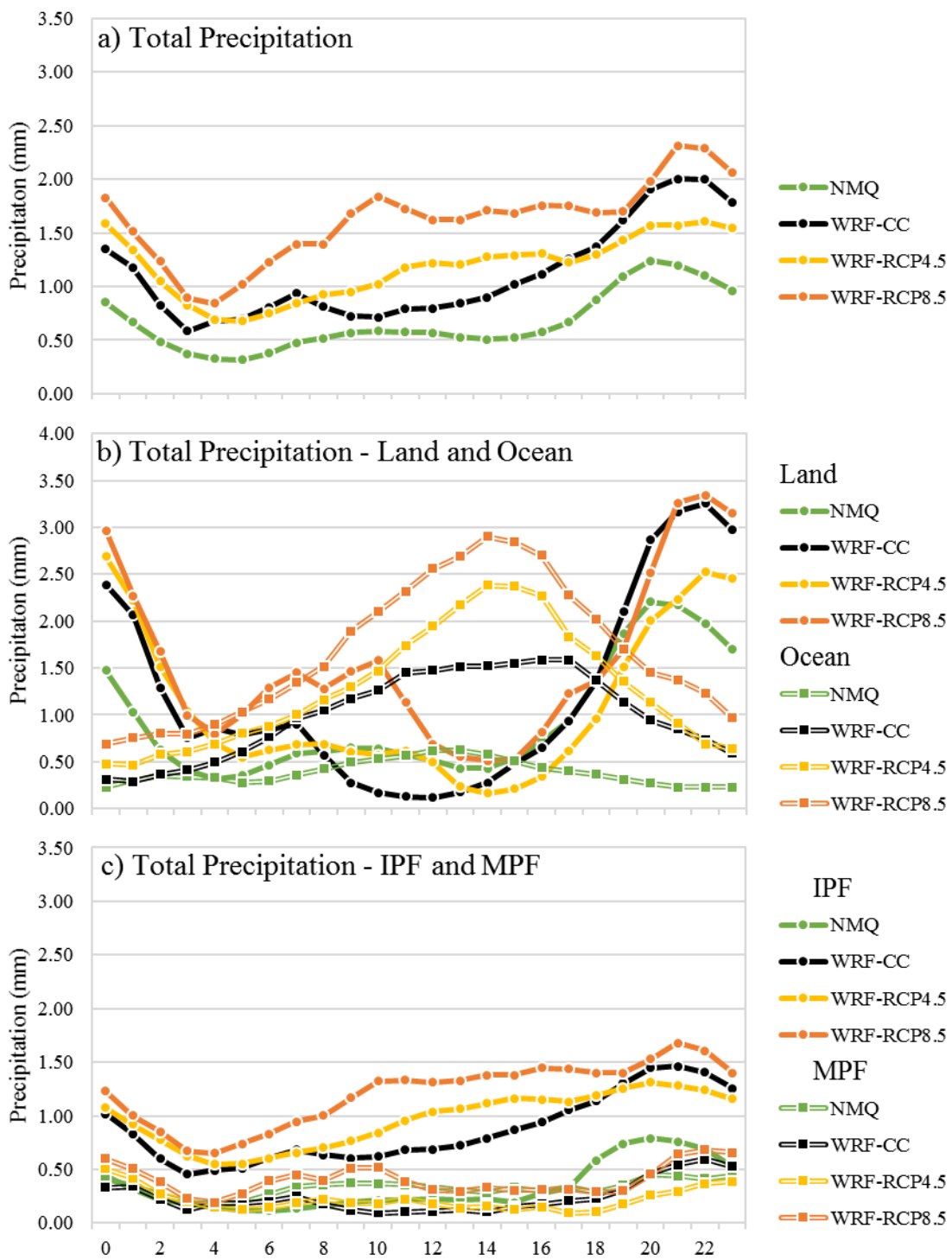


Figure 23 Same as Figure 22, but for the future climate simulations.

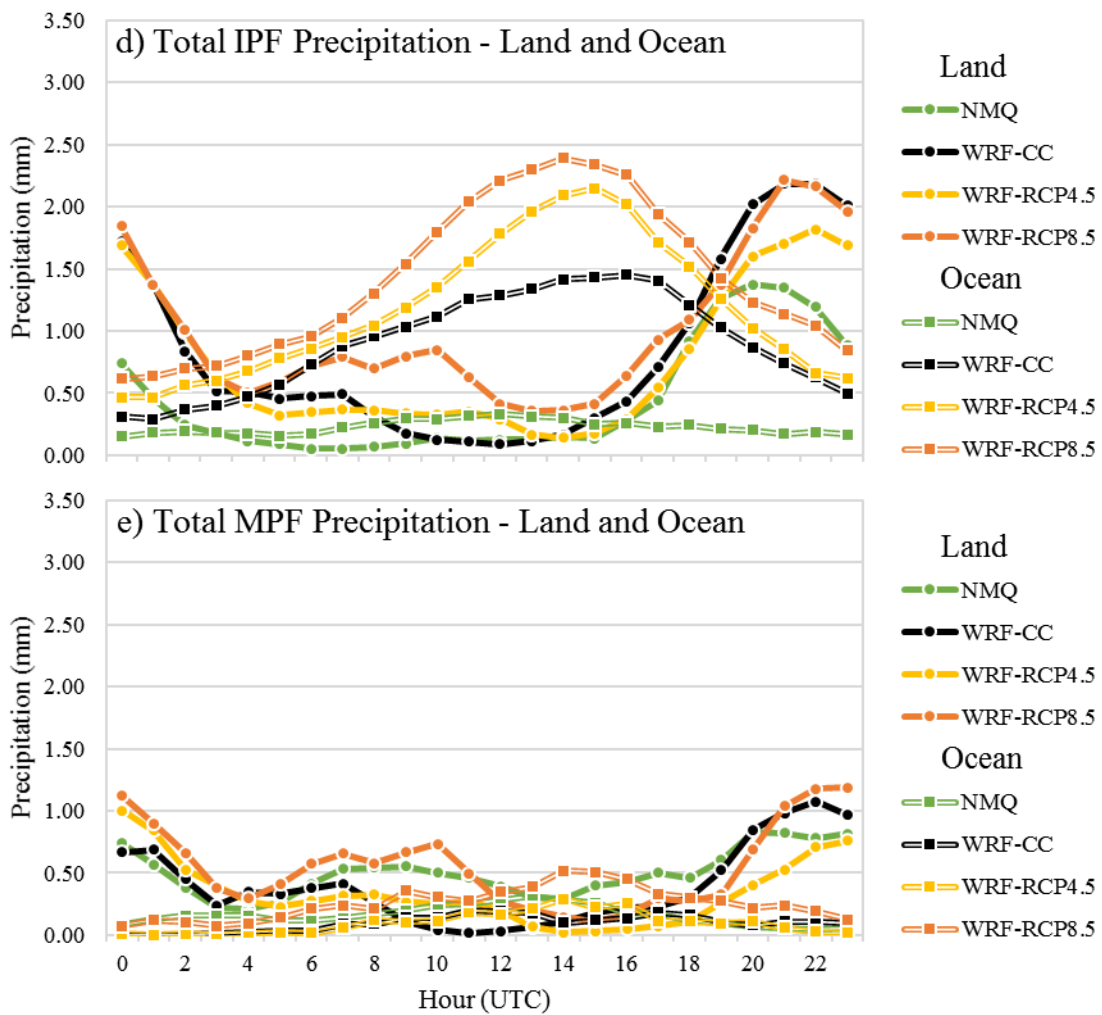


Figure 23 continued.

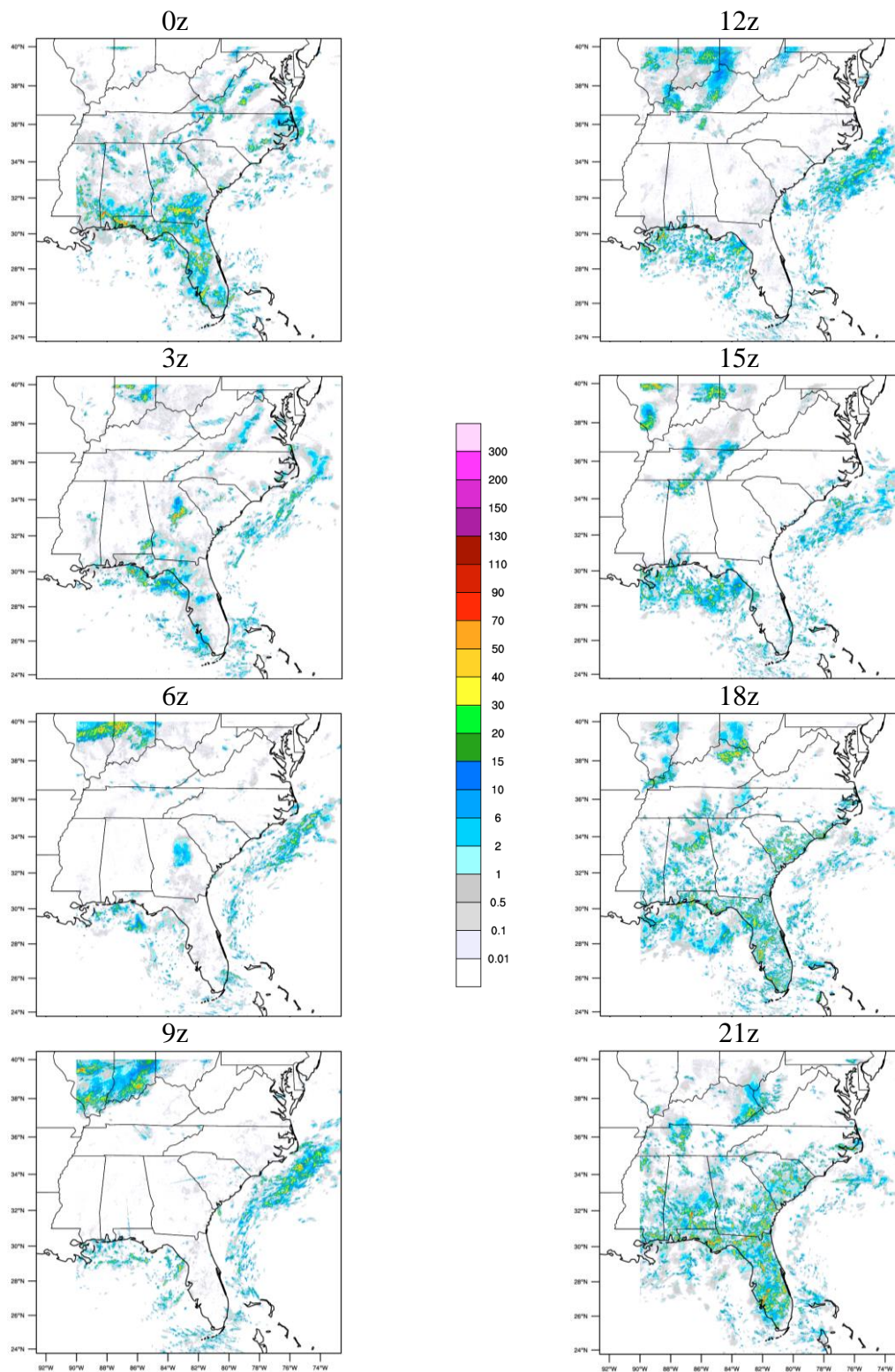


Figure 24 The diurnal sequence of hourly total accumulated IPF and MPF precipitation (mm) observed from 0 UTC 17 June to 0 UTC 23 June in the NMQ dataset.

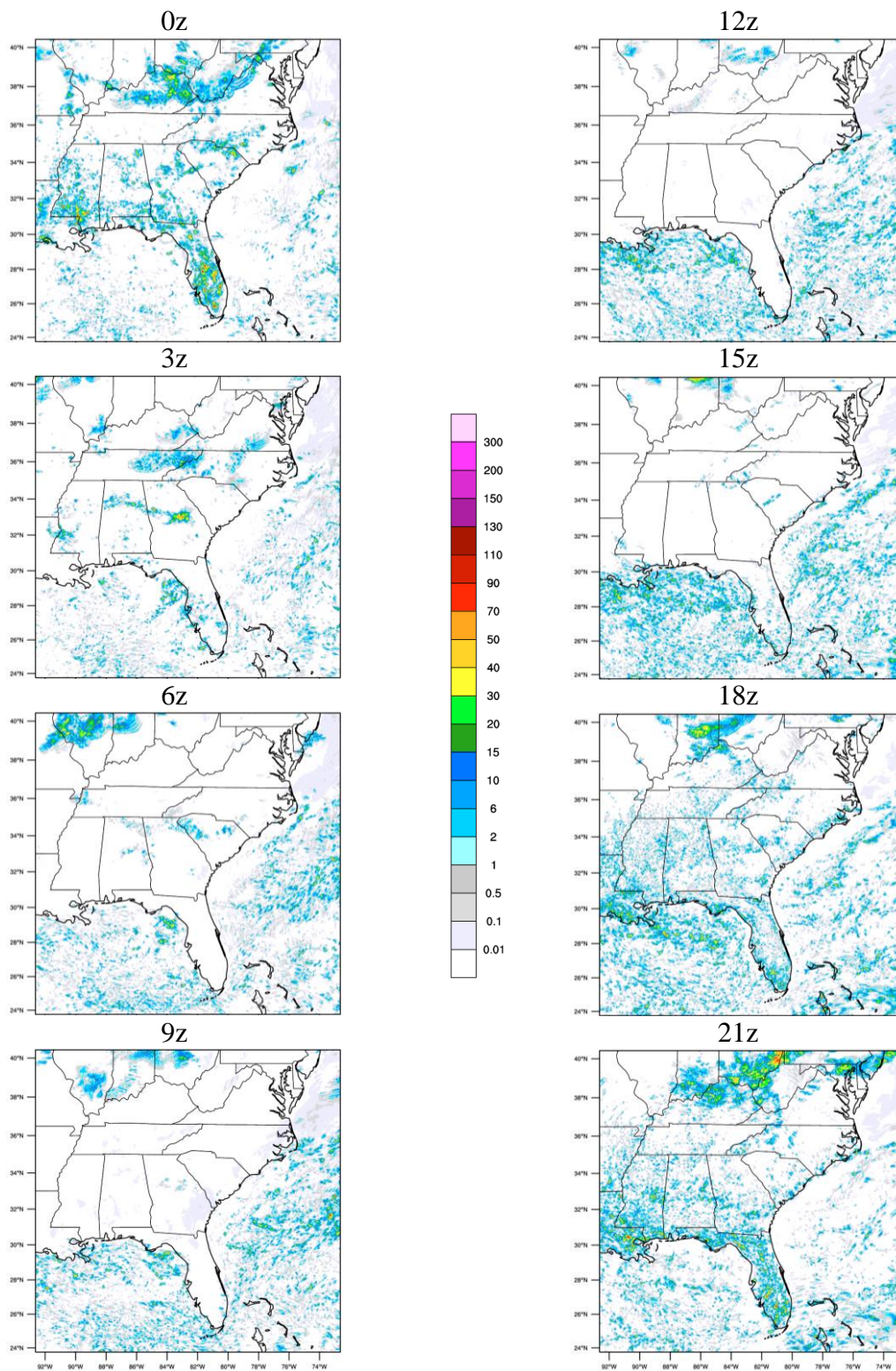


Figure 25 Same as Figure 24, but for WRF-CC.

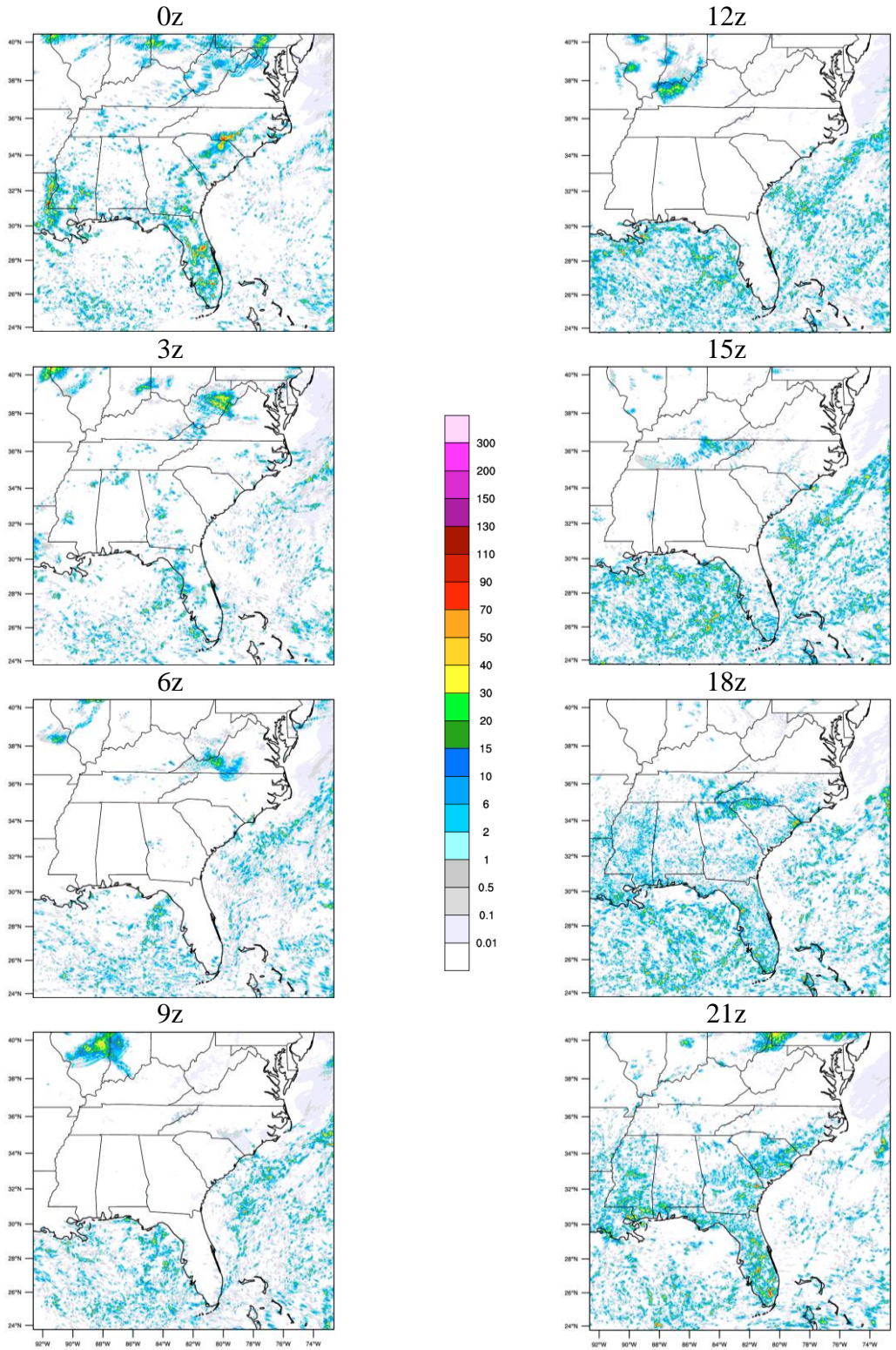


Figure 26 Same as Figure 24, but for WRF-RCP4.5.

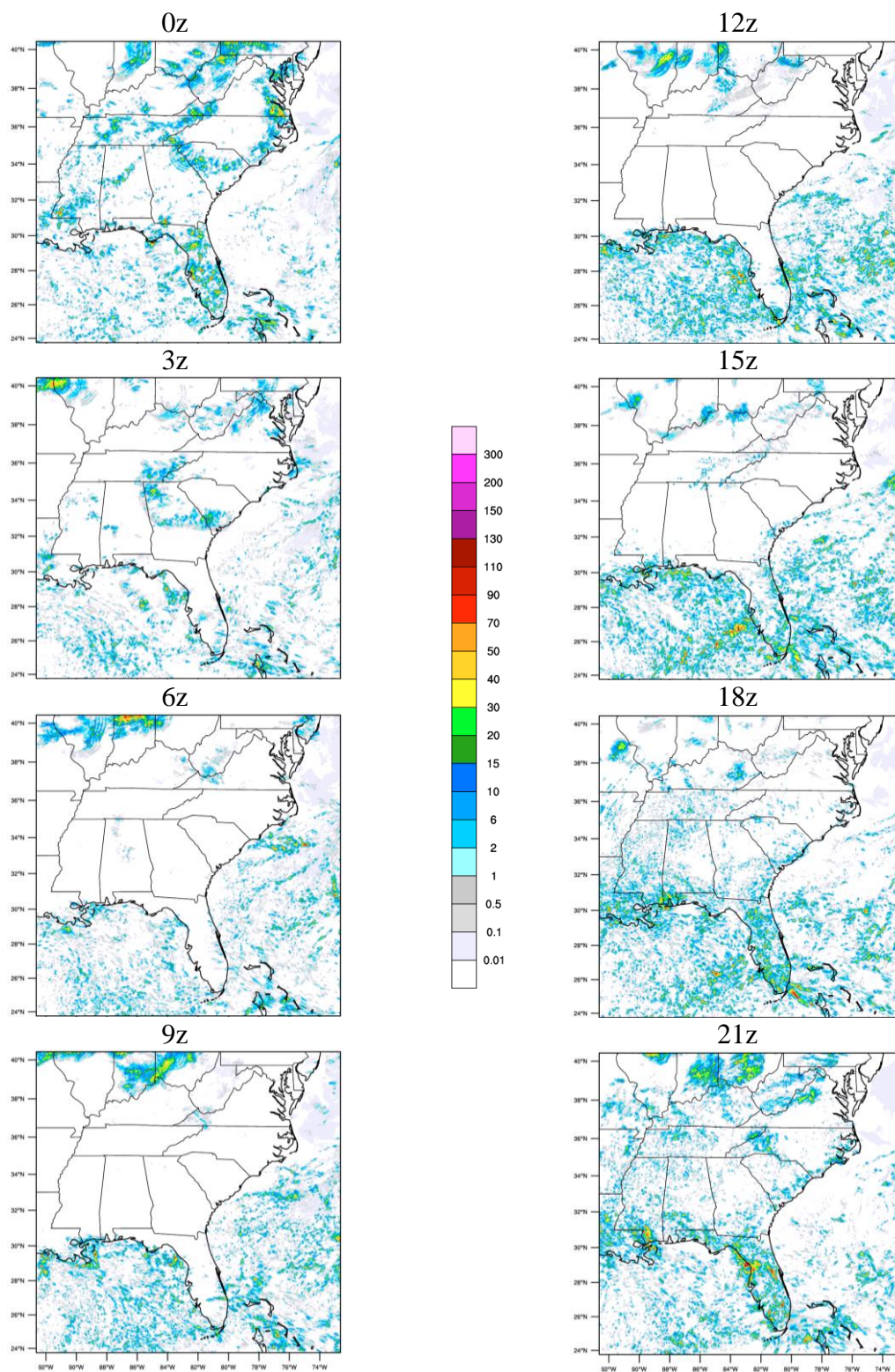


Figure 27 Same as Figure 24, but for WRF-RCP8.5.

4.3 Precipitation Features

The Rickenbach et al. (2015) identification algorithm produced additional output on total feature counts, feature lengths, feature echo heights, and feature total precipitation for the present and future climate simulations. Once again, the 250 km offshore ocean buffer was used to compare oceanic precipitation in WRF and NMQ.

4.3.1 Feature Numbers

Model Evaluation. Total IPF and MPF feature counts in WRF-CC compared well and were within 3.2% of the observed totals in the NMQ dataset (Table 7). Total counts of IPF were within 2.6% of each other, while WRF-CC had 61.5% fewer MPF than NMQ (Table 7). Over land, total feature counts and IPF feature counts compared well in WRF-CC and NMQ, but once again WRF-CC produced 63.5% fewer MPF features than in NMQ. Over the ocean buffer, total feature counts and IPF feature counts were within 10% of each other, but MPF feature counts in WRF-CC were 797 less, or 731.2% less, than NMQ (Table 7).

Dataset	Totals			Land			Ocean Buffer		
	All	IPF	MPF	All	IPF	MPF	All	IPF	MPF
NMQ	212453	210484	1969	115187	114124	1063	97266	96360	906
WRF-CC	205829	205070	759	116882	116232	650	88947	88838	109

Table 7 Total number of precipitation features in WRF-CC and NMQ measured from 0:00 UTC 17 June to 0:00 UTC 23 June 2010 over the land and ocean buffer.

Future Climates. Total precipitation feature numbers in WRF-RCP4.5 and WRF-RCP8.5 changed very little from WRF-CC. In WRF-RCP8.5, the number of MPF increased both over the land and the ocean (Table 8).

Dataset	Totals			Land			Ocean		
	All	IPF	MPF	All	IPF	MPF	All	IPF	MPF
WRF-CC	430253	429293	960	116882	116232	650	313371	313061	310
WRF-RCP4.5	431336	430408	928	105962	105390	572	325374	325018	356
WRF-RCP8.5	415903	414480	1423	109051	108221	830	306852	306259	593

Table 8 Total number of precipitation features in WRF-CC, WRF-RCP4.5, and WRF-RCP8.5 measured from 0:00 UTC 17 June to 0:00 UTC 23 June 2010 over the land and ocean.

4.3.2 Feature Lengths

Model Evaluation. IPF feature lengths over land in WRF-CC compared well to NMQ (Figure 28a). WRF-CC produced more features 0-20 km in length, but produced fewer features 20-100 km in length compared to the NMQ (Figure 28a). There was greater disparity between WRF-CC and NMQ over the ocean buffer for features 10-100 km in length (Figure 28b). One explanation is that the convective parameterization chosen for WRF favors more IPF features. It might also be an artifact of the inner grid spacing.

MPF feature lengths over land in WRF-CC also compared well to NMQ (Figure 29a). Over the ocean buffer, the discrepancies between MPF lengths in WRF-CC and NMQ were more significant (Figure 29b). WRF-CC resolved considerably fewer features 100-260 km in length, and did not produce any MPF over 260 km in length, while NMQ contained over 50 features greater than 300 km in length (Figure 29b).

Future Climates. IPF lengths over land did not change considerably in the future climate simulations (Figure 30a). Oceanic IPF in the larger bin sizes increased, with greater numbers in WRF-RCP8.5 (Figure 30b). MPF lengths over land changed very little in WRF-RCP4.5, but there was an increase in features between 180-300 km in length (Figure 31a). MPF lengths increased in almost every bin size in WRF-RCP8.5 (Figure 31a). Oceanic MPF 100-160 km in length increased in WRF-RCP4.5 (Figure 31b). Interestingly, WRF-RCP4.5 contained fewer

MPF 180-260 km in length compared to WRF-CC (Figure 31b). WRF-RCP8.5 saw an increase in MPF length throughout almost all bin sizes, including a few features 260-300 km in length which were not present in WRF-CC (Figure 31b). This suggests that there may exist some threshold temperature (above the WRF-RCP4.5 temperature increase) that leads to a merging of IPF and thus an increase in MPF.

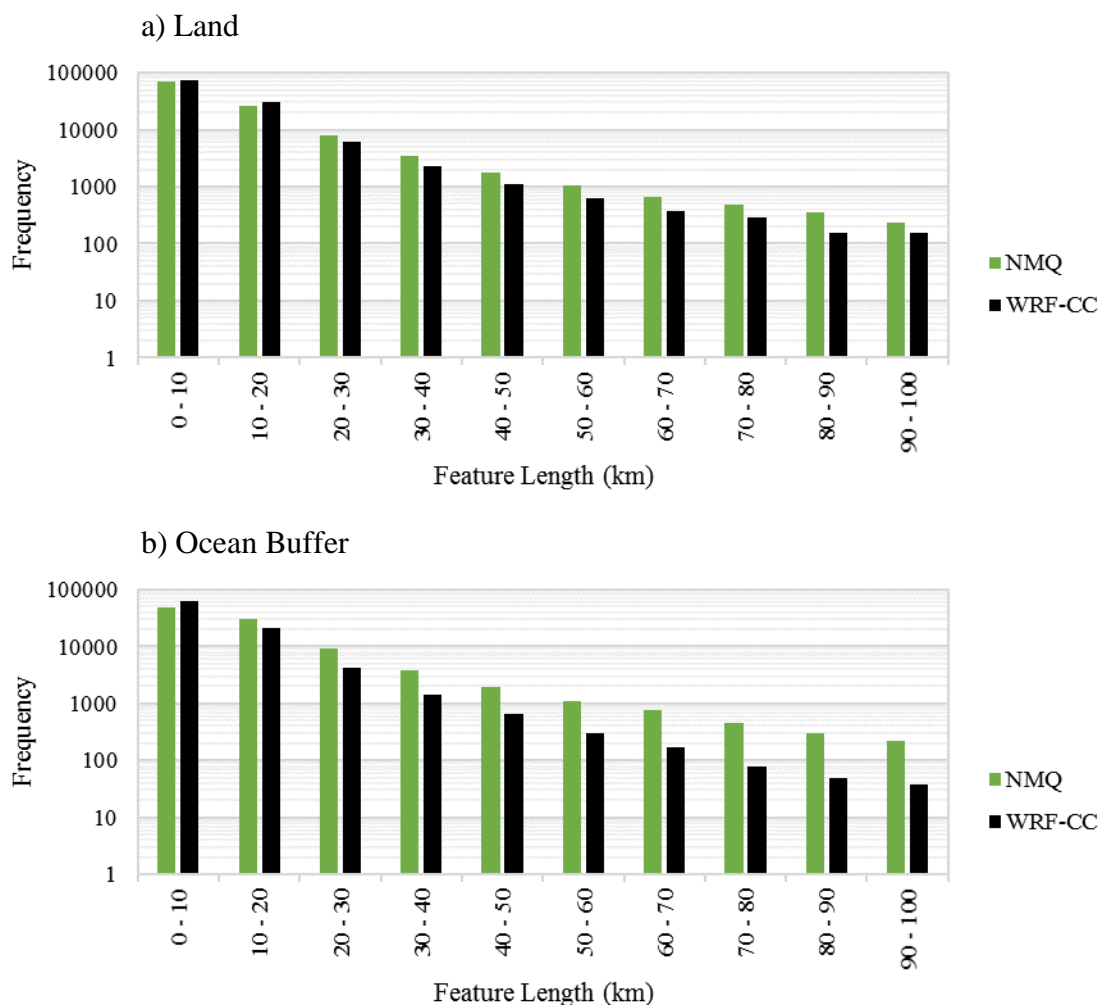


Figure 28 Histograms of IPF feature lengths (km) in WRF-CC and NMQ over (a) the land and (b) the ocean buffer.

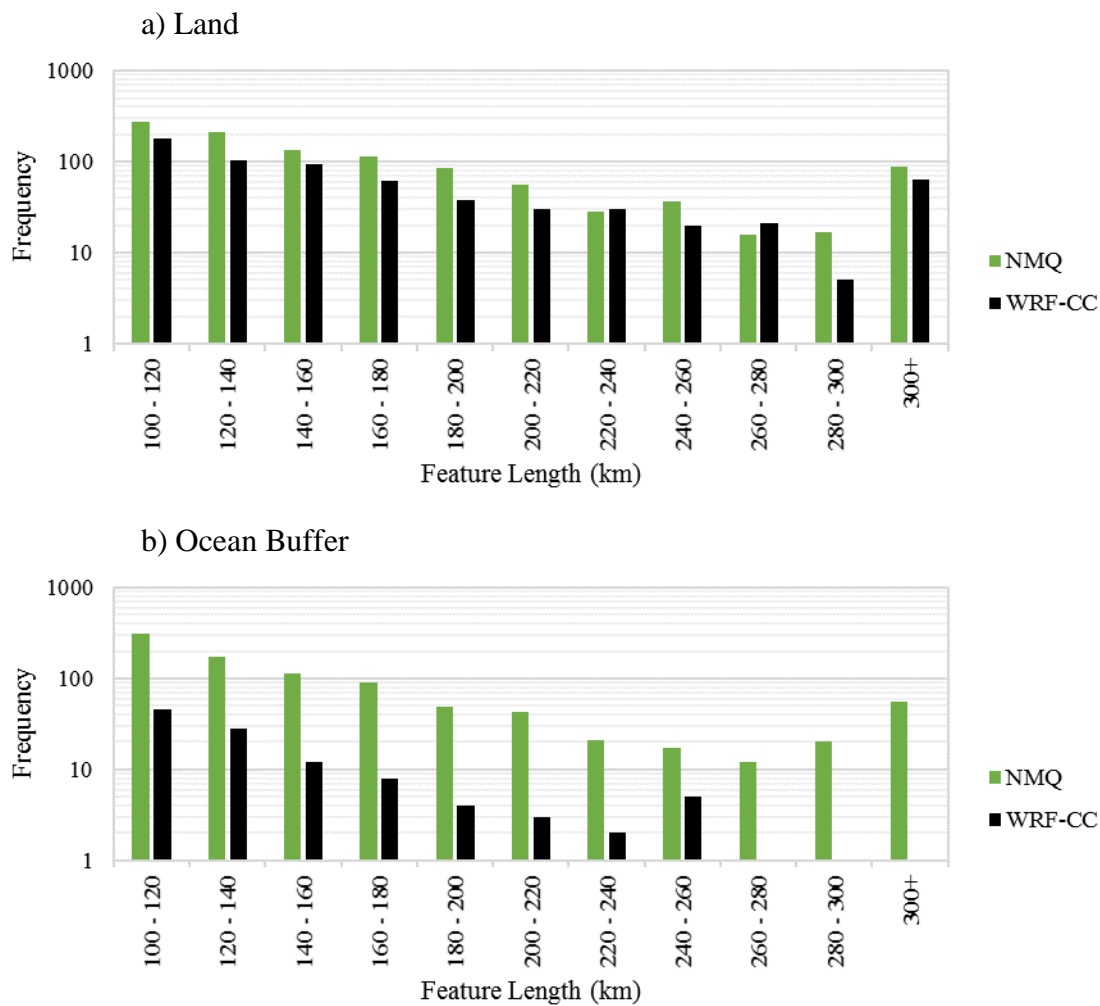


Figure 29 Same as Figure 28, but for MPF.

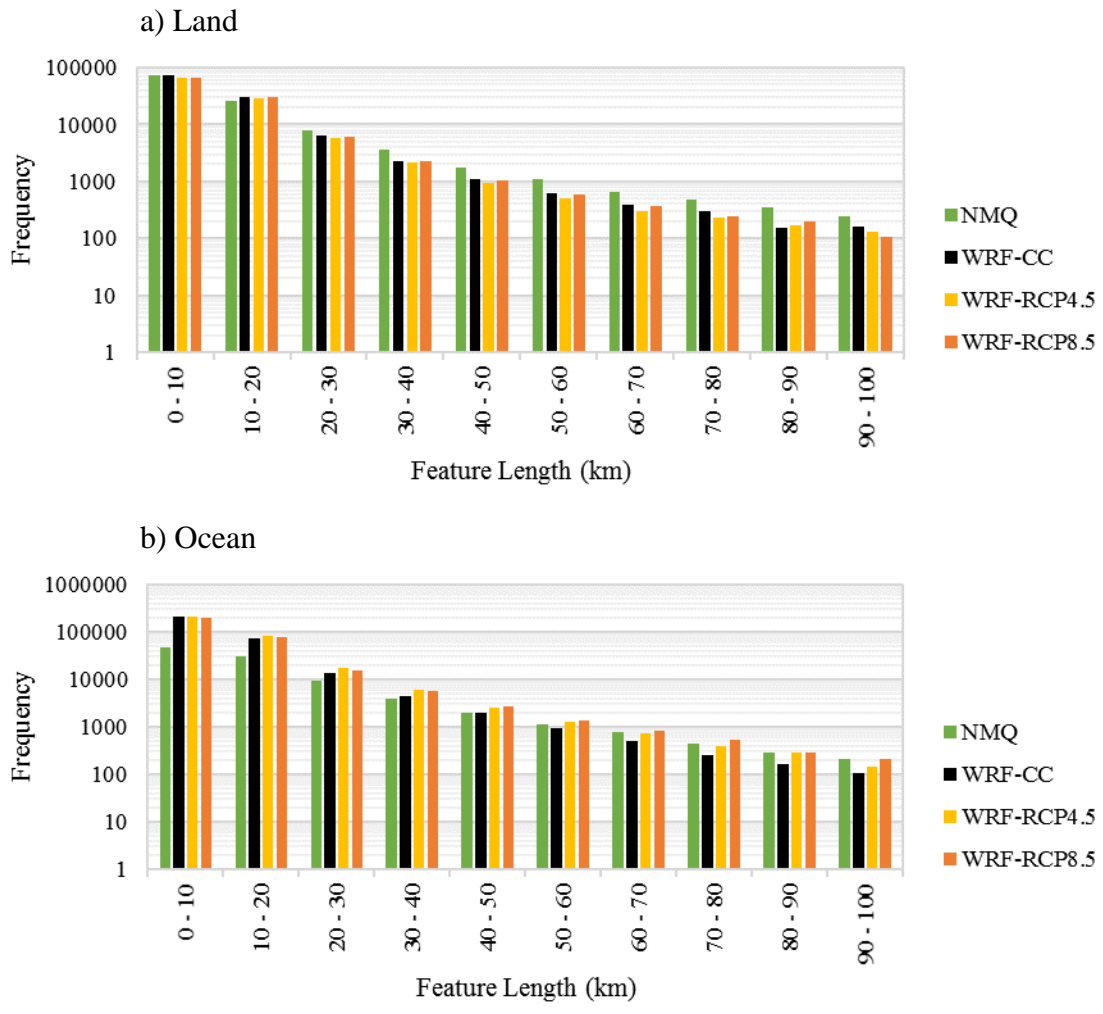


Figure 30 Histograms of IPF feature lengths (km) in NMQ, WRF-CC, WRF-RCP4.5, and WRF-RCP8.5 over (a) the land and (b) the ocean.

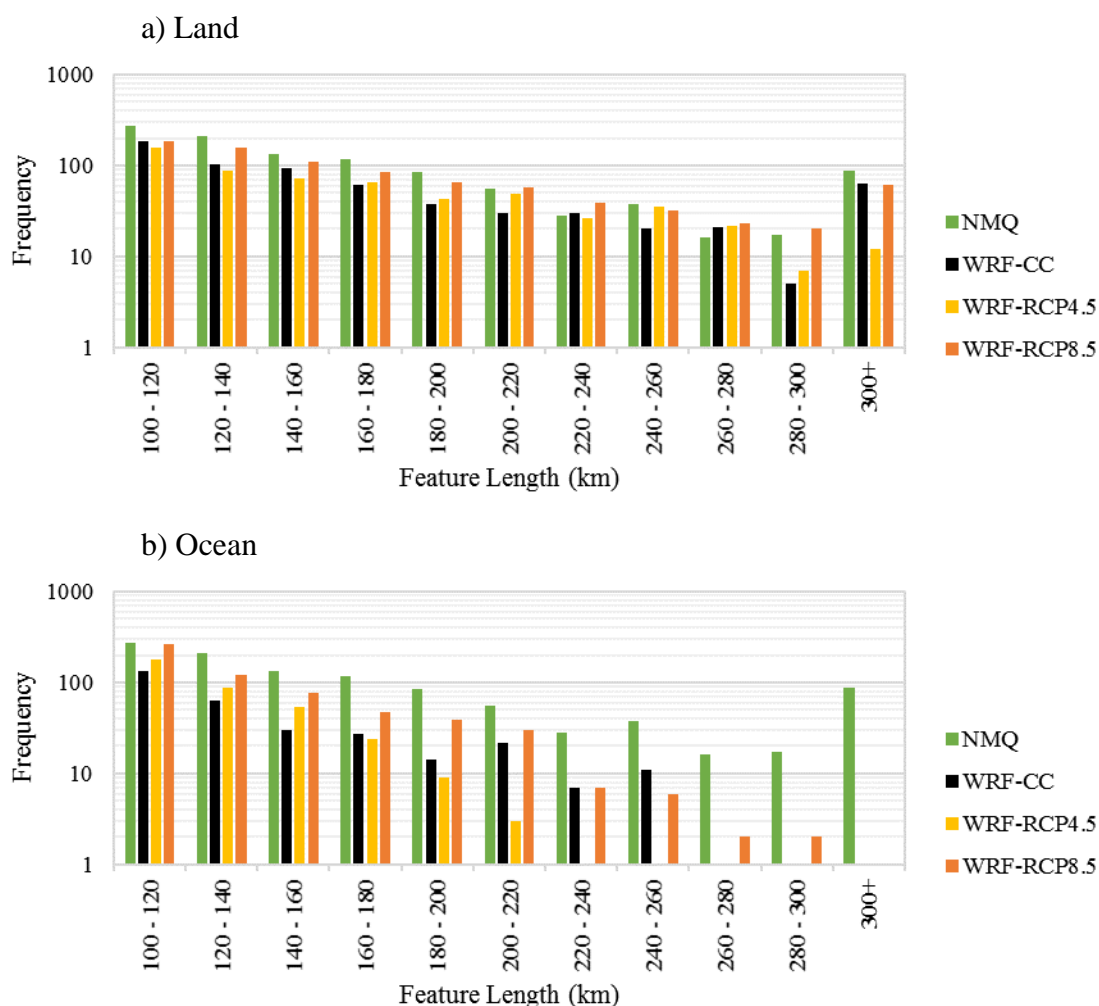


Figure 31 Same as Figure 30, but for MPF.

4.3.3 Feature Echo Heights

Model Evaluation. IPF feature heights in WRF-CC compared poorly to NMQ (Figure 32). This is true for both land (Figure 32a) and ocean buffer IPF (Figure 32b). WRF-CC produced considerably more IPF 0-7 km in height compared to NMQ, but produced fewer features 7-18 km in height (Figure 32a,b). WRF-CC IPF echo heights were shallower than NMQ. Again, this may be a response of the chosen parameterization scheme in WRF.

In contrast, MPF echo heights (Figure 33) in WRF-CC compared better to NMQ than IPF (Figure 32). Over the land, WRF-CC captured the bimodal distribution of MPF echo heights with

similar amplitudes to NMQ (Figure 33a). Over the ocean buffer, WRF-CC produced a similar distribution of MPF echo heights, but with smaller amplitudes (Figure 33b).

Future Climates. In WRF-RCP4.5, IPF echo heights over land decreased below 13 km, but increased above 13 km, with the greatest changes in the larger bin sizes (Figure 34a). These changes were more established in WRF-RCP8.5 for bin sizes greater than 12-13 km. In fact, WRF-RCP8.5 contained several IPF with echo heights greater than 18 km, which was not present in the other simulations (Figure 34a). Over the ocean, IPF echo heights increased in a similar manner beyond 6 km, with the greatest changes occurring again at the larger bin sizes (Figure 34b). The increase in the deeper echo heights in WRF-RCP4.5 and WRF-RCP8.5 is consistent with the increase in CAPE in the future climate simulations.

MPF echo heights over land increased between 3-10 km, while WRF-CC and NMQ had few features at these bin sizes (Figure 35a). MPF between 11-15 km decreased, but there was an increase in MPF above 16 km, especially in WRF-RCP8.5 (Figure 35a). Over the ocean, MPF below 15 km decreased, while features greater than 15 km increased (Figure 35b).

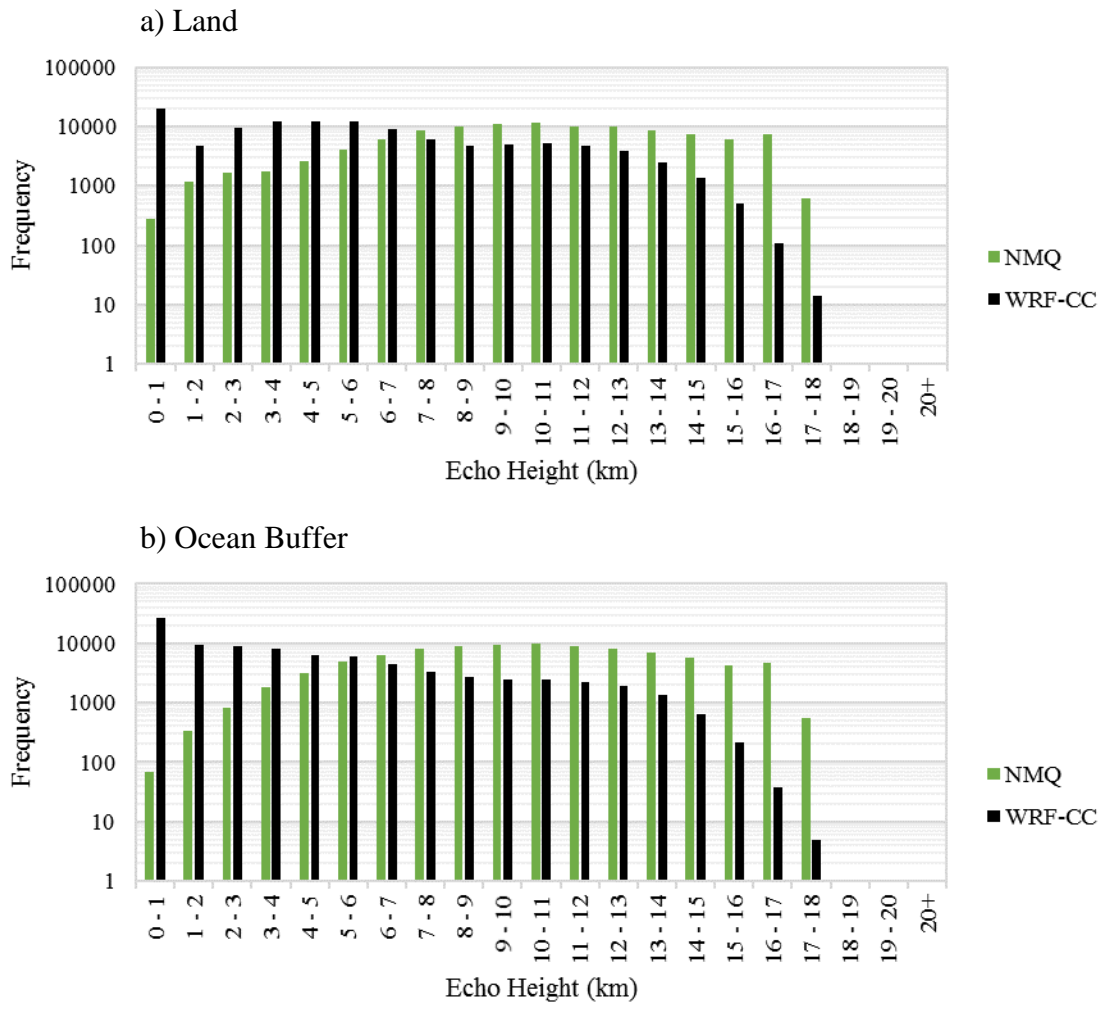


Figure 32 Histograms of IPF echo heights (km) in WRF-CC and NMQ over (a) the land and (b) the ocean buffer.

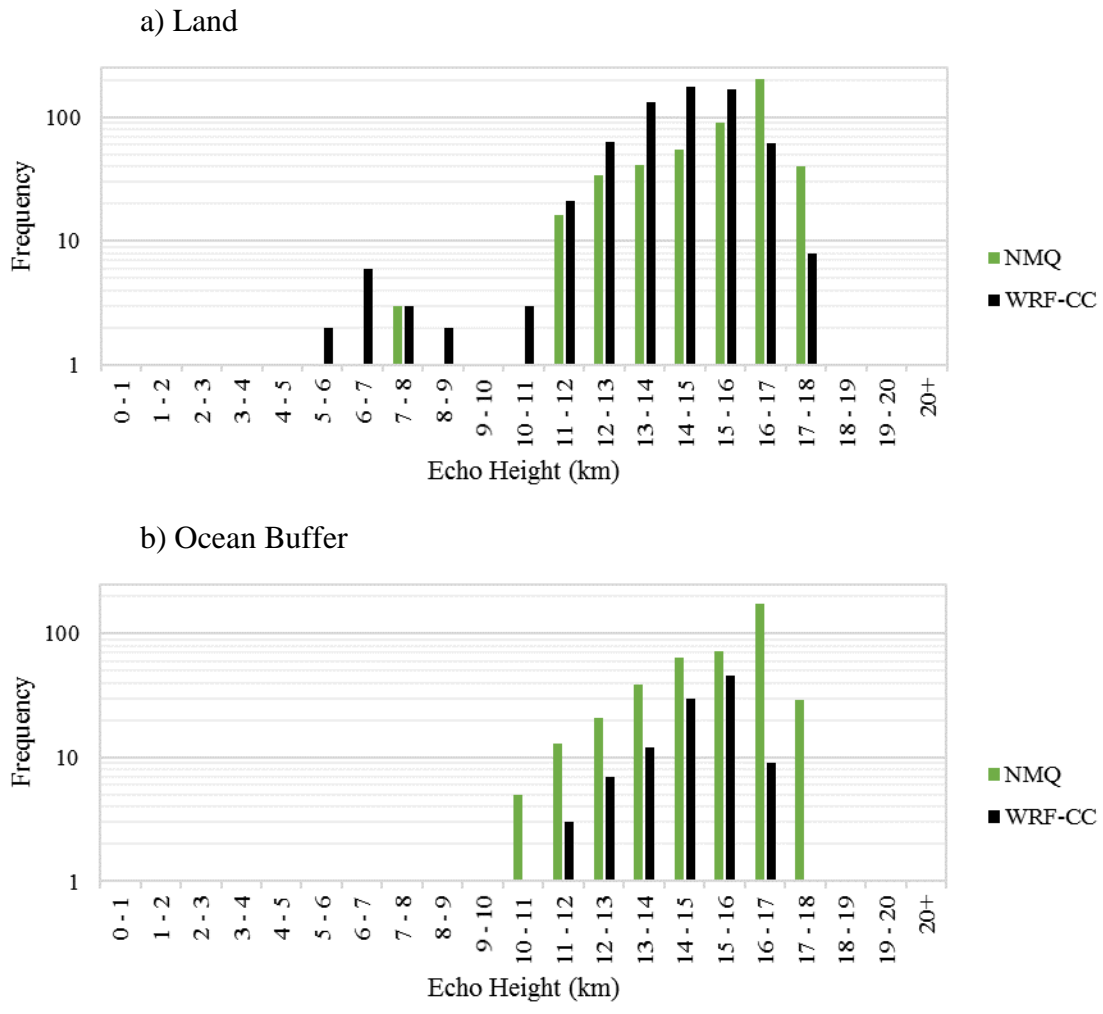


Figure 33 Same as Figure 32, but for MPF.

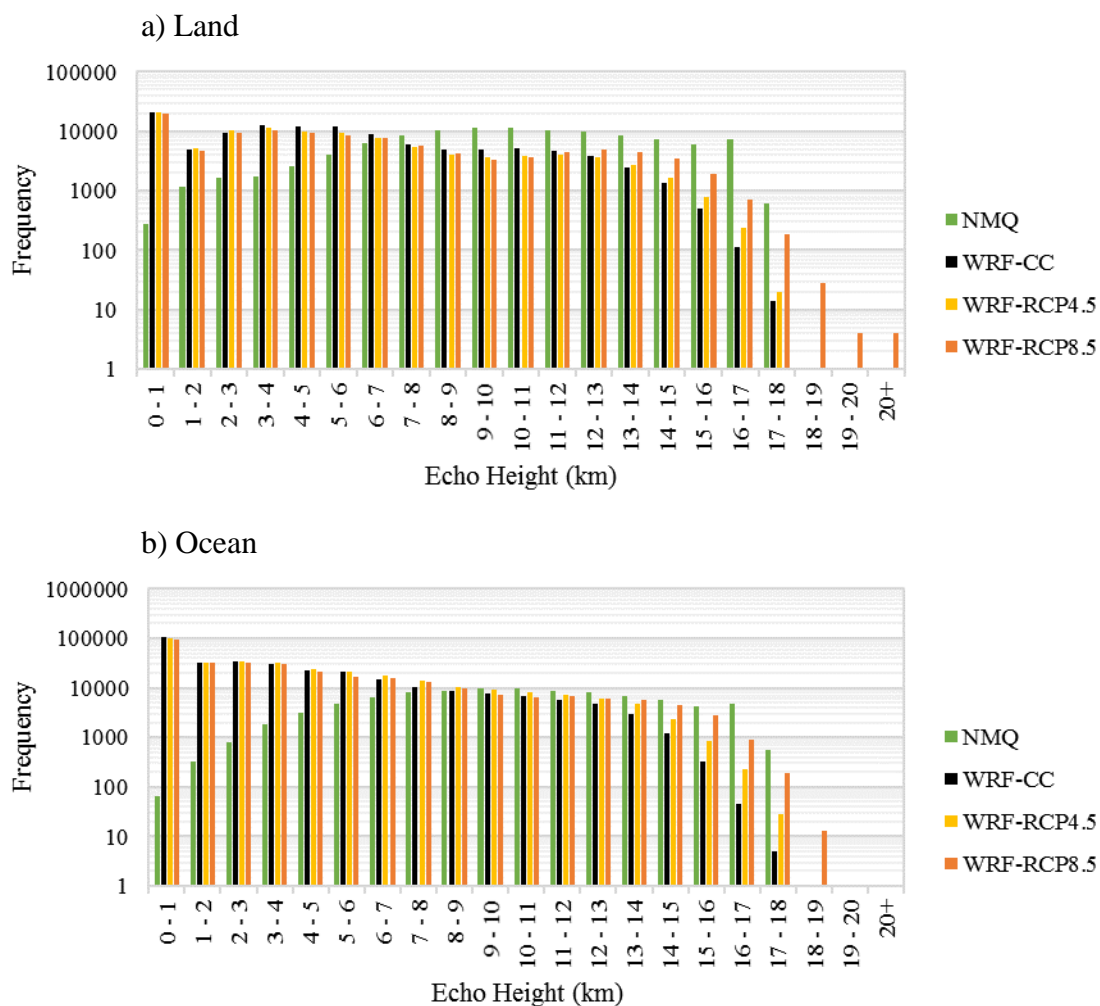


Figure 34 Histograms of IPF echo heights (km) in NMQ, WRF-CC, WRF-RCP4.5, and WRF-RCP8.5 over (a) the land and (b) the ocean.

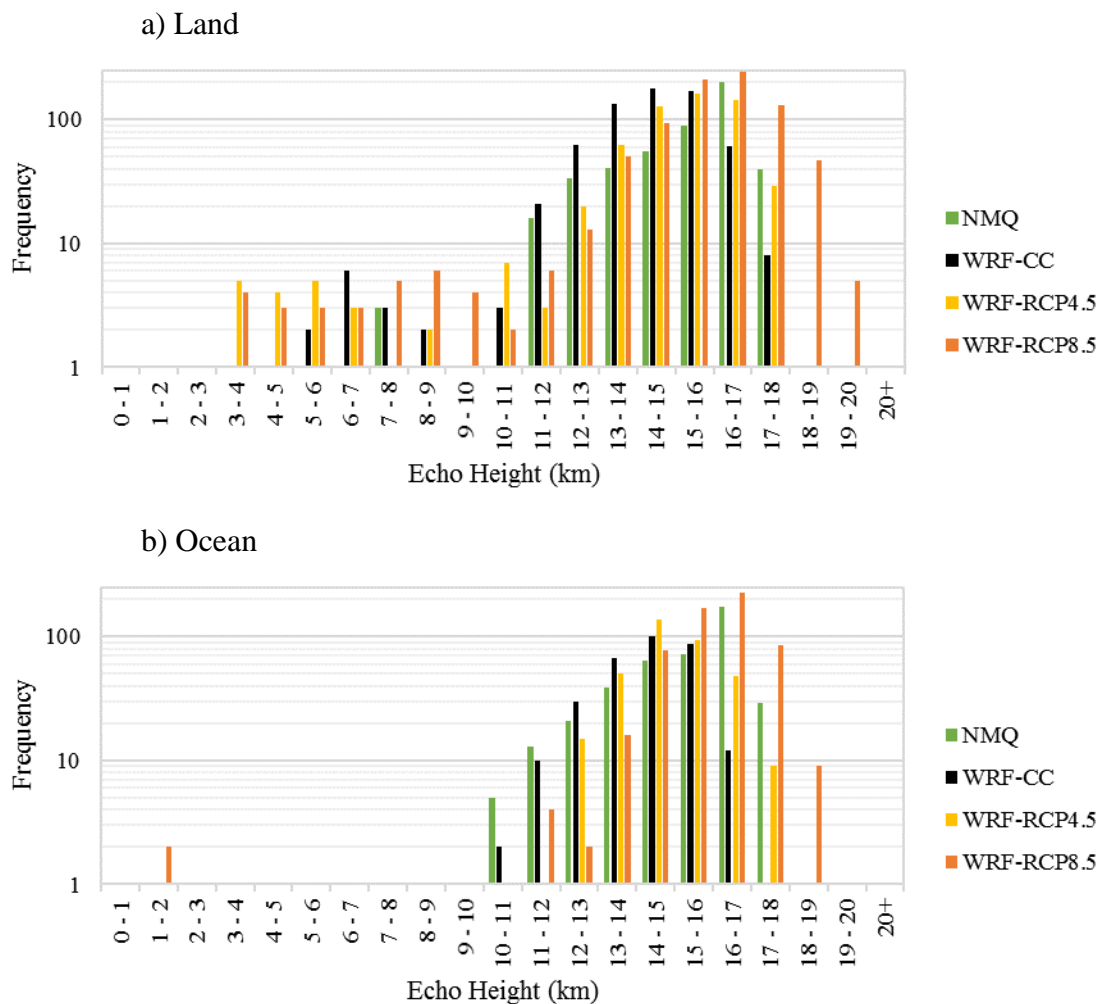


Figure 35 Same as Figure 34, but for MPF.

4.3.4 Feature Total Precipitation

Model Evaluation. When compared to NMQ, WRF-CC contained more IPF features with total precipitation less than 100 mm over the land (Figure 36a) and the ocean buffer (Figure 36b). However, NMQ contained more IPF with total precipitation greater than 100 mm compared to WRF-CC (Figure 36a,b).

The total number of MPF with total precipitation between 0-100,000 mm over land was greater in WRF-CC than in NMQ (Figure 37a). However, NMQ contained more MPF with total

precipitation greater than 120,000 mm (Figure 37a). Over the ocean buffer, WRF-CC produced MPF with total precipitation 0-120,000 mm, but in fewer numbers compared to NMQ (Figure 37b). WRF-CC failed to produce any MPF with total precipitation greater than 120,000 mm (Figure 37b), which could be due to the weaker MPFs over the Gulf Stream, Gulf Coast and Midwest (Figure 17c).

Future Climates. Total IPF precipitation over land changed very little in the future climate simulations (Figure 38a). Over the ocean, there is a trend for IPF to produce more precipitation, especially at the larger bin sizes (Figure 38b). However, as seen in Figures 14-16, it is odd that although WRF-RCP4.5 produced more IPF precipitation over the Gulf Stream compared to WRF-CC as expected, WRF-RCP8.5 produced very little IPF over the Gulf Stream, even less than WRF-CC. Total MPF precipitation over land generally increased in the future climate simulations, with larger changes in WRF-RCP8.5 (Figure 39a). Total MPF precipitation over the ocean increased substantially in the future climate simulations (Figure 39b). In WRF-RCP8.5, considerably more features with total precipitation over 100,000 mm are found (Figure 39b). Still, WRF-RCP4.5 and WRF-RCP8.5 failed to produce MPF precipitation in the Gulf Stream, which is counter to expectations and is the most unusual aspect of the future climate simulations.

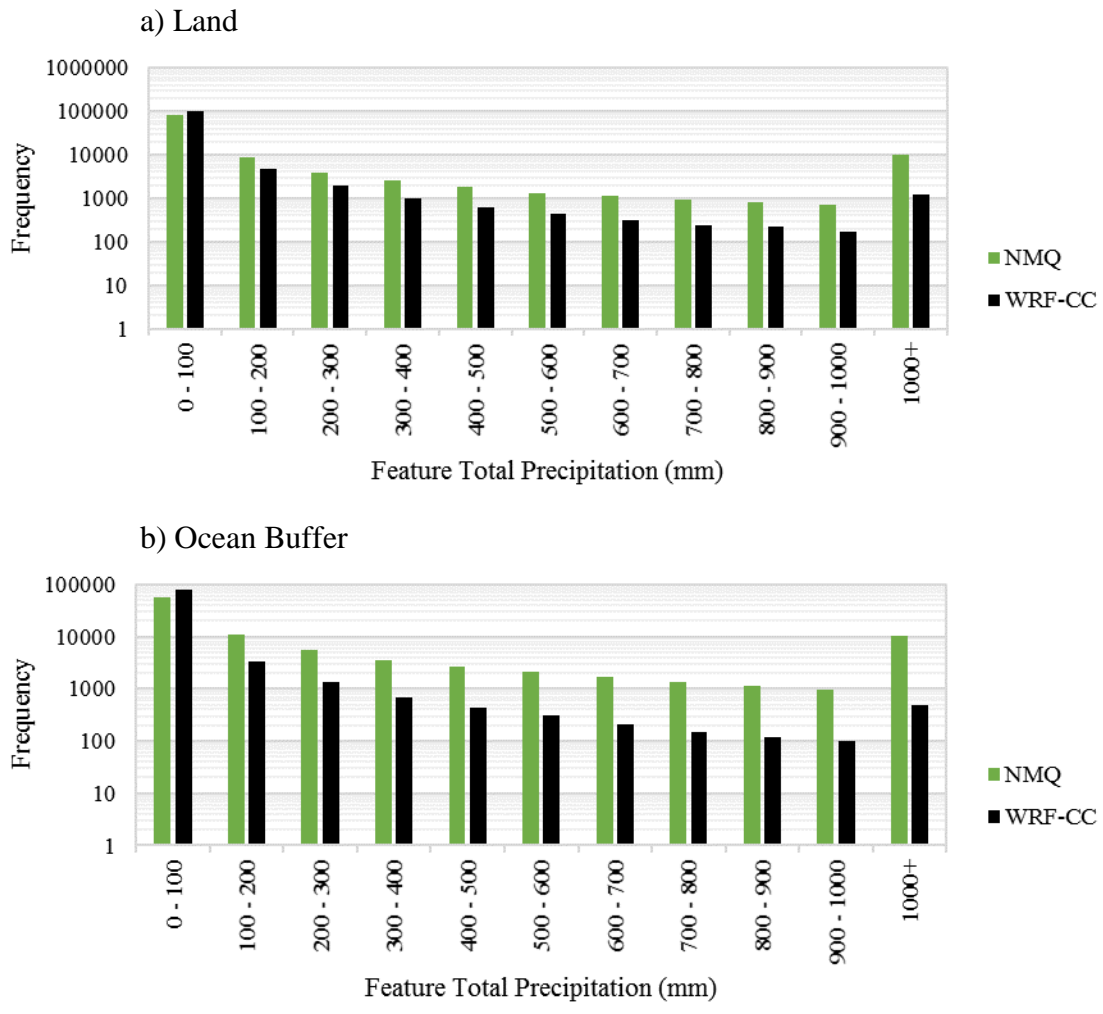


Figure 36 Histograms of IPF feature total precipitation (mm) in WRF-CC and NMQ over (a) the land and (b) the ocean buffer.

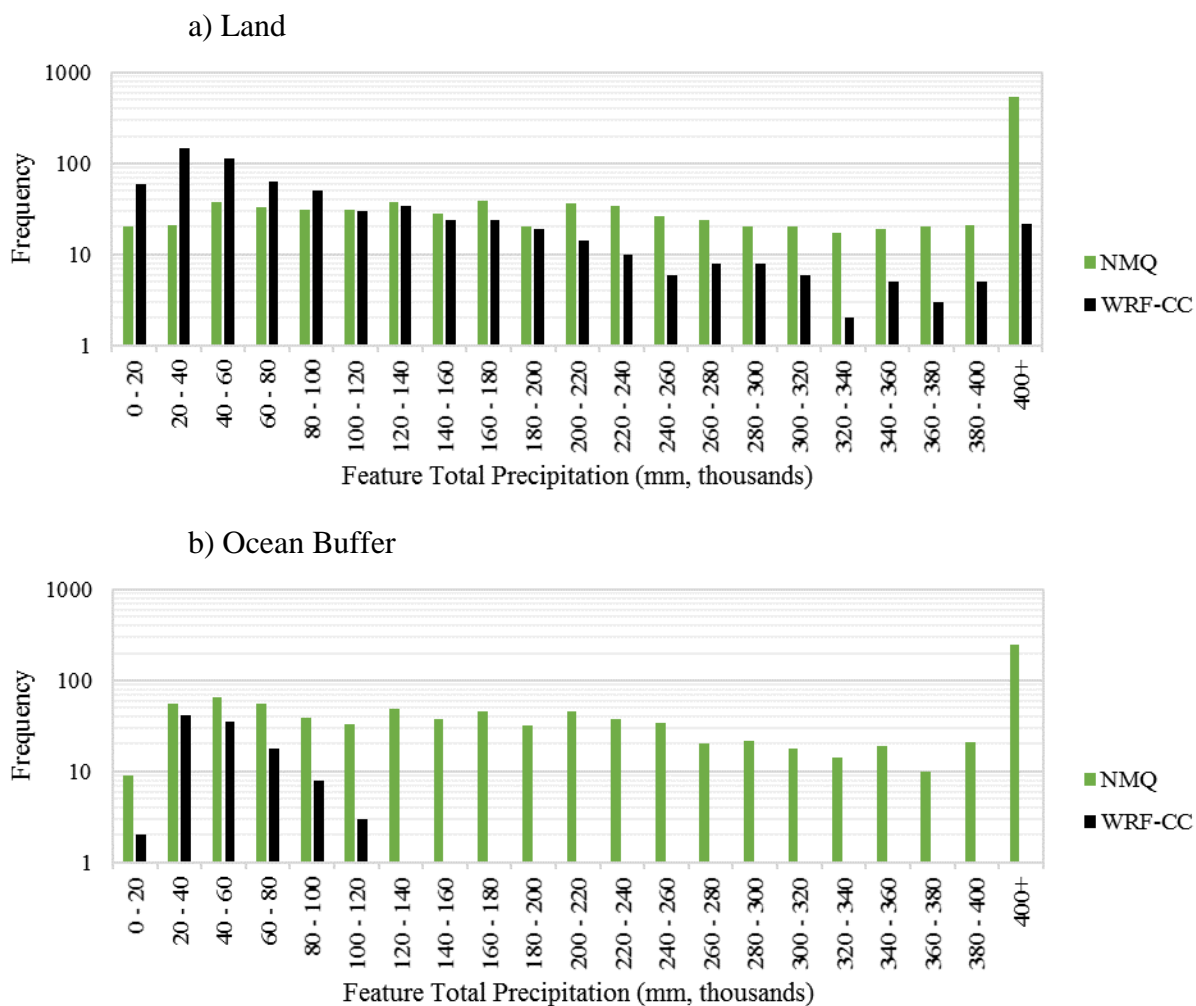


Figure 37 Same as Figure 36, but for MPF.

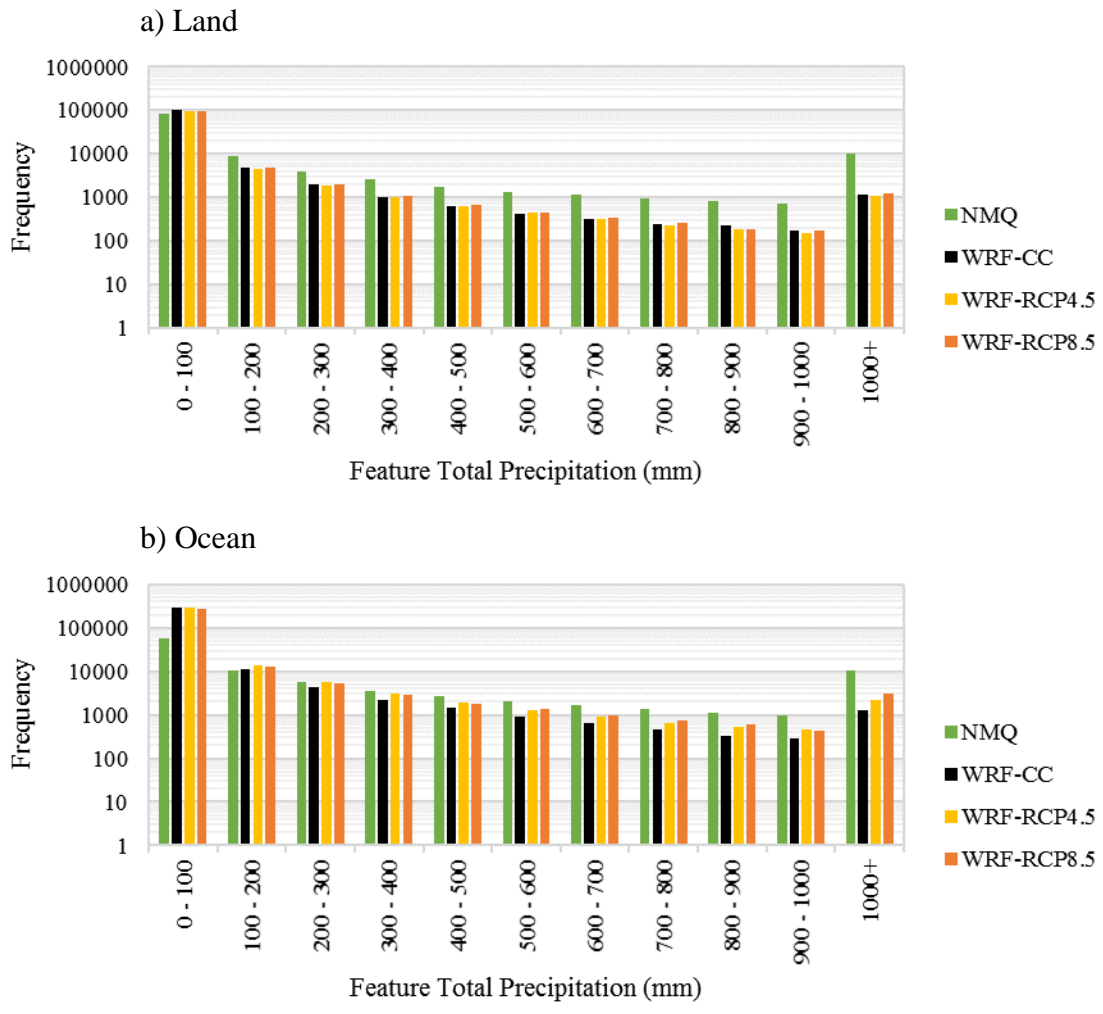


Figure 38 Histograms of IPF feature total precipitation (mm) in NMQ, WRF-CC, WRF-RCP4.5, and WRF-RCP8.5 over (a) the land and (b) the ocean.

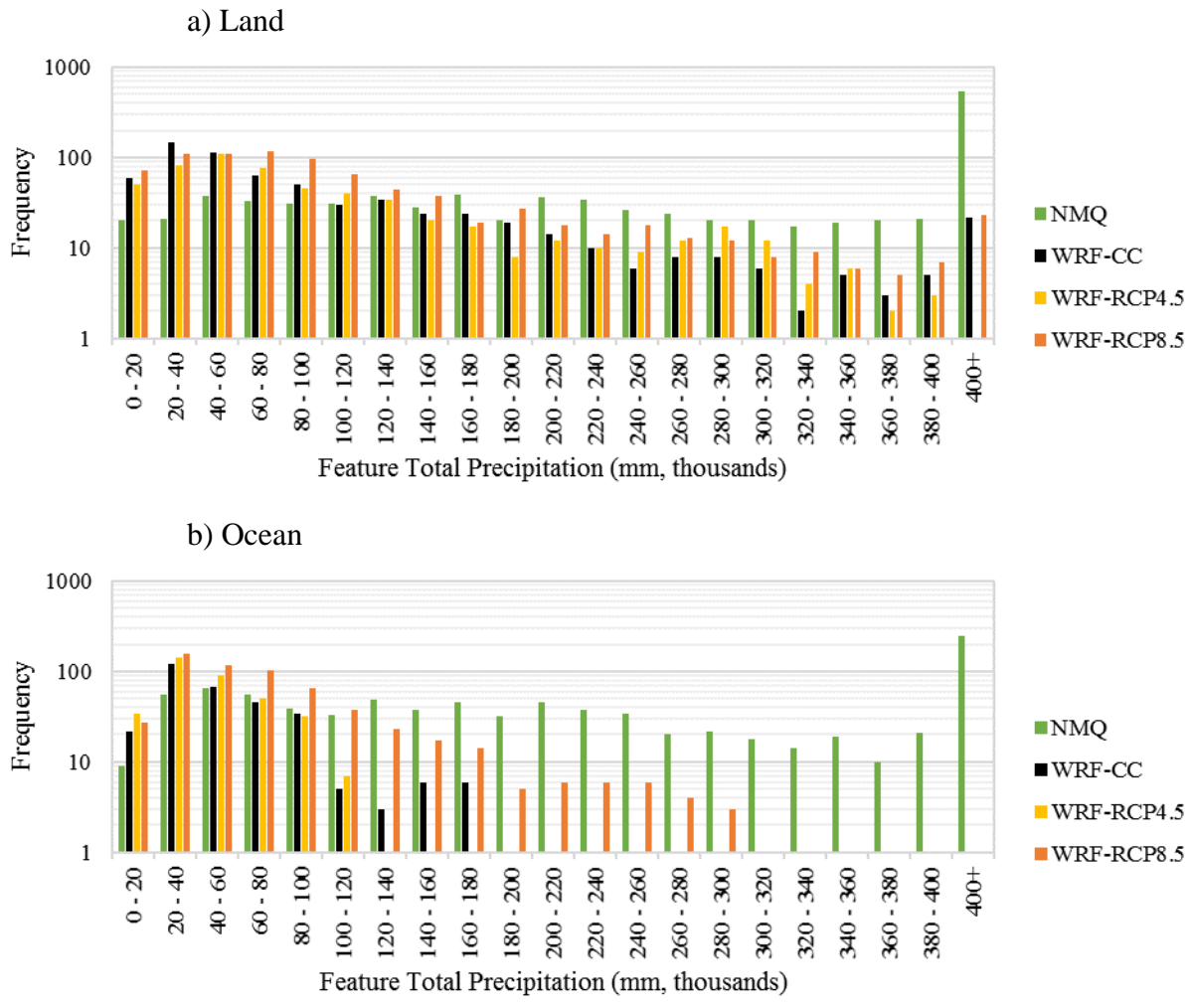


Figure 39 Same as Figure 38, but for MPF.

CHAPTER 5: DISCUSSION

This chapter will summarize and explain the major findings between the model and the observations and the model and the future climate simulations.

5.1 Model Evaluation

5.1.1 Total Precipitation

Total average precipitation in WRF-CC compared to within 1.55 mm, or roughly 6%, of the observed values in the NMQ dataset (Table 5). Despite this good performance, precipitation between the two datasets varied spatially across the domain. WRF-CC produced too little precipitation across the SE US coast, the Gulf Stream, the northern Gulf of Mexico, and portions of the Midwest (Figure 17a). On the other hand, WRF-CC produced excessive precipitation across portions of Ohio, West Virginia, and surrounding areas (Figure 17a).

5.1.2 Continental Precipitation

Continental precipitation in WRF-CC was 6.8 mm, or 30% higher, than in NMQ (Table 5). Because the magnitudes of total precipitation between WRF-CC and NMQ are similar across the SE US, this increase in continental precipitation could be due to the enhanced precipitation near West Virginia, increasing the average, despite having lower precipitation across the SE coast. It is possible that the lower sea level pressures (Figure 9a) and the stronger 850 mb Great Plains lower-level jet (Figure 7a) caused the frontal systems to penetrate farther south, shifting the axis of precipitation from the Midwest into West Virginia and areas farther eastward. It should be noted that radar data coverage is more limited over West Virginia compared to other areas in the SE US (Figure 1), which could suggest that the lower precipitation in NMQ is due to spotty data.

The majority of the precipitation across the SE US coast was tied to the sea breeze, which WRF-CC did manage to resolve. However, WRF-CC produced less precipitation near the coast compared to NMQ. It is hard to pinpoint exactly why WRF-CC produced less sea breeze precipitation, as it is a function of the model physics. A sensitivity study involving WRF physics parameterizations is necessary in order to answer this question, which is beyond the scope of this paper.

5.1.3 Ocean Buffer Precipitation

Ocean buffer precipitation in WRF-CC was 3.71 mm, or 14.5% less, than in NMQ (Table 5). Precipitation was lower over the northern Gulf of Mexico and over the Gulf Stream, where a heavy band of precipitation was present in NMQ (Figure 17a). Because of the closeness of the precipitation to the coast, the Gulf of Mexico precipitation is likely tied to the precipitation over land. The missing Gulf Stream precipitation in WRF-CC is more of a mystery, as it appears in WRF-RCP4.5 (Figure 15), but disappears in WRF-RCP8.5 (Figure 16).

5.1.4 Gulf Stream Precipitation

The Gulf Stream precipitation is a nocturnal phenomenon, which, in NMQ, appeared at around 3:00 UTC, peaked at around 12:00 UTC, and dissipated by 18:00 UTC (Figure 24). In WRF-CC, the precipitation developed at around 15:00 UTC, and dissipated by 18:00 UTC (Figure 25). In comparison, in WRF-RCP4.5, the band of precipitation developed at around 6:00 UTC, peaked at around 15:00 UTC, and dissipated by 18:00 UTC (Figure 26). The band did not appear at any hour in WRF-RCP8.5 (Figure 27).

In WRF-CC, the diurnal cycle of oceanic CAPE decreased between 9-18 UTC (when there was much less Gulf Stream precipitation than observed), but in NARR the CAPE actually increased (Figure 10). This would suggest that the diurnal cycle of oceanic CAPE in WRF-CC is

out of phase with NARR, which points to model energetics rather than convective parameterization as producing the lack of rain over the Gulf Stream.

In the NARR dataset, a weak 850 mb jet streak was located off the SE US coast (Figure 8, a). This feature appears even weaker in WRF-CC (Figure 5b), but is stronger again in WRF-RCP4.5 (Figure 5c) and in WRF-RCP8.5 (Figure 5d). The relation of this jet streak to the Gulf Stream precipitation is not well established. At the surface, the Gulf Stream precipitation occurs along the 1018 mb isobar, oriented southwest to northeast parallel to the coast, in the NARR dataset (Figure 8a). In WRF-CC, not only are the sea level pressures lower overall, but this 1018 mb isobar is oriented more south to north (Figure 8b). The orientation of the 1018 mb isobar does not change considerably in WRF-RCP4.5 (Figure 8c) or in WRF-RCP8.5 (Figure 8d).

As the SSTs remained static from the beginning of the simulation, it is possible that the Gulf Stream precipitation was missed due to a lack of SST update in WRF. Figure 40a illustrates the SSTs at the beginning of the model initialization, and Figure 40b shows the SSTs at the end of the simulation. Almost the entire western Atlantic warmed during this period, with some areas featuring warming in excess of 3°C (Figure 40d).

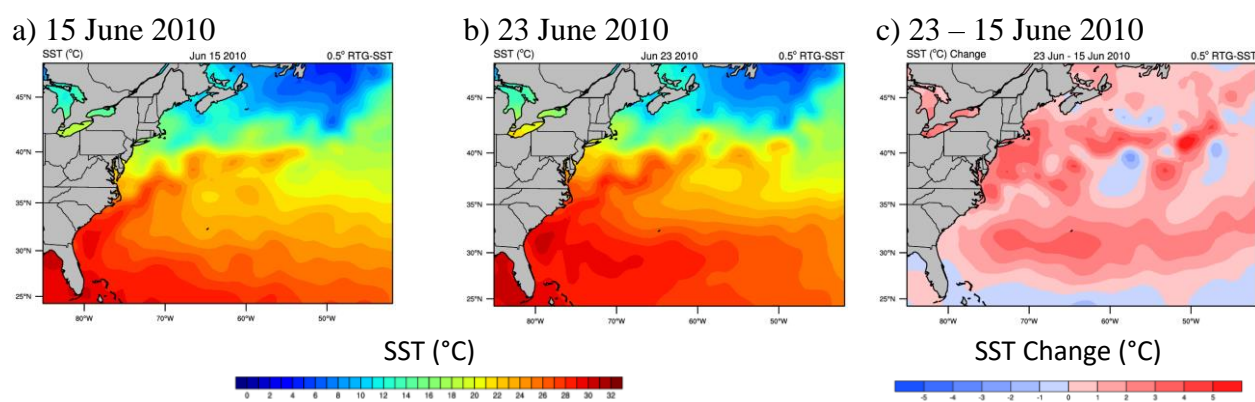


Figure 40 Comparison of SSTs from the 0.5° RTG-SST dataset on (a) 15 June 2010 at the initialization time of the WRF simulation and (b) on 23 June 2010 at the end of the simulation, together with (c) their differences.

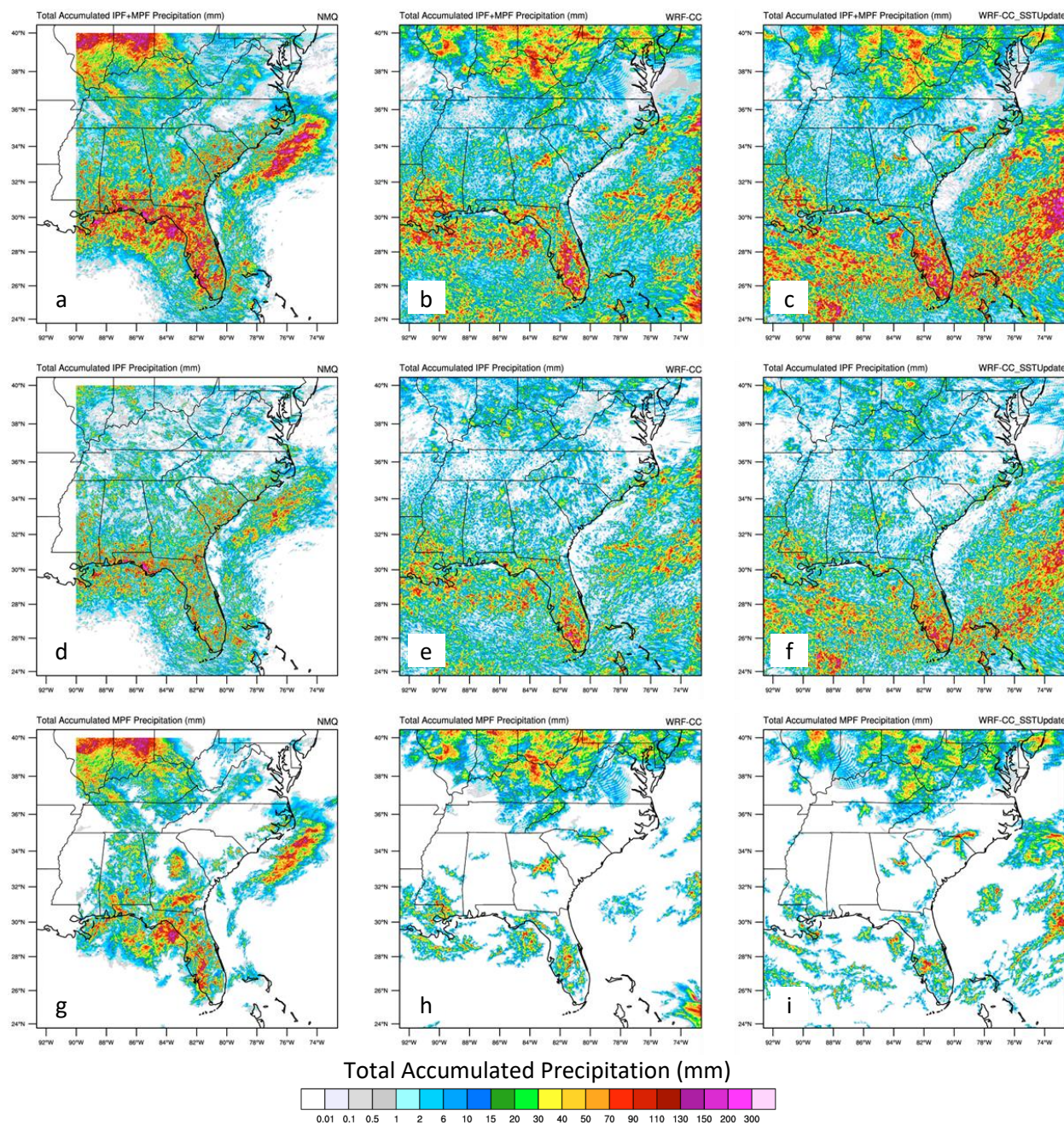


Figure 41 Comparison between (left column) NMQ, (middle column) WRF-CC, and (right column) WRF-CC with SST Update for (a-c) total IPF and MPF precipitation, (d-f) total IPF precipitation, and (g-i) total MPF precipitation.

An additional WRF simulation for WRF-CC was run with SST update turned on (Figure 41). The SST update simulation contained higher values of precipitation over the ocean, namely in the form of IPF. There was also an increase in oceanic MPF precipitation. While precipitation did increase slightly over the Gulf Stream, it still did not match the values in the NMQ dataset.

Therefore, it is likely that SSTs are not the main driver behind the missing Gulf Stream precipitation. Further simulations, mostly involving different physics options, will be needed to better understand the missing Gulf Stream precipitation in WRF.

5.1.5 Precipitation Features

The total number of precipitation features in WRF-CC compared to within 3.2% of NMQ (Table 7). WRF-CC also performed very well over the land, but produced 8.5% fewer features over the ocean buffer (Table 7). This difference is likely related to the missing Gulf Stream precipitation in WRF-CC. Nearly 99% of all precipitation features in NMQ and WRF-CC are IPF, with the remaining percentage constituting MPF. Interestingly, in NMQ MPF constitute a nearly identical fraction of total precipitation compared to IPF (Figure 20). In WRF-CC, MPF constitute 22.8% of all precipitation, which is 22.5% less than NMQ (Figure 20). WRF-CC produced 61.5% fewer MPF overall and nearly 88% fewer MPF over the ocean buffer (Table 7). Clearly, WRF has a bias towards IPF, and favors the development of isolated and discrete convective systems over broader, more organized MPF. This suggests an issue with the WRF convective parameterization, as mentioned previously.

5.1.6 IPF Precipitation

WRF-CC produced 7.27 mm more IPF precipitation than NMQ, with a 9.38 mm surplus in continental precipitation (Table 5). IPF precipitation in WRF-CC was significantly different from NMQ to the 95% level (Table 5). Even though WRF-CC produced more IPF precipitation, the total number of IPF in WRF-CC compared to within 3.1% of NMQ (Table 7). WRF-CC produced comparable IPF feature lengths to NMQ, but contained a greater number of smaller features 0-20 km in length (Figure 28). Despite the increase in IPF precipitation, WRF-CC echo heights were much shallower than NMQ (Figure 32). WRF-CC contained a surplus in IPF echo

heights 0-7 km in height, but contained fewer IPF 7-18 km in height (Figure 32). It is possible that WRF echo heights differed due to the calculation method, but MPF echo heights were more in line with NMQ.

5.1.7 MPF Precipitation

WRF-CC produced nearly half as much MPF precipitation as NMQ, with better performance over the continent and worse performance over the ocean buffer (Table 5). WRF-CC probably performed poorly over the ocean buffer because it had difficulty resolving the Gulf Stream precipitation. MPF feature lengths in WRF-CC compared well over the land, but were very different from NMQ over the ocean buffer (Figure 29). The poor performance over the ocean buffer is also possibly tied to the missing Gulf Stream precipitation. Even though WRF-CC produced fewer MPF, the MPF echo heights in WRF-CC contained similar distributions to NMQ (Figure 33).

5.1.8 CAPE and CIN

It is puzzling how different CAPE is between WRF-CC and NARR. Average CAPE in NARR is 2115.5 J/kg and average CAPE in WRF-CC is 1695.4 J/kg, a 420.1 J/kg difference. CAPE in WRF-CC is lower than NARR at all hours of the day (Figure 10a), including over the land and over the ocean (Figure 10b). Despite this discrepancy, total precipitation in WRF-CC and NMQ compare surprisingly well. CAPE in WRF-RCP4.5 is more similar to NARR than in WRF-CC. CIN in WRF-CC compares better to NARR (Figure 11), but CIN also features much smaller values than CAPE. Similarly, sea level pressures are much lower in WRF-CC than in NARR. It is possible that sea level pressures and CAPE differ so considerably in WRF-CC from the method that these values were calculated. Sea level pressure and CAPE in WRF were calculated using built-in WRF functions in NCAR Command Language (NCL), whereas all

NARR variables were precalculated and downloaded directly from the Earth System Resource Laboratory (ESRL) website.

5.2 Future Climates

Significant precipitation changes were seen in WRF-RCP8.5, including changes to IPF and MPF length and heights.

5.2.1 Total Precipitation

There is a trend towards more precipitation in the future climate simulations from heavier rain-producing IPF and a larger proportion of MPF. Total precipitation in WRF-RCP4.5 was 1.68 mm higher than WRF-CC, while total precipitation in WRF-RCP8.5 was 12.08 mm higher and significant to the 95% level (Table 6). While average precipitation does increase in the future climate simulations, there are spatial differences in precipitation across the domain, with some areas becoming wetter and other areas becoming dryer. Precipitation in WRF-RCP4.5 increased over the Carolinas, the Gulf of Mexico, and over the Gulf Stream, but was lower over Kentucky and Ohio (Figure 18a). Precipitation in WRF-RCP8.5 increased everywhere across the domain, with some drying in the SE US and Midwest region (Figure 19, a). Most changes in precipitation south of 36°N can be tied to the increased thermodynamic instability from the warmer temperatures in the future climate simulations. Precipitation north of 36°N, however, is more variable, as the precipitation in this region is tied to the passage of transient midlatitude cyclones.

5.2.2 Continental Precipitation

Total land precipitation in WRF-RCP4.5 decreased, but these values were not statistically significant (Table 6). WRF-RCP8.5 experienced a statistically significant 8.13 mm, or 27.6%,

increase in land precipitation (Table 6). Statistically significant increases were seen in IPF and MPF precipitation.

5.2.3 Oceanic Precipitation

Oceanic precipitation in WRF-RCP4.5 increased by 6.51 mm, or 27.1%, statistically significant to the 95% level (Table 6). However, it should be noted that this was due to a 6.50 mm increase in IPF precipitation, as MPF precipitation did not change (Table 6). WRF-RCP8.5 saw a 16.03 mm, or a 66.8%, increase in oceanic precipitation, statistically significant to the 95% level (Table 6). IPF and MPF precipitation both increased significantly from WRF-CC. The largest increases in precipitation occurred in the norther Gulf of Mexico and the western Atlantic near the coast of Florida (Figure 19).

5.2.4 Precipitation Features

The effect of warmer temperatures on precipitation features is complicated, as the total number of features remained steady in WRF-RCP4.5, but decreased in WRF-RCP8.5 (Table 8). In WRF-RCP4.5, the total number of features decreased by 10,920 over land, but increased by 12,003 over the ocean, cancelling each other out (Table 8). The increase in the number of oceanic features might be related to the Gulf Stream precipitation that was captured in WRF-RCP4.5, but not in the other simulations. The decrease in land features is harder to explain, as it might just be due to natural variability from the transient frontal systems in the northern part of the domain. The total number of MPF was also lower in WRF-RCP4.5 (Table 8). The total number of features in WRF-RCP8.5 decreased by 14,350, which is mostly from IPF, while the total number of MPF increased by 495 (Table 8). It is likely that IPF in WRF-RCP8.5 grew larger and coalesced with other IPF, resulting in fewer but larger IPF and more MPF.

5.2.5 IPF Precipitation

IPF precipitation in WRF-RCP4.5 increased by 2.31 mm, or 11.1%, statistically significant to the 95% level (Table 6). While IPF precipitation decreased over land, it increased significantly over the ocean. In WRF-RCP8.5, IPF precipitation increased by 8.23 mm, or 39.5%, statistically significant from WRF-CC (Table 6). In WRF-RCP8.5, the largest changes in IPF precipitation occurred over the ocean, where a 12.25 mm, or a 56.5%, increase occurred (Table 6). IPF feature lengths increased marginally over the continent in the future climate simulations (Figure 30a). The greatest changes in IPF feature length occurred over the ocean, with the largest changes in WRF-RCP8.5 (Figure 30b). Even though IPF echo heights did not compare well to NMQ, significant changes were seen in the future climate simulations. Over the continent, the number of IPF with echo heights greater than 12 km increased considerably, including the addition of a few features 18-20+ km in height, which were not present in NMQ nor in the other simulations (Figure 34a). Oceanic IPF 11-19 km in height also increased in the future climate simulations, with the greatest differences in WRF-RCP8.5 (Figure 34b).

5.2.6 MPF Precipitation

The greatest changes in MPF precipitation occurred in WRF-RCP8.5, which increased by 85.2%, statistically significant to the 95% level (Table 6). MPF precipitation increased by 63.4% over the land and 161.8% over the ocean, both statistically significant to the 95% level (Table 6). MPF feature lengths increased over land in the future climate simulations, with the greatest changes in WRF-RCP8.5. Even greater changes were seen over the ocean, where there was a notable increase in MPF 100-300 km in length (Figure 31b). MPF echo heights 3-10 km in length increased over land in the future climate simulations, possibly due to the larger number of MPF overall (Figure 35a). Land MPF echo heights 11-15 km decreased, while an increase was

seen again in echo heights 16-20 km in height (Figure 35a). MPF echo heights also increased over the ocean, with the greatest changes for features 15-19 km in height (Figure 35b). These increases in MPF echo heights and feature lengths are consistent with stronger and heavier rain-producing thunderstorms in the future climate simulations.

5.2.7 CAPE and CIN

Average CAPE in WRF-RCP4.5 increased by 347.7 J/kg and by 810.0 J/kg in WRF-RCP8.5. The largest increases in CAPE were seen over the ocean, with a nearly 400 J/kg increase per RCP (Figure 10b). The diurnal minimum and maximum values of CAPE occurred at the same hours in the future climate simulations (Figure 10). The increase in CAPE coincides with the increases in precipitation in the future climate simulations. CIN also increased in proportion to CAPE, which allowed the thunderstorms to develop at the same hour of the day in the future climate simulations.

Simulation	CAPE (J/kg)	850 mb Temp. (°C)	500 mb Temp. (°C)	300 mb Temp. (°C)
WRF-CC	1695.4	18.1	-6.4	-32.7
WRF-RCP4.5	2043.1	19.9	-4.3	-29.8
WRF-RCP8.5	2505.5	21.8	-2.3	-27.3

Table 9 Average CAPE (J/kg) and 850, 500, and 300 mb temperature (°C) from 17 June at 0z to 23 June at 0z 2010 for the 3 km domain.

The higher values of CAPE coincide with the warmer temperatures in the future climate simulations. Temperatures increased by roughly 2°C per RCP in the lowest layers of the atmosphere, with a nearly 4°C increase in WRF-RCP8.5 compared to WRF-CC (Table 9). The temperature changes in the upper-levels of the atmosphere near 300 mb featured a more dramatic 3°C increase per RCP (Table 9). These temperature anomalies were maintained throughout the simulations.

CHAPTER 6: CONCLUSION

WRF performed well in simulating the observed patterns of precipitation features in the NMQ dataset. However, WRF does have some biases. There are also interesting changes in the characteristics and distributions of precipitation features in the future climate simulations. Here the research questions listed in Chapter 1 are directly addressed:

1. *How well does WRF-simulated precipitation organization compare to the observations in the NMQ dataset?* Precipitation totals in WRF compared to within 6% of the observed totals in the NMQ dataset, which is surprisingly good for a NWP model. However, WRF differed from NMQ in the mode-of-delivery of the precipitation. Even though IPF constitute nearly 99% of all features identified in NMQ, they produce only about half of the total observed precipitation. In WRF-CC, on the other hand, even though the total number of features in WRF compared to within 3.2% of those in NMQ, IPF produced a much larger percentage (77.2%) of the total precipitation. Precipitation features in WRF tend to be smaller in size, which favors the development of IPF over MPF. IPF feature lengths compared well between WRF and NMQ, but WRF produced shallower features that did not extend as deeply into the troposphere.
2. *Will the increase in temperature cause a shift in the distributions of precipitation organization? If so, will there be a shift towards more IPF or MPF?* Feature distributions did not change considerably in WRF-RCP4.5, but WRF-RCP8.5 did see notable shifts in the distributions of IPF and MPF. In the future climate simulations, IPF still constitute nearly 99% of all precipitation features, but there is a trend towards more MPF. While the total number of precipitation features in WRF-RCP8.5 decreased by 3.3%, the total number of MPF increased by 48.2%. There was also an 85.2% increase in precipitation produced by

MPF in WRF-RCP8.5. This boosted the fraction of total precipitation produced by MPF by 3.0%.

3. *How will the horizontal and vertical structure of precipitation organization change?* As the warming is increased, IPF have the tendency to coalesce into larger precipitation features with some merging into MPF. This is reflected in the decrease in the total number of IPF and the increase the number of MPF. There is a tendency for precipitation features to become longer in length and grow deeper in size. Likewise, these precipitation features produce more precipitation overall in the future climate simulations.
4. *How will precipitation totals in general change?* Total precipitation did not change considerably in WRF-RCP4.5, but WRF-RCP8.5 did see a significant increase in total accumulated domain-averaged precipitation by 12.08 mm. In WRF-RCP8.5, IPF and MPF precipitation also increased significantly across the land and ocean. The greatest changes in precipitation occurred in the northeastern Gulf of Mexico and off the east coast of Florida. These increases in precipitation are directly related to the warmer temperatures in the future climate simulations, as evidenced by higher values of CAPE.

This study has demonstrated that it is possible to apply the Rickenbach et al. (2015) feature identification algorithm to non-observational datasets, such as NWP output from WRF. This allows the study of precipitation features in areas that contain poor radar data coverage. More research is still necessary in order to understand and improve the biases in the WRF precipitation features examined in this study.

REFERENCES

- Adachi, S. et al., 2012. Comparison of the impact of global climate changes and urbanization on summertime future climate in the Tokyo metropolitan area. *Journal of Applied Meteorology and Climatology*, 51(8), pp.1441–1454.
- Allen, M.R. & Ingram, W.J., 2002. Constraints on future changes in climate and the hydrologic cycle. *Nature*, 419(6903), pp.224–232.
- Anon, Global Forecast System (GFS). Available at: <https://www.ncdc.noaa.gov/data-access/model-data/model-datasets/global-forecast-system-gfs> [Accessed January 1, 2016].
- Bi, D. et al., 2013. The ACCESS coupled model: description, control climate and evaluation. *Australian Meteorological and Oceanographic Journal*, 63, pp.41–64.
- Castro, C.L., 2005. Dynamical downscaling: Assessment of value retained and added using the Regional Atmospheric Modeling System (RAMS). *Journal of Geophysical Research*, 110(D5), pp.1–21. Available at: <http://doi.wiley.com/10.1029/2004JD004721>.
- Cubasch, U. et al., 2001. Projections of Future Climate Change. *Climate Change 2001: The Scientific Basis. Contribution of Working Group I to the Third Assessment Report of the Intergovernmental Panel on Climate Change*, p.881.
- Doswell, C. a. I. & Schultz, D.M., 2006. On the Use of Indices and Parameters in Forecasting Severe Storms. *Electronic Journal of Severe Storms Meteorology*, 1(3), pp.1–22. Available at: <http://secure755.hostgator.com/~elke/ojs/index.php/ejssm/article/viewArticle/11>.
- Ferreira, R.N., Hall, L. & Rickenbach, T.M., 2013. A climatology of the structure, evolution, and propagation of midlatitude cyclones in the southeast united states. *Journal of Climate*, 26(21), pp.8406–8421.
- Flato, G. et al., 2013. Evaluation of Climate Models. In Intergovernmental Panel on Climate Change, ed. *Climate Change 2013 - The Physical Science Basis*. Cambridge: Cambridge University Press, pp. 741–866. Available at: <http://ebooks.cambridge.org/ref/id/CBO9781107415324A028>.
- Frei, C. et al., 1998. Heavy precipitation processes in a warmer climate. *Geophysical Research Letters*, 25(9), p.1431.
- Fujihara, Y. et al., 2008. Assessing the impacts of climate change on the water resources of the Seyhan River Basin in Turkey: Use of dynamically downscaled data for hydrologic simulations. *Journal of Hydrology*, 353(1-2), pp.33–48.
- Gutmann, E.D. et al., 2012. A comparison of statistical and dynamical downscaling of winter precipitation over complex terrain. *Journal of Climate*, 25(1), pp.262–281.
- Hara, M. et al., 2008. Estimation of the Impact of Global Warming on Snow Depth in Japan by the Pseudo-Global-Warming Method. *Hydrological Research Letters*, 2(5), pp.61–64.

Available at: <http://joi.jlc.jst.go.jp/JST.JSTAGE/hrl/2.61?from=CrossRef>.

- Held, I.M. & Soden, B.J., 2006. Robust responses of the hydrological cycle to global warming. *Journal of Climate*, 19(21), pp.5686–5699.
- Hill, K. a. & Lackmann, G.M., 2011. The impact of future climate change on TC intensity and structure: A downscaling approach. *Journal of Climate*, 24(17), pp.4644–4661.
- Hong, S. & Lim, J., 2006. The WRF single-moment 6-class microphysics scheme (WSM6). *Journal of the Korean Meteorological Society*, 42(2), pp.129–151. Available at: http://www.mmm.ucar.edu/wrf/users/docs/WSM6-hong_and_lim_JKMS.pdf \n http://search.koreanstudies.net/journal/thesis_name.asp?tname=kiss2002&key=2525908.
- Hong, S.-Y., Dudhia, J. & Chen, S.-H., 2004. A Revised Approach to Ice Microphysical Processes for the Bulk Parameterization of Clouds and Precipitation. *Monthly Weather Review*, 132(1), pp.103–120. Available at: [http://journals.ametsoc.org/doi/abs/10.1175/1520-0493\(2004\)132<0103:ARATIM>2.0.CO;2](http://journals.ametsoc.org/doi/abs/10.1175/1520-0493(2004)132<0103:ARATIM>2.0.CO;2).
- Hong, S.-Y., Noh, Y. & Dudhia, J., 2006. A New Vertical Diffusion Package with an Explicit Treatment of Entrainment Processes. *Monthly Weather Review*, 134(9), pp.2318–2341. Available at: <http://journals.ametsoc.org/doi/abs/10.1175/MWR3199.1>.
- Houze, R.A., Smull, B.F. & Dodge, P., 1990. Mesoscale Organization of Springtime Rainstorms in Oklahoma. *Monthly Weather Review*, 118(3), pp.613–654.
- Hurrell, J.W. et al., 2013. The Community Earth System Model: A Framework for Collaborative Research. *Bulletin of the American Meteorological Society*, 94(9), pp.1339–1360. Available at: <http://journals.ametsoc.org/doi/abs/10.1175/BAMS-D-12-00121.1>.
- Iacono, M.J. et al., 2008. Radiative forcing by long-lived greenhouse gases: Calculations with the AER radiative transfer models. *Journal of Geophysical Research*, 113(D13), p.D13103. Available at: <http://doi.wiley.com/10.1029/2008JD009944>.
- Iizumi, T., Hayashi, Y. & Kimura, F., 2007. Influence on Rice Production in Japan from Cool and Hot Summers after Global Warming. *Journal of Agricultural Meteorology*, 63(1), pp.11–23.
- Janjić, Z.I., 1994. The Step-Mountain Eta Coordinate Model: Further Developments of the Convection, Viscous Sublayer, and Turbulence Closure Schemes. *Monthly Weather Review*, 122(5), pp.927–945. Available at: [http://journals.ametsoc.org/doi/abs/10.1175/1520-0493\(1994\)122<0927:TSMECM>2.0.CO;2](http://journals.ametsoc.org/doi/abs/10.1175/1520-0493(1994)122<0927:TSMECM>2.0.CO;2).
- Jones, C.D. et al., 2011. The HadGEM2-ES implementation of CMIP5 centennial simulations. *Geoscientific Model Development Discussions*, 4(1), pp.689–763.
- Kanada, S., Wada, A. & Sugi, M., 2013. Future changes in structures of extremely intense

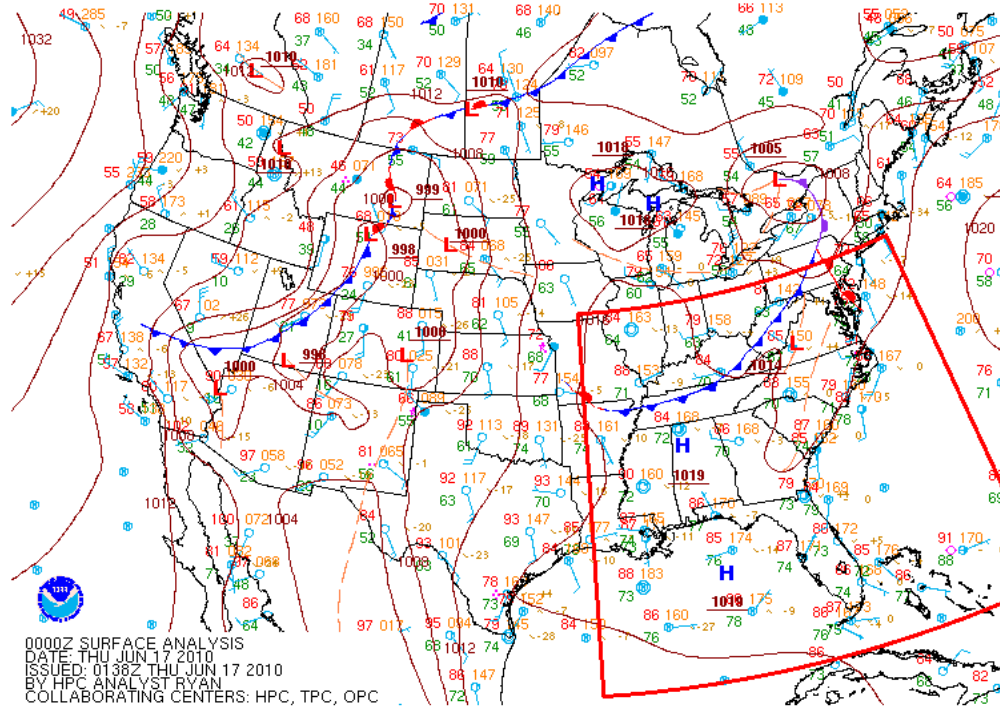
- tropical cyclones using a 2-km mesh nonhydrostatic model. *Journal of Climate*, 26(24), pp.9986–10005.
- Kawase, H. et al., 2008. Downscaling of the Climatic Change in the Mei-yu Rainband in East Asia by a Pseudo Climate Simulation Method. *SOLA*, 4(c), pp.73–76. Available at: <http://joi.jlc.jst.go.jp/JST.JSTAGE/sola/2008-019?from=CrossRef>.
- Kharin, V. V. et al., 2007. Changes in Temperature and Precipitation Extremes in the IPCC Ensemble of Global Coupled Model Simulations. *Journal of Climate*, 20(8), pp.1419–1444. Available at: <http://journals.ametsoc.org/doi/abs/10.1175/JCLI4066.1>.
- Kimura, F. & Kitoh, A., 2007. Downscaling by Pseudo Global Warming Method. *The Final Report of ICCAP*, 10, pp.2–5. Available at: http://www.chikyu.ac.jp/iccip/ICCAP_Final_Report/2/4-climate_kimura.pdf.
- Lackmann, G.M., 2013. The South-Central U.S. Flood of May 2010: Present and Future*. *Journal of Climate*, 26(13), pp.4688–4709. Available at: <http://journals.ametsoc.org/doi/abs/10.1175/JCLI-D-12-00392.1>.
- Li, L., Li, W. & Deng, Y., 2013. Summer rainfall variability over the southeastern united states and its intensification in the 21st century as assessed by cmip5 models. *Journal of Geophysical Research: Atmospheres*, 118(2), pp.340–354.
- Li, W. et al., 2011. Changes to the North Atlantic Subtropical High and Its Role in the Intensification of Summer Rainfall Variability in the Southeastern United States. *Journal of Climate*, 24(5), pp.1499–1506. Available at: <http://journals.ametsoc.org/doi/abs/10.1175/JCLI-D-11-00674.1>.
- Mallard, M.S., Lackmann, G.M. & Aiyyer, A., 2013. Atlantic Hurricanes and Climate Change. Part II: Role of Thermodynamic Changes in Decreased Hurricane Frequency. *Journal of Climate*, 26(21), pp.8513–8528. Available at: <http://journals.ametsoc.org/doi/abs/10.1175/JCLI-D-12-00183.1>.
- Martin, G.M. et al., 2011. The HadGEM2 family of Met Office Unified Model climate configurations. *Geoscientific Model Development*, 4(3), pp.723–757. Available at: <http://www.geosci-model-dev.net/4/723/2011/>.
- Mesinger, F. et al., 2006. North American Regional Reanalysis. *Bulletin of the American Meteorological Society*, 87(3), pp.343–360. Available at: <http://journals.ametsoc.org/doi/abs/10.1175/BAMS-87-3-343>.
- Murakami, M., 1990. Numerical Modeling of Dynamical and Microphysical Evolution of an Isolated Convective Cloud - The 19 July 1981 CCOPE cloud. *J. Meteor. Soc. Japan*, 68(April), pp.107–128.
- Nieto Ferreira, R. & Earl Hall, L., 2015. Midlatitude cyclones in the southeastern United States: frequency and structure differences by cyclogenesis region. *International Journal of Climatology*, 35(13), pp.3798–3811. Available at: <http://doi.wiley.com/10.1002/joc.4247>.

- Pall, P., Allen, M.R. & Stone, D. a., 2007. Testing the Clausius-Clapeyron constraint on changes in extreme precipitation under CO₂ warming. *Climate Dynamics*, 28(4), pp.351–363.
- Rasmussen, R. et al., 2011. High-resolution coupled climate runoff simulations of seasonal snowfall over Colorado: A process study of current and warmer climate. *Journal of Climate*, 24(12), pp.3015–3048.
- Rickenbach, T.M. et al., 2015. A seasonal and diurnal climatology of precipitation organization in the southeastern United States. *Quarterly Journal of the Royal Meteorological Society*, 141(690), pp.1938–1956. Available at: <http://doi.wiley.com/10.1002/qj.2500>.
- Sato, T., Kimura, F. & Kitoh, A., 2007. Projection of global warming onto regional precipitation over Mongolia using a regional climate model. *Journal of Hydrology*, 333(1), pp.144–154.
- Schär, C., Lüthi, D. & Davies, H.C., 1996. Surrogate climate-change scenarios for regional climate models. *Geophysical Research Letters*, 23(6), pp.669–672.
- Skamarock, W.C. et al., 2008. A Description of the Advanced Research WRF Version 3. *Technical Report*, (June), p.113.
- Stevens, B. et al., 2013. Atmospheric component of the MPI-M Earth System Model: ECHAM6. *Journal of Advances in Modeling Earth Systems*, 5(2), pp.146–172. Available at: <http://doi.wiley.com/10.1002/jame.20015>.
- Stocker, T.F. et al., 2013. Technical Summary. In Intergovernmental Panel on Climate Change, ed. *Climate Change 2013 - The Physical Science Basis*. Cambridge: Cambridge University Press, pp. 31–116. Available at: <http://ebooks.cambridge.org/ref/id/CBO9781107415324A011>.
- Stouffer, R.J., Taylor, K.E. & Meehl, G.A., 2011. CMIP5 Long-Term Experimental Design. *CLIVAR Exchanges Newsletter*, 16(2), pp.5–7. Available at: http://www.clivar.org/sites/default/files/imported/publications/exchanges/Exchanges_56.pdf.
- Taylor, K.E., Stouffer, R.J. & Meehl, G.A., 2012. An overview of CMIP5 and the experiment design. *Bulletin of the American Meteorological Society*, 93(4), pp.485–498.
- Tewari, M. et al., 2004. Implementation and verification of the unified noah land surface model in the WRF model. In *Bulletin of the American Meteorological Society*. pp. 2165–2170. Available at: <http://link.springer.com/10.1007/s11269-013-0452-7>.
- Thiébaux, J. et al., 2003. A New High-Resolution Blended Real-Time Global Sea Surface Temperature Analysis. *Bulletin of the American Meteorological Society*, 84(5), pp.645–656. Available at: <http://journals.ametsoc.org/doi/abs/10.1175/BAMS-84-5-645>.
- Tsunematsu, N. et al., 2011. Potential impact of spatial patterns of future atmospheric warming on Asian dust emission. *Atmospheric Environment*, 45(37), pp.6682–6695. Available at: <http://dx.doi.org/10.1016/j.atmosenv.2011.08.048>.

- Ueyama, H., 2012. Estimation methods for monthly humidity from dynamical downscaling data for quantitative assessments of climate change impacts. *Theoretical and Applied Climatology*, 109(1-2), pp.15–26.
- Walko, R.L. et al., 1995. An Interactive Nesting Algorithm for Stretched Grids and Variable Nesting Ratios. *Journal of Applied Meteorology*, 34(4), pp.994–999. Available at: [http://journals.ametsoc.org/doi/abs/10.1175/1520-0450\(1995\)034<0994:AINAFS>2.0.CO;2](http://journals.ametsoc.org/doi/abs/10.1175/1520-0450(1995)034<0994:AINAFS>2.0.CO;2).
- Wang, H. et al., 2010. Intensification of Summer Rainfall Variability in the Southeastern United States during Recent Decades. *Journal of Hydrometeorology*, 11(4), pp.1007–1018. Available at: <http://journals.ametsoc.org/doi/abs/10.1175/2010JHM1229.1>.
- Willison, J., Robinson, W. a. & Lackmann, G.M., 2015. North Atlantic Storm-Track Sensitivity to Warming Increases with Model Resolution. *Journal of Climate*, 28(11), pp.4513–4524. Available at: <http://journals.ametsoc.org/doi/abs/10.1175/JCLI-D-14-00715.1>.
- Yoshikane, T. et al., 2012. Verification of the Performance of the Pseudo-Global-Warming Method for Future Climate Changes during June in East Asia. *SOLA*, 8, pp.133–136. Available at: <http://japanlinkcenter.org/DN/JST.JSTAGE/sola/2012-033?lang=en&from=CrossRef&type=abstract>.
- Zhang, J. et al., 2011. National Mosaic and Multi-Sensor QPE (NMQ) System: Description, Results, and Future Plans. *Bulletin of the American Meteorological Society*, 92(10), pp.1321–1338. Available at: <http://journals.ametsoc.org/doi/abs/10.1175/2011BAMS-D-11-00047.1>.

APPENDIX: SURFACE AND UPPER AIR WEATHER MAPS

17 June 2010



18 June 2010

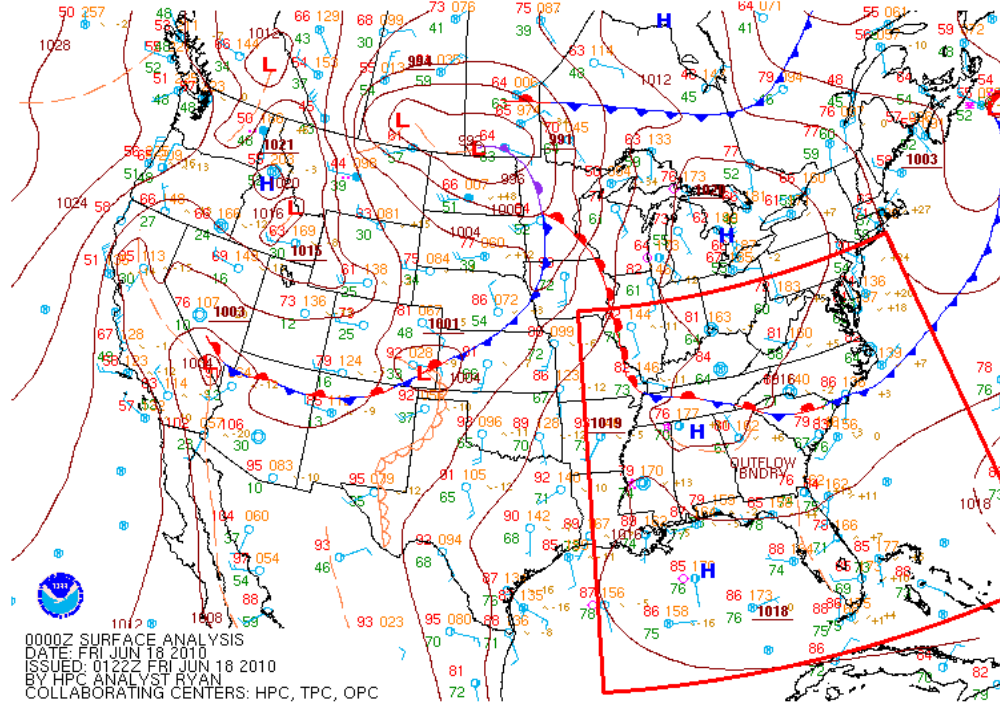


Figure 42 Daily 0:00 UTC surface analysis plots from the Storm Prediction Center (SPC). The location of the 3 km WRF domain has been outlined in red.

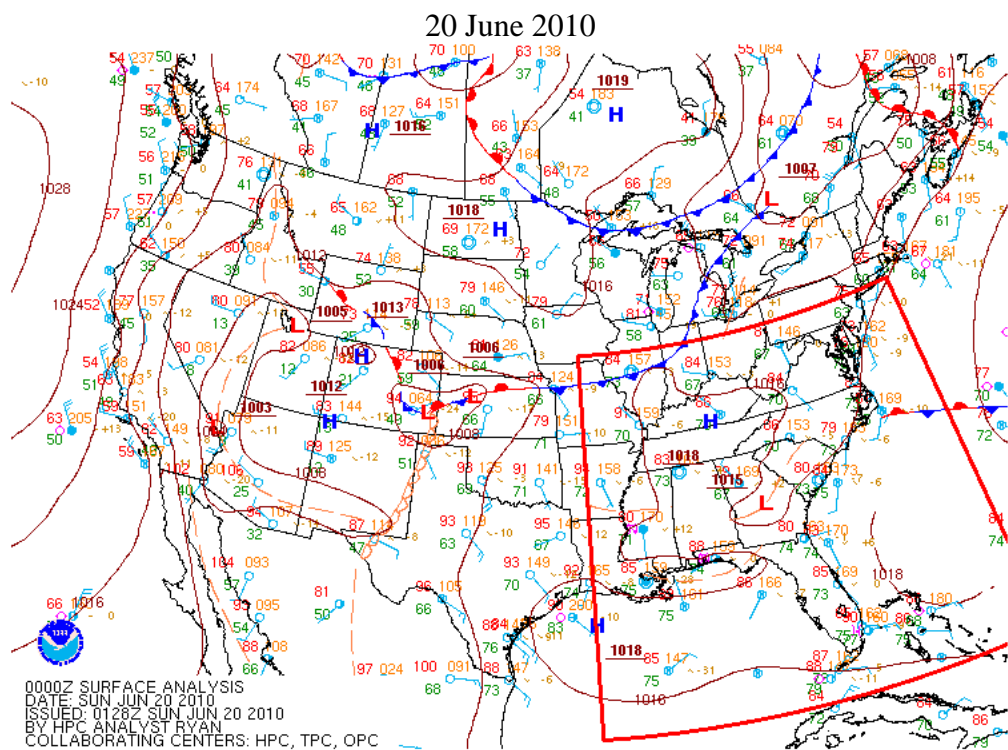
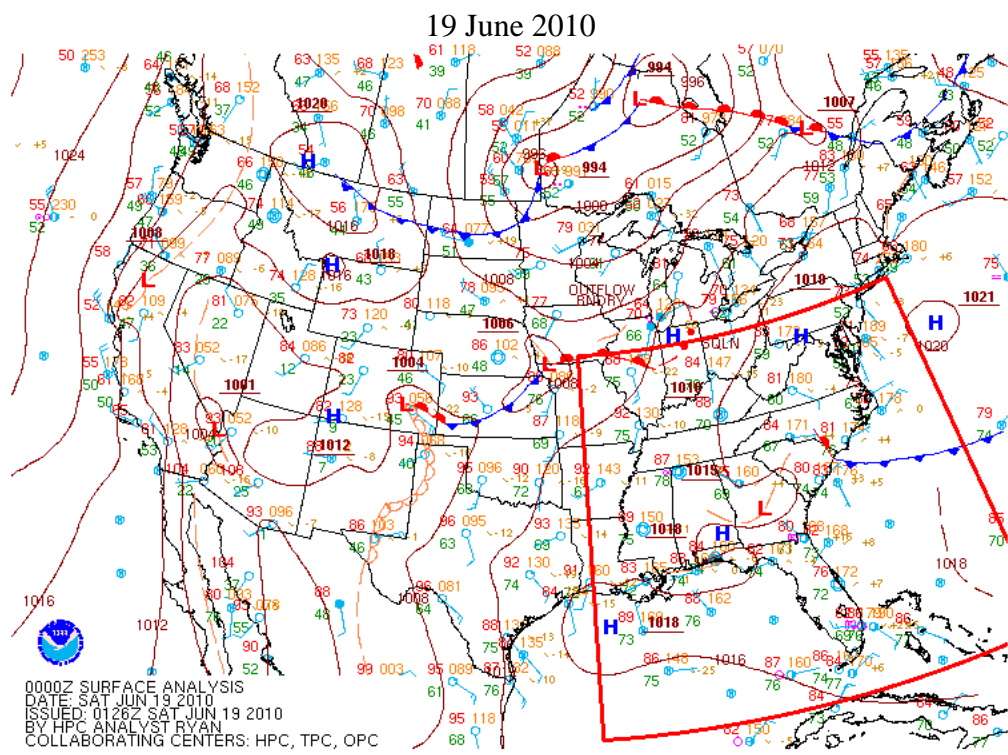


Figure 42 continued.

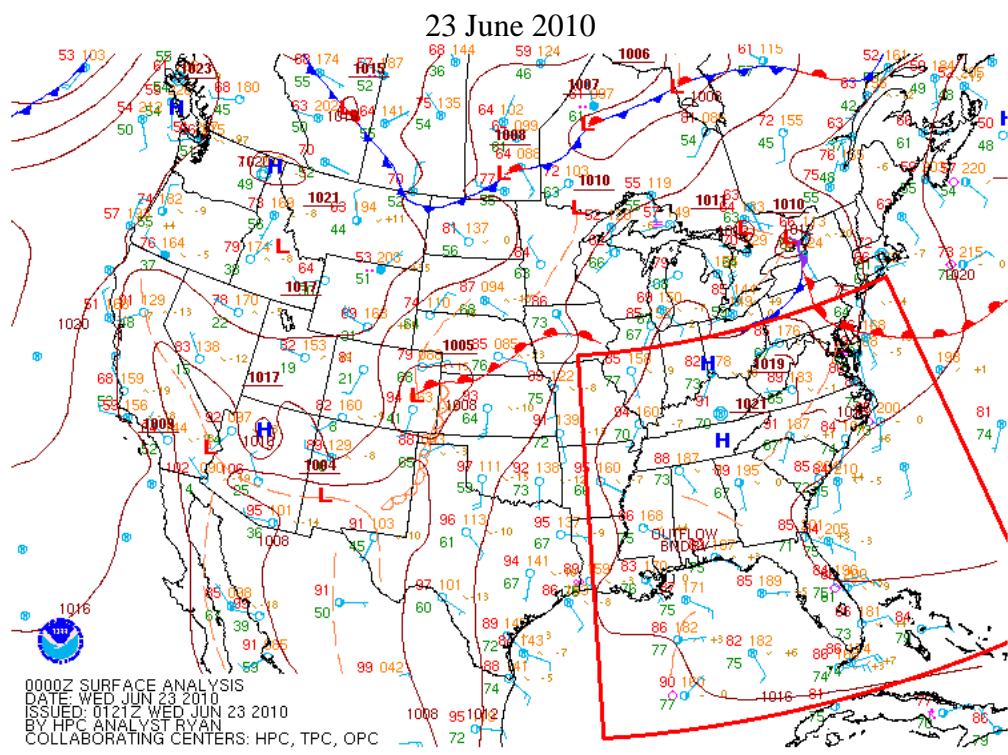


Figure 42 continued.

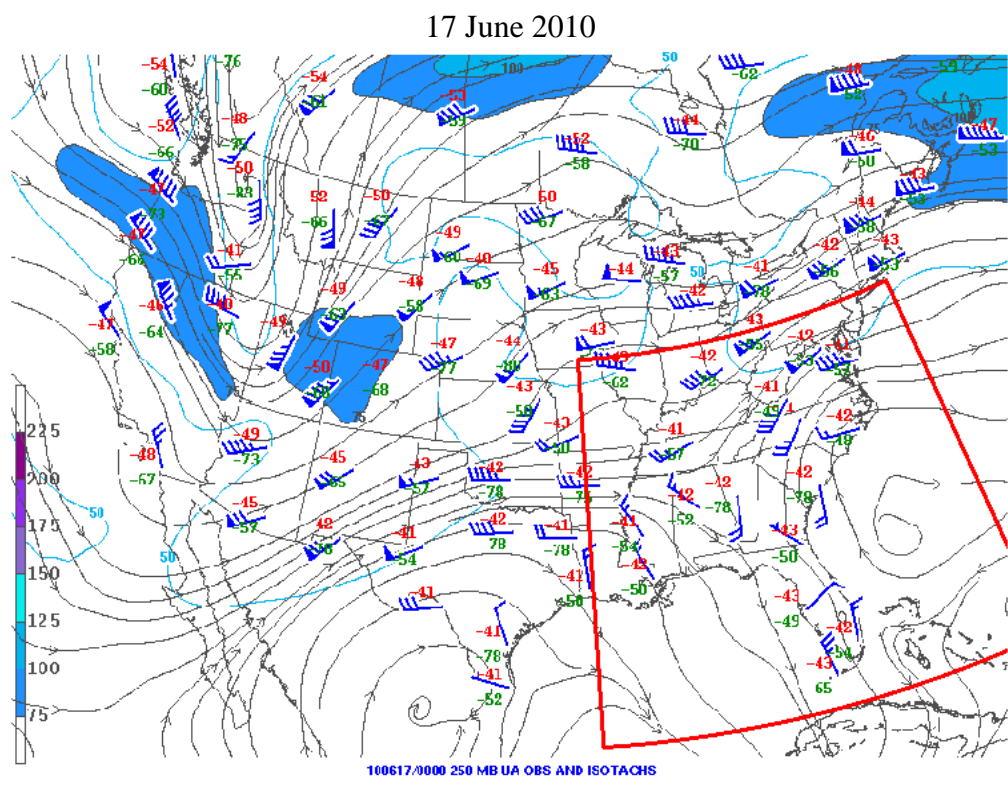
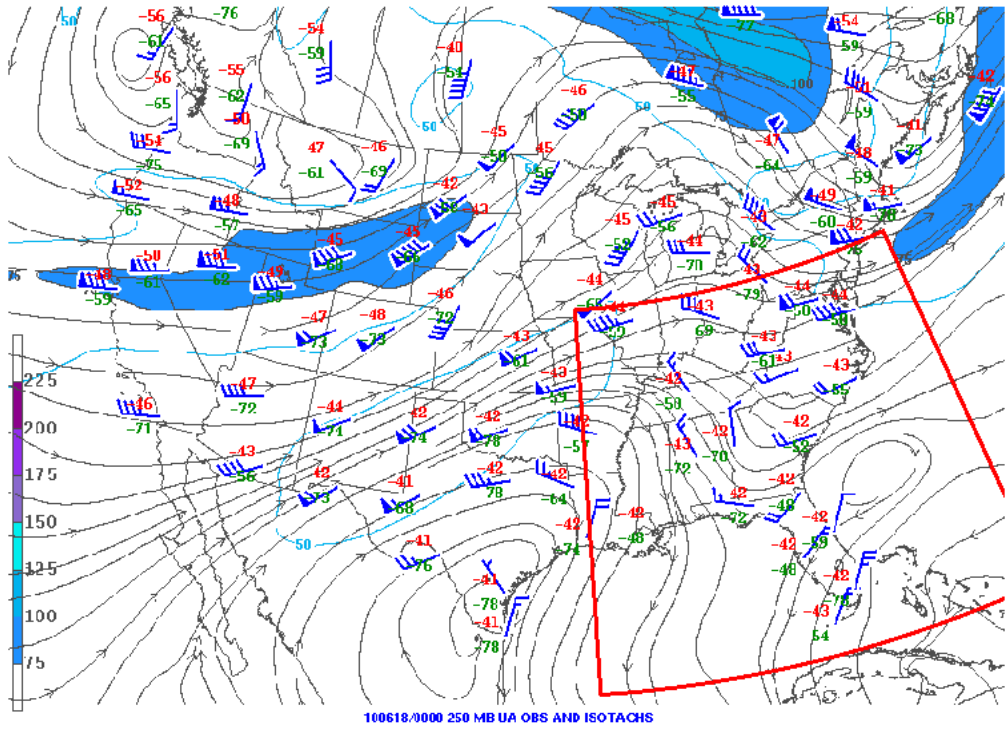


Figure 43 Daily 0:00 UTC upper air plots at 250 mb from the SPC. The location of the 3 km WRF domain has been outlined in red.

18 June 2010



19 June 2010

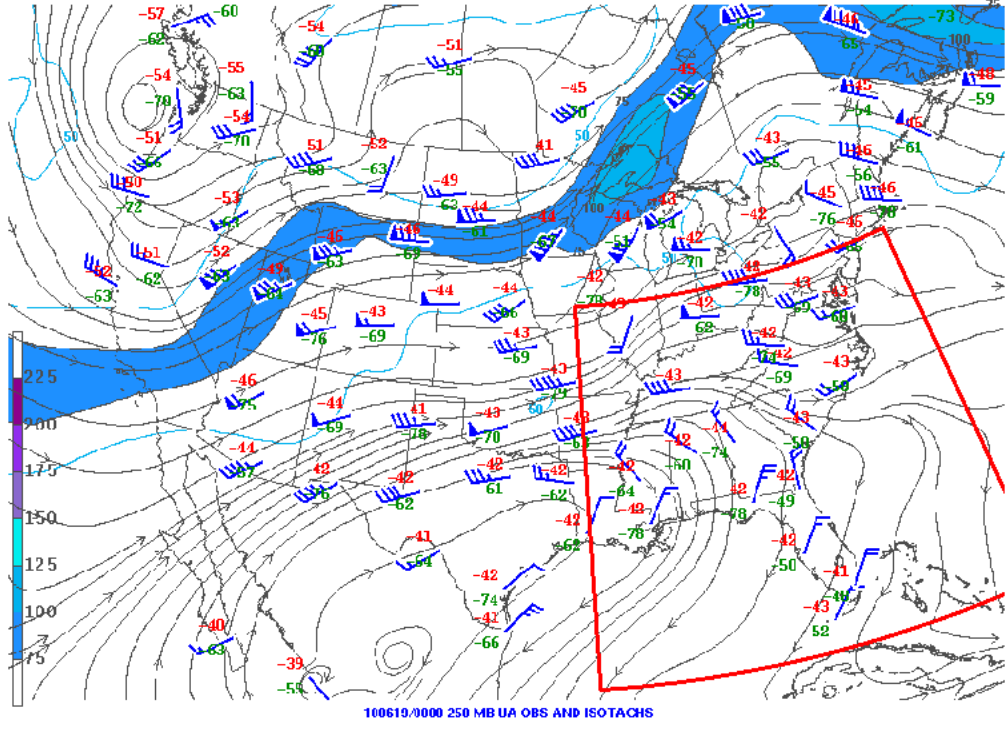
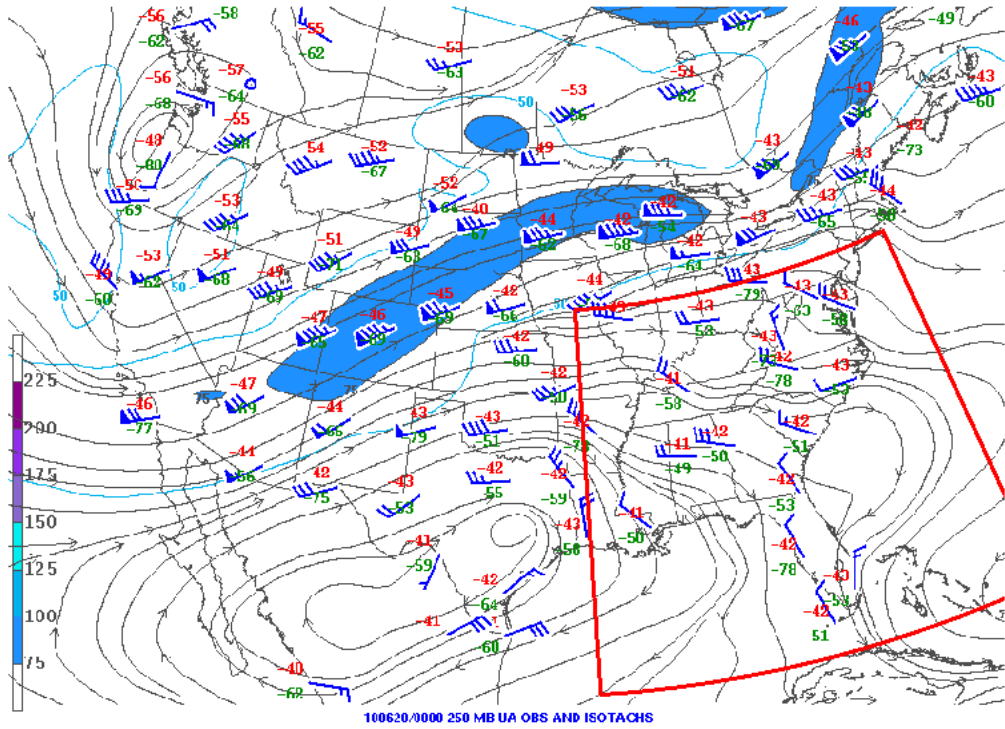


Figure 43 continued.

20 June 2010



21 June 2010

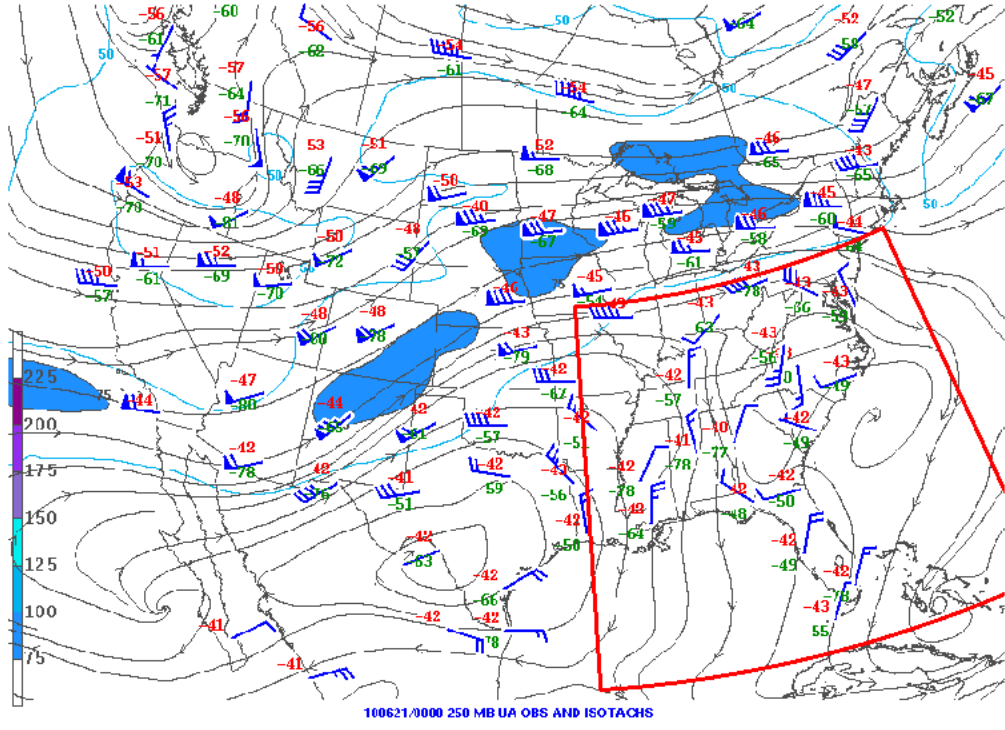
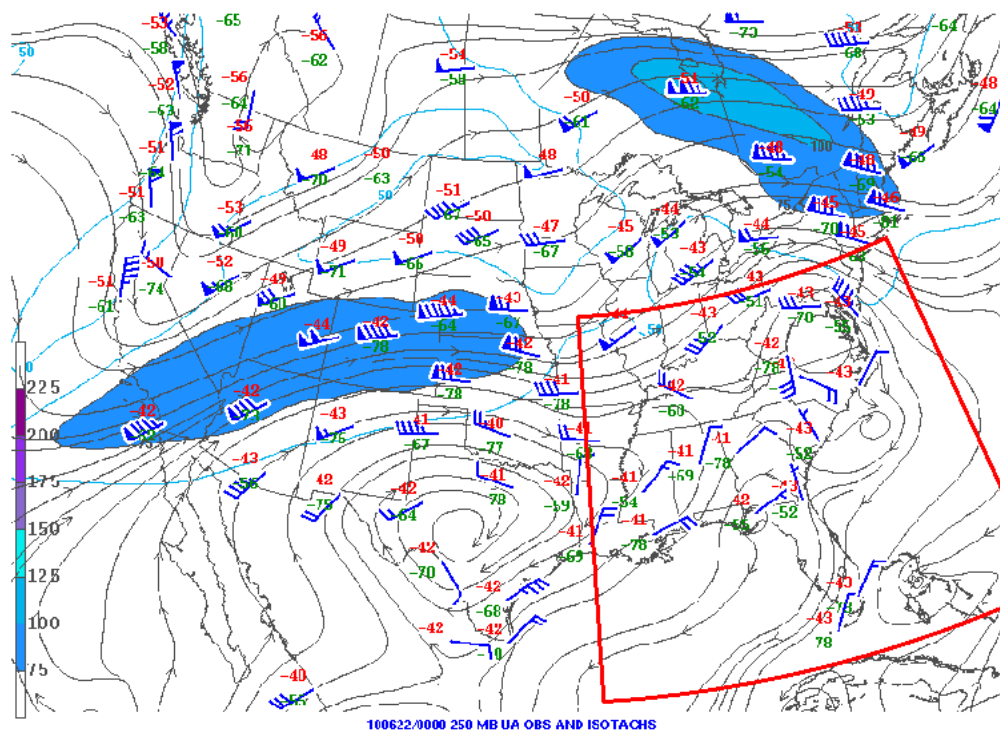


Figure 43 continued.

22 June 2010



23 June 2010

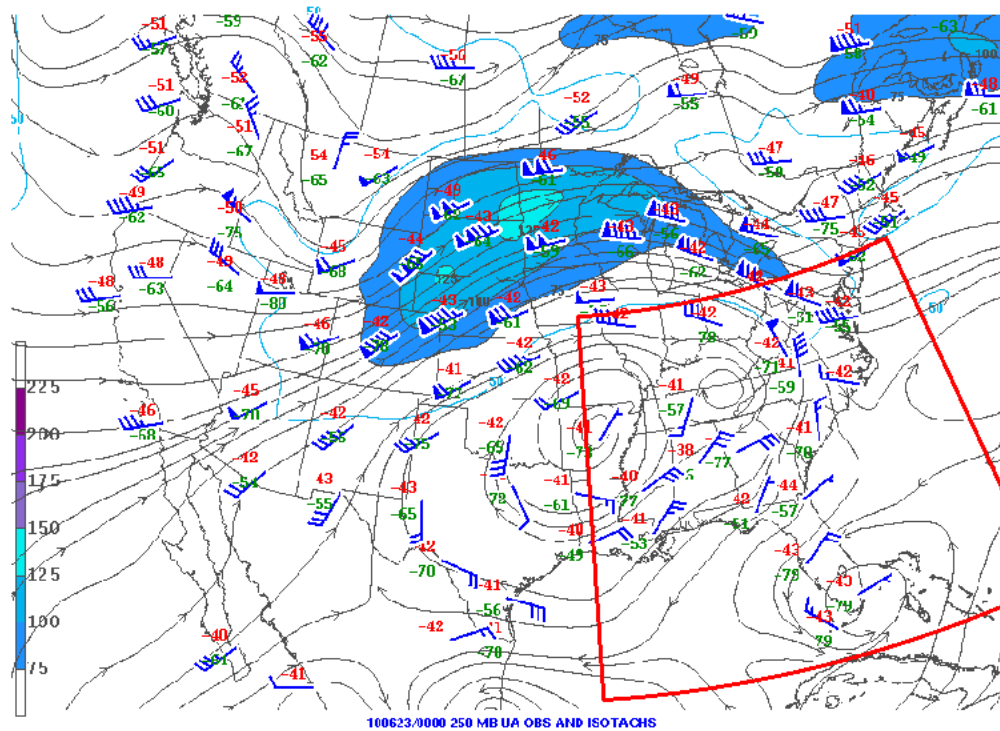


Figure 43 continued.